RANDOM PACKINGS VIA MECHANICAL CONTRACTION

ÁLVARO GONZÁLEZ GARCÍA

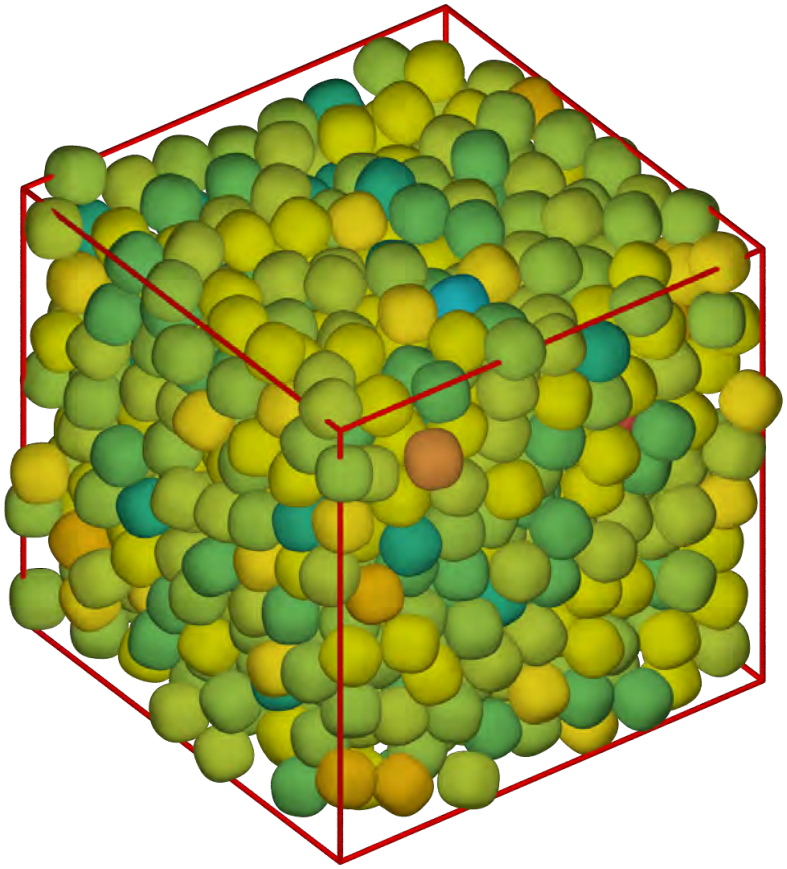

Revision and Expansion of the Mechanical Contraction Method

Van 't Hoff Laboratory for Physical and Colloid Chemistry

Universiteit Utrecht

SUPERVISORS:
Roel Baars
Albert Philipse

April 2015

Master thesis by Álvaro González García: *Random Packings via Mechanical Contraction,* Revision and Expansion of the Mechanical Contraction Method, © April 2015
SUPERVISORS:
Roel Baars
Albert Philipse

Who could ever calculate the path of a molecule?
How do we know that the creations of worlds
are not determined by falling grains of sand?

— Victor Hugo, *Les Miserables*

ABSTRACT

Random packings of particles are size independent, exhibiting the same features in the meso and in the nanoscale. These particle configurations are widely present in nature and technology, and their study constitutes an interesting and challenging topic.

One of the ways of inducing random configurations of granular matter is via computer simulations using a Mechanical Contraction Method (MCM), explained and analyzed in details in the present thesis. A more robust base has been provided to the method and its applicability has been extended to hard boundary conditions and superquadric shapes. The contact detection developed for superquadrics finds applicability beyond the results presented in this project.

An optimization of the set of parameters inherent to the MCM has been performed. For rods, a physical relation for the amount of overlap removed by means of translations or rotations has been developed. The outcome from the algorithm has been used to construct a glass-transition equation of state for rods of any aspect ratio. The influence of hard boundary conditions in random packings of rods has been connected with experimental results. Finally, random configurations of superballs have been generated and characterized.

The roots of the MCM has been revised. This has provided insight about its limitations and advantages.

CONTENTS

1 INTRODUCTION 1
- 1.1 Influence of Particle Shape 1
- 1.2 Random state of matter 3
- 1.3 Random Packings Study 6
  - 1.3.1 Theoretical studies 7
  - 1.3.2 Simulations 8
  - 1.3.3 Random Packings study via MCM 9
  - 1.3.4 Experiments 11
- 1.4 Random Packings in Nature and Technology 11
- 1.5 Aim and structure of this project 13

2 RANDOM PACKING OF RODS VIA MECHANICAL CONTRACTION 15
- 2.1 MCM: spheres 15
  - 2.1.1 Algorithm schema 15
  - 2.1.2 Parameter dependence of MCM 20
- 2.2 MCM for spherocylinders 23
  - 2.2.1 Algorithm modifications 24
  - 2.2.2 Parameter dependence for rods 29
- 2.3 MCM: Results for rods 29
  - 2.3.1 Pair distribution function reflects excluded volume effects 31
  - 2.3.2 ϵ interpretation 33
  - 2.3.3 Scan in Λ. Glass transition for rods 35
- 2.4 Conclusion and Outlook 42

3 RANDOM PACKINGS IN HARD BOUNDARY CONDITIONS VIA MECHANICAL CONTRACTION 47
- 3.1 Relevance of hard boundaries 47
- 3.2 Cylindrical Boundary Conditions 49
  - 3.2.1 Algorithm modifications 49
  - 3.2.2 Simulation results in a totally hard cylinder 53
  - 3.2.3 Simulation results in a z-periodic cylinder 54
- 3.3 Random packings confined in a wedge 57
  - 3.3.1 Algorithm modifications 58
  - 3.3.2 Simulation results. Scan in angle 61
- 3.4 Conclusion and outlook 64

4 RANDOM PACKING OF SUPERQUADRICS VIA MECHANICAL CONTRACTION 67

4.1 Introduction 67
4.1.1 Superquadrics, Superellipsoids and Superballs 68
4.1.2 Packings of Superballs 70
4.2 MCM for superquadrics 72
4.2.1 Energy constraint and overlap removal for general convex shape. 72
4.2.2 Contact Detection Algorithm between Superquadrics 74
4.3 Parameter dependence for Superballs 79
4.4 Results for Superballs 80
4.4.1 Pair distribution function reflects excluded volume effects. 81
4.4.2 Scan in deformation parameter γ 84
4.5 Conclusion and Outlook 88
A SHAPES, VOLUMES AND SURFACES 89
B OVERLAP REMOVAL DETAILS 93
B.1 General convex shape 93
B.2 Spheres 95
B.3 Spherocylinders 95
B.4 Expressions for the moment of inertia 97
B.4.1 Spherocylinders 97
B.4.2 Superquadrics 97
B.5 Important remark 98
C THE GLASS TRANSITION ASYMPTOTIC MATCHING 99
D VIRTUAL ROD IN A PLANE 103
E THE ENVELOPING SPHERE RADIUS FOR SUPERQUADRICS 107
E.1 General problem set up 107
E.2 Superballs 108
E.3 Supercuboids 108
E.4 Derivation in the general case 110
BIBLIOGRAPHY 111

1 INTRODUCTION

The current project deals with the theoretical and computational study of the random state of matter for different particle shapes and boundary conditions. The present chapter summarizes some of the ideas that are widely used later on: why particle shape and boundary conditions influence the physical behavior of a collection of bodies, what a random packing is and which method has been used for generating this random configurations. Finally, the objective and structure of this thesis are indicated.

1.1 INFLUENCE OF PARTICLE SHAPE

The hard sphere approximation constitutes the very first deviation from the ideal picture of a physical system: particles are not any longer points without volume, but their finite size plays a role. Such picture makes the explanation of phase transitions as deviations from the ideal gas equation possible [1, 2]. However, spheres are rotationally invariant, and thus the variety of phases is not as rich as the one provided by non-spherical shapes. Hard sphere models have been widely studied both theoretically and computationally [3–7]. This forms the reference system for comparing the features arising in non-spherical systems.

Upon increasing density, the most common phases expected are gas, liquid and crystal. The gas phase can be defined as the one in which particles are far enough for particle shape not playing a role. When nonsphericity has an effect, a complete zoo of phases shows up as density increases. The proper physical quantity for comparing different particle shapes is the *volume fraction*:

$$\phi = \frac{NV_p}{V} = \rho V_p \tag{1.1}$$

N is the number of particles considered, V_p is the volume of the particle, V is the volume of the system, and ρ is the number density. Notice that the number density by itself does not incorporate in any way the geometry of the particle, which effect is present via V_p. The volume fraction (also called *packing fraction*) is connected with the concept of porosity, which is defined simply as $(1 - \phi)$: whereas the volume fraction provides which percentage of the system is filled up by particles, the

porosity expresses the percentage of voids.

Particle shape affects the system in terms of *excluded volume*, which is the volume inaccessible to the particles in the system as a result of the presence of other particles. For instance, it was proved by Onsager [8] that the excluded volume for spherocylinders is given by:

$$V_{excl} = \frac{\pi}{2}L^2D + 2\pi LD^2 + \frac{4}{3}\pi D^3 \tag{1.2}$$

Excluded volume effects play a role in densities in which particles are close enough to feel each others' presence, and then its influence is higher the more elongate or prolate particles are (Equation 1.2). It may be noticed that sharpening the edges of particles is a kind of anisotropy, which is expressed in the higher excluded volume as particle asphericity increases [9–11].

Dealing with hard systems means that the potentials treated are step-like ones: what matters is only if particles are or are not in contact, and no attractive or repulsive forces are taken into account. Such kind of systems are denoted as (granular) *packings*, and only particle shape via excluded volume effects play a role in their final configuration. Depending on the theoretical framework considered, friction forces are or not taken into account in the study of this kind of systems.

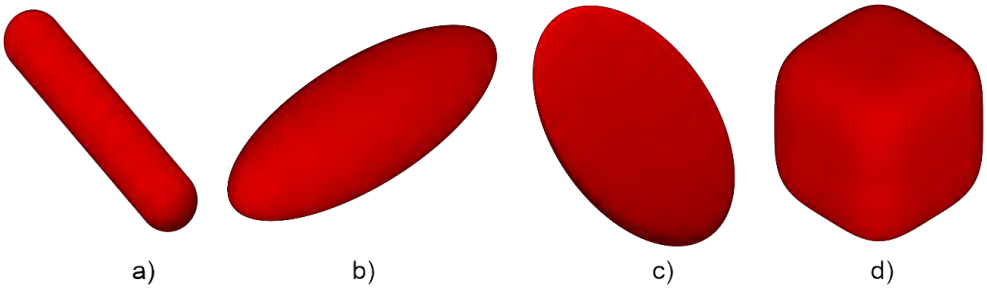

Figure 1.1: Graphical representation of several particle shapes. a) Sphereocylinder, b) Prolate ellipsoid, c) Oblate ellipsoid, and d) superball. Spherocylinders and ellipsoids exhibit nematic and smectic phases, among others. Both elongate and prolate ellipsoids show also more exotic phases such as crystal sm2 and stretched-fcc. [12–17] Very oblate ellipsoids (disk-like) also exhibit a columnar arrangement under certain situations [18]. Superballs (d) have been proved to present a plastic fcc crystal phase, as well as two possible columnar stackings.[10, 11, 19]

It is known that elongated particles exhibit nematic and smectic liquid crystal phases, whereas oblate particles also exhibit a columnar phase at high densities (Figure 1.1). The stable phase for a given set of parameters (temperature, pressure, density) is provided in terms of energy and entropy favorable conditions: any stable phase will imply a proper balance of minimum energy and maximum entropy. Systems constituted by spherocylinders and spheroids have been studied, and thus phase transitions can be predicted.[12–17]

Another example of the shape dependence behavior is shown in the superquadric or superellipsoid shapes. When dealing with closed volumes, and assuming that the three axis of the particles are equivalent, a superquadric must be regarded as a shape in between a cube and a sphere (a cube with round edges), and is commonly known as superball. The phase diagram for superballs have been also studied, and even more different phases are then revealed, such as a fcc plastic phase. [10, 11, 19]

Beyond these relatively easy mathematically definable shapes, systems made out of very strangely shaped particles have been studied. Of course the more complex the shape, the more difficult its study. Examples of hard particles already studied are platonic solids, dumbbells, octopods and bent spherocylinders. Almost any kind of particle can be modeled as a division of the surface in smaller subsurfaces, using procedures as the Voronoi tessellation. [20]

1.2 RANDOM STATE OF MATTER

A fact not contradicted by experience is that the highest packing fraction is achieved by ordering the particles that constitute a system, reaching crystalline or/and liquid crystal structures depending on particle shape [21]. However, another possible state for a dense system is characterized by the absence of order while still constituting a mechanically stable situation: particles cannot move any longer due to the fact that their degrees of freedom have been blocked by the surrounding particles. This is not necessarily a thermodynamically stable situation, but particles are in contact in a mechanically stable situation. These configurations are called *random packings*, and their importance is visible in their abundance in nature and technology [18, 22, 23].

Describing random states of matter is not a trivial subject. However, some characteristics can be quantified. The *mean contact number* ($\langle C \rangle$) defines the average number of contacting particles with a considered central one in a random packing.

This magnitude together with the volume fraction constitute the main physical observables for this state of matter. Thus, a question that arises is which is the minimum average number of particles randomly placed that blocks all movement of a considered central particle. This number is known as the *caging number*. With the purpose of describing the state of the system and how it is affected by particle shape, other contact numbers are defined. The *kissing number* is the maximum number of particles that can touch a particle, and the *parking number* is the average maximum number of particles that can be placed randomly on a central particle without interpenetration. It is expected that the mean contact number in a random configuration will lie in between the caging number and the kissing number, and above the parking number particles must rearrange, exhibiting thus some sort of local order. It should be highlighted, as an example of the complexity of random packings, that not even for spheres there exists an analytical solution for some of the variables here defined. Notice as well that the *coordination number* is a more general concept than the contact number, as far as the former defines a cut-off distance to define the nearest neighbours whereas in the latter the cut-off is defined by the particle's dimensions.

As an illustrative example, for spheres the caging number is $\langle \gamma \rangle = 4.71$ and the parking number is $\langle z \rangle = 8.7$ [18]. For a random packing of spheres, caging effects prevent the contact number to rise much above 5 without inducing local order in the system [24], finding normally a final coordination number around 6.

Although random packings have been widely studied, due to their nature there is not a clear definition or even a total agreement in literature of what a random state is. For instance, the usual definition of *Random Close Packing* (RCP) is the maximum density that a large, random collection of particles can attain. However, the concept of RCP was shown [25] to be mathematically ill-defined, and it turns out that it is better to use the notion of a *Maximally Random Jammed* (MRJ) state. On the other hand, the loosest possible random packing that is mechanically stable is denoted as *Random Loose Packing* (RLP).

For spheres, the MRJ state provides $\phi \approx 0.64$ [26, 27], and the RLP is reached for $\phi \approx 0.55$ [28]. Independently of the means by which it is generated, a random configuration of spheres will have a final volume fraction lying between this two values. It is remarkable that the values achieved experimentally [29] for random packings are closer to the RLP limit, whereas in many computer simulated results the goal is to get very close to the MRJ limit.

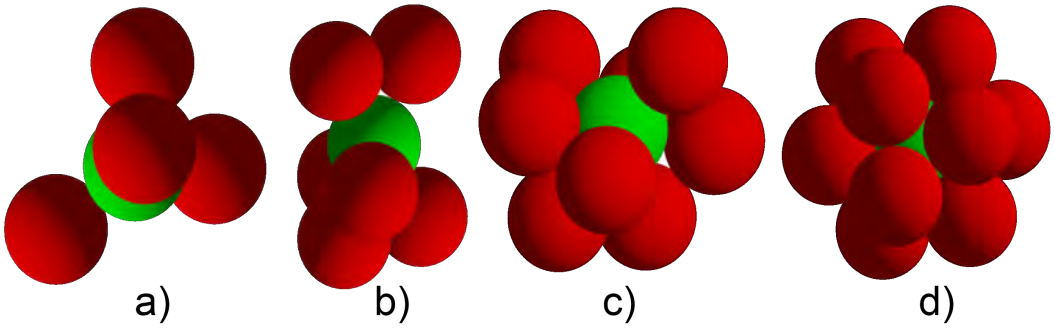

Figure 1.2: a) Sphere caged by four particles. Due to the fact that the caging number is $\langle \gamma \rangle = 4.71$, we can find some spheres in a final random packing configuration with few contacts. The minimum number of spheres to block a central one is 3.
b) A sphere being blocked by 6 bodies; the actual coordination number $\langle C \rangle$ in a random packing configuration is 6, thus this neighbour distribution is more than expected.
c) A sphere in contact with 8 other non overlapping particles; again if the mean value is 6 it is not surprising to find spheres in contact with this high number of spheres. This value is close to the parking number $\langle z \rangle$.
d) The maximum number of contacts for a sphere is 12, and it is achieved by aligning the centers of outer spheres with the vertices of an icosahedron with the length of the diameter of the central sphere.

The above statement is connected with one of the most exciting properties of random packings: they are, theoretically, size independent. Therefore the treatment of random packings is within the framework of the *granular matter* (regarding granular matter as conglomerations of discrete macroscopic particles). Despite the apparent simplicity of granular matter, granular materials behave differently from the other familiar forms of matter, which makes the problem of the random packing study a challenging and interesting subject. One example of this interesting behavior is the flow of sand grains: it is a solid system that somehow moves like a fluid [30]. Figure 1.3 constitutes an illustration of the independence of the random states with the scale.

Due to the difficulties in defining a random state, it is normal to measure the degree of order in the system, and check that its value is lower than those of the more ordered phases. This usually is done by means of structure order parameters and radial distribution function.

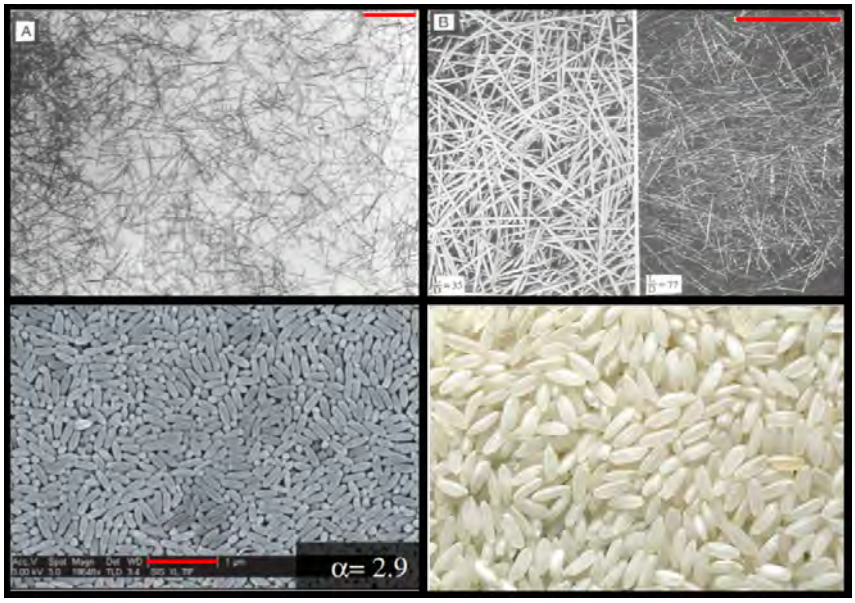

Figure 1.3: Top line: (A) Impression of a two-dimensional random distribution of silica rods on an electron microscope grid. The bar is 200 nm. (B) "Simulation" of a three-dimensional sediment of random rods with a random packing of wooden rods (left) and copper wire (right). The bars represent 2 cm. Image taken from [31]
Bottom line. Right: A Scanning Electron Microscopy image of colloidal rods (aspect ratio $\Lambda = 1.4$) with scale bar 1μm, taken from [32]. Left: common rice ($5.2 - 7$ mm each grain), with an aspect ratio of $\Lambda \approx 2.7$ [33].
These pictures illustrate the analogy between the colloidal and macroscopic random packings.

1.3 RANDOM PACKINGS STUDY

The complexity arising from the definition of the random state makes them an interesting and current object of study. Normally, the random packing of anisotropic particles is typically investigated case by case for each shape using either computer simulations or experiments, but theoretical models have been also proposed. Table 1.1 shows a comparison of the values from theory, experiments and simulations.

The final packing fraction that particles with a given geometry exhibit depends on the method used for achieving the considered random packing configuration (see Table 1.1). This happens already for spheres. Possible sources of discrepancies are the particular experimental set-up used, the algorithm defined for the simulations or the theoretical assumptions done. Even more, when computer-based

shape	ϕ_{max}^{rand} simulation	ϕ_{max}^{rand} experiment	ϕ_{max}^{rand} theory
Sphere	0.645	0.64	0.634
M&M candy		0.665	
Dimer	0.703		0.707
Oblate ellipsoid	0.707		
Prolate ellipsoid	0.716		
Spherocylinder	0.722		0.731
Lens-shaped particle			0.736
Tetrahedron	0.7858	0.76	
Octahedron	0.697	0.64	0.95
Dodecahedron	0.716	0.65	0.91
Icosahedron	0.707	0.61	0.82

Table 1.1: A comparison between the different values for random packings obtained by computer simulations, experiments and theoretical models. All data are taken from [34], except the data for the experimental and theoretical values for the platonic solids (tetrahedron, octahedron, dodecahedron and icosahedron) which have been taken from [35].

algorithms are used, the friction between particles might or might not been taken into account, which will result in different final packing fraction.

1.3.1 *Theoretical studies*

General random packing configurations of anisotropic particles have been studied using a mean-field theory that may be able to predict the optimal random configuration for any particle shape by decomposing it in spheres and calculating their effective Voronoi interactions [36, 37]. Also some articles can be found in the search of analytical solutions for random packings of bimodal and polydisperse spheres [38–40]. Due to their granular nature, regular physical concepts are also defined differently for random packings. The lack of well-defined conservation laws, on which a statistical description of the system could be based, produces the arise of concepts such as 'granular entropy', whose definition implies the computation of the number of ways in which N particles can pack into a given volume V [41]. The particularity of the random state of matter is also shown in the attempts of

constructing the phase diagrams of only the jammed state, from the random loose pack to the maximally random jammed state. [28, 42].

Random packings of particles show reproducibility: being not atomistic either in equilibrium they keep the principle of statistical mechanics that systems can be completely defined by a small number of parameters and can be constructed in a reproducible way. Although details of local structure are needed for a complete theory, there are large scale behaviors which fit into the structure of statistical mechanics. With these considerations, an ensemble can be defined for random packings: the *Edwards ensemble* [43]. This is a statistical ensemble of volume and stress fluctuations through the thermodynamic notion of entropy, compactivity (X), and angoricity (A), which are two temperature-like variables [44].

Since these systems are apparently difficult to study, it is not surprising to see a trend in theoretical studies for obtaining the best characterization of a random system, introducing, for example, appropriate order parameters [10, 45] and structural analysis [46, 47].

1.3.2 *Simulations*

The most extended way of generating random packings is using computer simulations, where a variety of algorithms exists to generate the final dense random configuration. The final main observables of the system (ϕ and $\langle C \rangle$) will depend on the algorithm employed. Without going into details, the main ideas of some of the procedures are summarized.

Random sequential addition (RSA): As its name denotes, the system starts with a configuration of particles in fixed positions, and then in a number of steps particles are randomly added without producing overlaps. This algorithm has already been used for some time [48], and its applicability has been checked for non-spherical particles [49], and even for hard hyperspheres[50, 51]. The final packing fraction obtained via RSA is always far below the RCP limit, as far as the condition that particles are in contact is not imposed [49].

Molecular Dynamics (MD): Classical MD methods determine the trajectories of the bodies by numerically solving Newton's equations of motion. For achieving random packings, they can be performed both for hard or soft particles by either increasing the density or by using dissipative dynamics in a gravitational field. One way to increase the density is by particle growth until a certain critical condi-

tion is reached. [52]

Lubachevsky-Stillinger Algorithm(LSA): The LSA consists in simulating the scenario of compressing a set of particles by contracting the system boundaries. The state of particle jamming is achieved via simulating a granular flow, which is rendered as a discrete event simulation, being the events particle-particle or particle-boundary collisions (if hard boundaries are present). [53]

Collision-Driven Molecular Dynamics (CDMD): At this point it is worth mentioning an algorithm that takes ideas from LSA and MD, and whose efficiency has been widely probed. It is the collision-driven MD algorithm for hard-particle systems developed by Donev et al[54, 55]. So far this algorithm is used to get a MRJ not only for spheres and ellipsoids [56], but also for superballs[57].

Mechanical Contraction Method (MCM): This method was developed by Williams and Philipse [58] and its main characteristic is that it is based on geometric arguments. Starting from a random distribution of particles, the system is quenched, and when particles overlap the penetrations are removed according to certain physical constraint. This is the method studied in the present project, and it is explained in details in Chapter 2 and further modifications are given in the corresponding consecutive chapters. Independently of the current project it has also been studied elsewhere recently[59].

Results of simulations performed using MCM are indeed a minor percentage of the total number of articles found concerning random packing of particles. It is here out of place to present a list of all the literature available concerning the subject, yet the big amount of information found reflects the importance of the topic. This research is mainly based on the original paper by Williams [58] and on Alan Wouterse's PhD thesis [18]. An accurate and extensive description of the MDMC method is found in Alexandar Donev's PhD thesis [56], where plenty of results and discussion concerning the random state of matter can be found. Finally, Joost de Graaf's PhD thesis provides very good ideas about how particles of any imaginable shape can be simulated (yet it does not concern about the random state of matter)[20].

1.3.3 *Random Packings study via MCM*

The top line of Figure 1.4 represents the final configuration of a MCM simulation for spheres and its contact number distribution. The color code will be kept during the whole project: the closer the particles are to red, the fewer contacts they have,

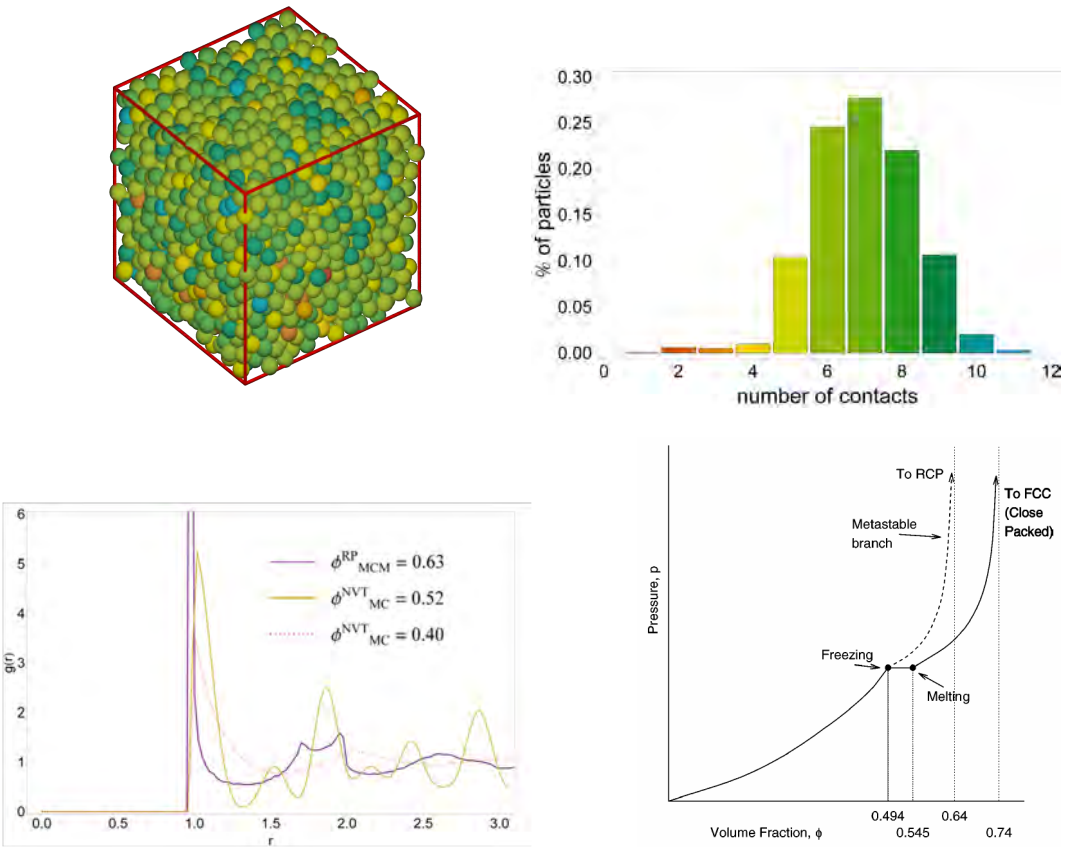

Figure 1.4: Top, left: final configuration for a collection of 1500 hard spheres using the Mechanical Contraction Method. Top, right: contact number distribution for the configuration on left. The colors of the spheres in the left have the contact number of the corresponding color bar in the right.
Bottom, left: final distribution function averaged over 20 different starting configurations using the MCM (ϕ_{MCM}) reaching a volume fraction of 0.63 compared with Monte Carlo NVT simulations at $\phi = 0.52$ and $\phi = 0.4$. Bottom, right: phase diagram for sphere, from [60].

and the reverse applies for purple. As can be seen, the mean contact number is close to 6, as expected for a random packing of frictionless spheres [18, 58]. Notice how in the final random state some particles have no contacts: they are able to move within cages formed by their immobile, jammed neighbors, and thus receive the name of *rattles*.

In the bottom line of Figure 1.4, the radial distribution function probes that, even Monte Carlo simulation being performed for hard spheres, the final configu-

ration at a lower packing fraction is more ordered that the final state of a system undergoing a Mechanical Contraction Method. This is shown in the more ordered peaks for the MC radial distribution function with respect to the one of the MCM. The phase diagram presents a distinction of the state achieved by MCM and MC simulations. Despite the fact that MC simulations in the NPT ensemble also deal with hard spheres, they take an objective pressure into account, and thus particles re-arrange upon a certain critical volume fraction, producing the liquid-crystal transition. The MCM is an athermal method, and the final configuration is a random distribution. This is reflected in the periodicity of the peaks of the $g(r)$: MC simulations at $\phi = 0.52$ show more ordered peaks at a lower volume fraction than the final configuration achieved via MCM. This agrees with the idea that the random metastable branch is achieved when the system is compressed very quickly, so that no thermal reorganization takes place.

Despite the fact that the present project only presents results for system with all particles equal, the MCM has also been applied to binary systems, providing results that are in agreement with the theoretical expected values. Moreover, also rod-sphere mixtures have been studied [61, 62], as well as systems constituted by hard ellipsoids and cut-spheres [18, 63].

1.3.4 *Experiments*

The interest in the random packing of particles and its theoretical size-independent configuration has generated very nice studies. For instance, we find rigorous studies of collections of *M&Ms* [64] or dice [35]. Image 1.5 shows systems used to characterize random packings of spheres (candy balls) and very sharp superballs (dice). It may be taken into account that when particles are set in non-periodic boundary conditions, the hard walls will induce order in the systems [65, 66]. This is one of the reasons why values of experiments will never be the same as the ones predicted by theory or computer simulations (see table 1.1).

1.4 RANDOM PACKINGS IN NATURE AND TECHNOLOGY

Random packings are commonly shown in nature: examples at the macroscopic scale are packings of sand, rice or glass fibers, whereas at the mesoscale we can find cellulose fibers in paper and colloidal rods in amorphous sediments[31]. Moreover, random packings can be applied to explain certain cell movements[67], or

Figure 1.5: Typical configuration for performing experiments of random packing of particles. Left: a random packing of spheres (*suikergoed*). Center: a random packing of dice. Right: A random packing of metal (magnetizable) rods. All random packings are generated within cylindrical hard boundary condition. Notice how the packing of dice form some sort of bent columnar phases near the glass of the container due to hard boundary effects.

even the structure of the cell cytoskeleton [68].

Not only in nature, but also in technology random packings also find its applicability. When systems are quenched at a high rate, the degrees of freedom of the particles are blocked mechanically by the other ones before reaching a thermodynamically more favorable situation [66]. For instance, one of the ways for building colloidal crystals is inducing order by means of a wedge, forcing particles to order not only by means of attractive forces but also by the geometrical properties of the container and particles. [69]

Furthermore, one of the goals of the present thesis is providing the starting configuration for a magnetic separation set-up [70]. Magnetic separation consists in extracting a magnetically susceptible material from a mixture using a magnetic force, and it finds its applicability in a wide range of fields (biological cell-selective separation, removal of heavy metals, purification, ...). A collection of randomly

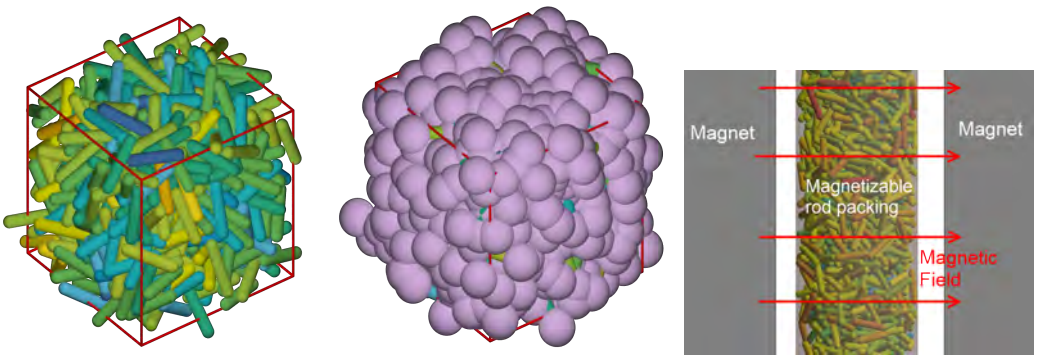

Figure 1.6: Graphical representation of the magnetic separation chamber using magnetizable rods ($L/D = 4$). Left: a random packing of rods in periodic boundary conditions. Center: the same configuration indicating the zone in which the rods attract mostly other magnetic particles (purple spheres). Right: schema of the magnetic separation chamber as a random packing of magnetizable rods within a cylinder.

oriented magnetizable rods inside a cylinder could be used as a magnetic separation chamber (Figures 1.5, left and 1.6). The flow of magnetic particles towards this random matrix will provide a check of the possibility of decantation by applying a magnetic field. This collection of magnetizable rods will produce a high magnetic gradient that allows the capturing of magnetic particles by the rods.

1.5 AIM AND STRUCTURE OF THIS PROJECT

This thesis may be regarded as a review and expansion of the Mechanical Contraction Method, going into details (Chapter 2) and expanding it for hard boundary conditions (Chapter 3) and superquadric shapes (Chapter 4). The feasibility of the MCM is then checked, and exiting new possibilities for this computational method are presented. The last section of each chapter presents conclusions and outlook for the particular subject treated.

All programs have been built using C++ from the GNU compiler collection. Images have been generated using either *Wolfram Mathematica 10.0.1* [71] or *POVRay*. All data analysis presented has been done in *Mathematica* as well.

2 RANDOM PACKING OF RODS VIA MECHANICAL CONTRACTION

The method to induce random states of matter via computer simulations used in this project is here described. The algorithm, named Mechanical Contraction Method (MCM), was developed first at the Van't Hoff Laboratorium in 2003 [58]. The present chapter presents first the MCM for spheres and then for spherocylinders.

A detailed analysis of this algorithm has been conducted, achieving an optimized set of variables in which the method is dependent. The most efficient manner of removing overlap between rods is clearly set via the moment of inertia for rods. The trends obtained for volume fraction and final mean contact number versus aspect ratio using a more robust MCM are in concordance with previous results. The packing fraction-final contact number relation is finally used to derive a glass transition equation of state by asymptotic matching.

2.1 MCM: SPHERES

Spheres are rotationally invariant, and they constitute the reference system when analyzing the outcome of more complicate particle shapes. Thus, the most logical starting point when studying the MCM is the case of spheres.

2.1.1 *Algorithm schema*

In the MCM procedure, a random packing is formed by quenching the system at a rapid rate. No thermal fluctuations or energy considerations are taken into account, except for the way in which the overlap created between particles is removed. This is consistent with the idea that a random packing is formed under a situation in which particles are kinetically trapped before they get into a thermodynamically more favorable situation: in random packings pressure dominates over any thermal fluctuation. MCM deals with particles that are frictionless, meaning that there is not any kind of force between particles.

2.1.1.1 *Periodic boundary conditions and initial configuration*

As it is the simplest situation possible, first the random packings in periodic boundary conditions for spheres are explained in detail. The meaning of periodic boundary conditions is shown in Figure 2.1: particles do not touch any hard boundary, and when a part of the particle 'leaves' one side of the box, its corresponding volume 'enters' the simulation box from its opposite side. The box with the final configuration has to be regarded as infinitely repeated in space, with each box having the same particle distribution. To ensure a physical solution with periodic boundary conditions, good statistics of a single box is compulsory.

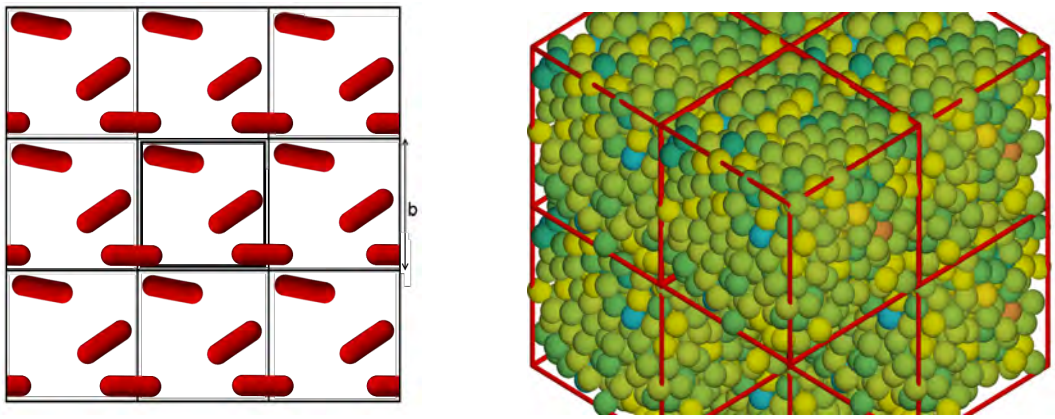

Figure 2.1: Left: Periodic Boundary Conditions schema, also known as Nearest Image Convention. Right: being the final state of a simulation for sphere of the box, the actual result implies this the box is infinitely repeated in space, with the same particle distribution.

The *initial condition* is a randomly distributed low-volume-fraction collection of non overlapping spheres in a periodic cubic cell. A pseudo-random number generator for particle positions and orientations was implemented as defined by Panneton et al [72], and the computer time at the moment that this number is generated is used as seed. Once a sphere i is placed, another randomly positioned sphere j will overlap if $|\boldsymbol{x}_{cm,i} - \boldsymbol{x}_{cm,j}| \leq |R_i - R_j|$, with $R_{i,j}$ the radius of the respective spheres and $\boldsymbol{x}_{cm,k}$ the center of masses of two considered spheres. Notice that this initial configuration constitutes by itself an Random Sequential Addition (RSA). Moreover, when the initial packing fraction is set to too high values, the maximum packing achievable by this method is the one of the RSA (for spheres, $\phi_{\text{RSA}}^{\max} \approx 0.38$ [49]).

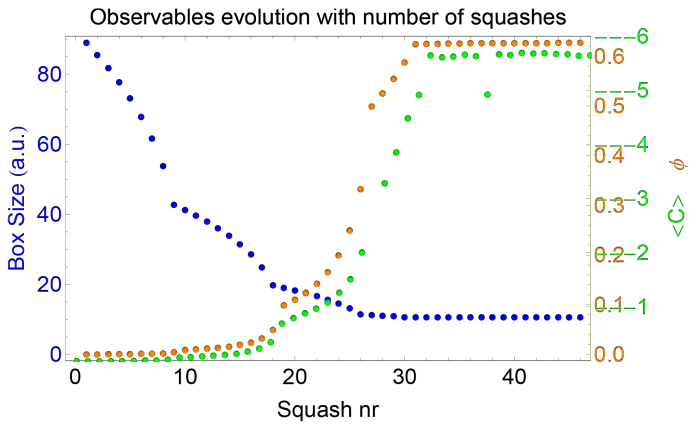

Figure 2.2: Evolution of observables during a MCM procedure of a system of $N = 1500$ spheres with $\beta = 0.2$. Meaning of β explained below in the text.

2.1.1.2 *Mechanical Contraction Method steps*

Once a non-overlapping configuration of randomly distributed spheres is generated, the subsequent algorithm steps are:

1. *Box scaling*: The volume of the cubic cell is reduced by a small amount ΔV and the particle positions are scaled by a factor s, such that a particle that was in the corner of the cell will remain in that corner of the scaled cubic cell. For non spherical particles, the orientation after the standard rescaling remains invariant. Being b the length of the cell, the length of the squashed box b' will be $b' = sb$ such that its volume will be $V' = V - \Delta V = (sb')^3$. The scaling factor, and thus the change in each particle center of mass, are given by:

$$s = \frac{b'}{b} = \frac{V'^{1/3}}{V^{1/3}} = \left(1 - \frac{\Delta V}{V}\right)^{1/3} \tag{2.1}$$

2. *Overlap removal*: The scaling of particle positions can produce particle overlaps. When an overlap is found, particles move such that overlap is removed in a certain maximum number of iterations defined by the user.

3. *Stopping criteria*: Once it is not possible to remove any overlap between particles after the number of tries specified, the last configuration in which no overlap between particles is present is taken as the final random packing.

Figure 2.2 shows some key characteristics of the MCM. As the simulation box shrinks, the volume fraction increases and so does the contact number following the same trend. The 'jumps' present are due to how the box is scaled: for a greater efficiency, the box scaling is bigger the lower the packing fraction is. The variation

in the main system observables shows a convergence before the stopping criteria is achieved. The time that the algorithm requires to perform a squash dramatically increases when the box is very small: the loop over the total number of tries to remove the overlap is only performed indeed when the simulation stops.

2.1.1.3 *Contact detection and overlap removal*

The direction in which the overlap is removed must be found in terms of the amount of overlap vector $\boldsymbol{\delta}_{ij}$ between particles i and j, defined as $\boldsymbol{\delta_{ij}} = \boldsymbol{k}_{ij} - \hat{\boldsymbol{k}}_{ij}(R_i + R_j)$ for two spheres. Here $\boldsymbol{k}_{ij}$ is the distance between the particle's center of mass, such that $\boldsymbol{k}_{ij} = \boldsymbol{x}_{cm,i} - \boldsymbol{x}_{cm,j}$ and $\hat{\boldsymbol{k}}_{ij}$ stands for its normalized vector. The contact detection for two spheres reads as $|\boldsymbol{\delta_{ij}}| \leq 0$ if no numerical relaxations are taken into account. The velocity at which a sphere i changes its overlap with another particle j is given by Equation 2.2. In the case of a mono modal system, the further simplification $D = R_i + R_j \forall (i,j)$ is straightforward.

$$\frac{\partial |\boldsymbol{\delta}_{ij}|}{\partial t} = \boldsymbol{a}_i \cdot \hat{n}_{C,ij} \qquad (2.2)$$

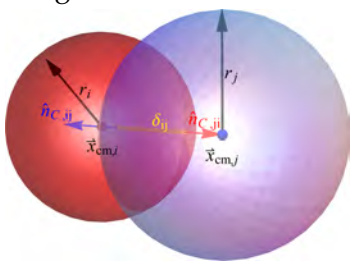

Figure 2.3: A view of two non equal overlapping spheres and the parameters involved in the contact detection and overlap removal.

As the radius of the spheres is constant, $\frac{\partial \delta_{ij}}{\partial t} = \frac{\partial k_{ij}}{\partial t}$. The change in overlap between particles i and j and thus the change in $|\boldsymbol{k}_{ij}|$ is maximum in the direction of $\boldsymbol{k}_{ij}$ (normal to the contact point in both surfaces, see Figure 2.3). As a particle i is surrounded by C particles in contact, the total change in overlap can then be expressed as a summation of all the considered velocities in order to remove the overlap. This summation over all overlapping particles represents a rate s_i at which the total overlap of particle i is changing.

The factor δ_i accounts for the largest overlap between particles, and is introduced to ensure that there is a preference to remove the larger overlaps over the smaller ones. The particle overlap is not moved all at once, since the overlap removal in the preferential direction may induce overlap with other particles: it is removed in several steps, provided that it is always removed in the direction of

most overlap. Figure 2.4 presents in light blue the amount of overlap for different spheres with a central one. This is accounted by the factor β. Despite the fact that originally ([18, 58]) the overlap removal was taken as half the value of the overlap amount ($\beta = 0.5$), there is no 'a priori' reason for this.

$$s_i = \sum_{j=1}^{C} \beta \delta_i \frac{\partial |\delta_{ij}|}{\partial t} \qquad (2.3)$$

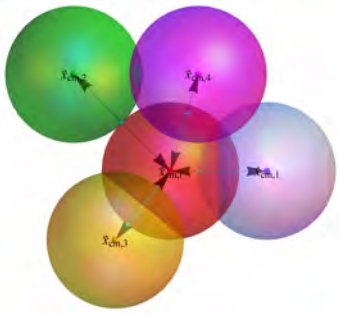

Figure 2.4: A view of a extreme case of many overlapping spheres (1,2,3,4) with a considered central one (i).

2.1.1.4 *Energy constraint*

What remains to know is what will be the actual direction of the velocity components for particle i, $\boldsymbol{a}_{i,k}$ with $k = x, y, z$. As expected from all previous discussion, the direction will be normal to the surface at the contact point. Assuming that contacts between particles behave as inelastic collisions, an energy constraint must be satisfied. Considering that the vector $\boldsymbol{a}_i$ was introduced as the overlap removal velocity, the kinetic energy at which particles remove overlap must be then conserved. The classical kinetic energy when only linear components of the speed play a role can be sorted such that the meaning of $\boldsymbol{a}_i$ is revealed:

$$\begin{aligned} E_{k,i} &= \tfrac{1}{2} m_i \boldsymbol{v}_i \cdot \boldsymbol{v}_i \\ 2E_{k,i} &= m_i (v_{i,x}^2 + v_{i,y}^2 + v_{i,z}^2) \end{aligned} \qquad (2.4)$$

This kinetic energy term comes from considering particle overlaps as collisions. From a computational point of view, any numerical value could be assigned to this magnitude. From Equation 2.4, a convenient choice can be made, such that $\boldsymbol{a}_i$ are the velocity components when the kinetic energy during overlap removal is numerically set to $2E_{k,i} = 1$.

$$\begin{aligned} &\text{if } 2E_{k,i} = 1 && \rightarrow v_{i,k} = a_{i,k} \\ &1 && = m_i (a_{i,x}^2 + a_{i,y}^2 + a_{i,z}^2) \end{aligned} \qquad (2.5)$$

This is the most general possible case, in which the mass of each particle must be taken into account. In a mono modal system, $m_i = m_j = m \forall (i,j)$, and it can be simply set that $2E_k = m$. Any other numerical choice is possible for the kinetic energy, but it would only enter as a constant factor in all derivations here presented.

Formally, the problem of how overlap is removed is reduced to minimize Equation 2.2 subject to Equation 2.5 for each contacting particle with the considered i. Once this is done, the final components of the speed are given as in Equation 2.6.

$$\boldsymbol{a}_i = \frac{1}{m_i} \sum_{j=1}^{C} \delta_{ij} \hat{n}_{C,ij} \tag{2.6}$$

Detailed step by step derivation of the Lagrange optimization problem can be found in Appendix B. As expected, the direction of the velocity components is actually the direction normal to the surface at the contact point. Notice that the dependence in particle's mass will only provide a constant factor that will be anyway taking into account by the overlap removal rate β: the actual direction does not change, but how much each sphere moves with respect to the others depends on their relative masses. This implies simply that a sphere will remove overlap faster the smaller its size with respect to the standard one. The standard particle diameter has been chosen to be $D = 1$.

Figure 2.5 presents a visualization of how a random packing of spheres is achieved via MCM with the considered overlap removal.

2.1.2 *Parameter dependence of MCM*

Although the algorithm is well-defined, some computational issues need to be taken into account when dealing with the MCM.

2.1.2.1 *Concerning contact detection*

How a contact is defined influences the final mean contact number $\langle C \rangle$ (also called coordination number). Concerning this, particles are allowed to have a very thin overlap before contact is actually detected, and the contact number is defined taking into account a thin shell surrounding the particles (see Figure 2.6). This provides a set of two variables in which the coordination number is involved. Given a particle with radius R_i, the values for the thin overlap and contact detection particle radius ($R_i \pm \delta R$) were optimized, getting values of $\delta R \in \{-10^{-7}, -10^{-10}\}$ for the inner sphere and $\delta R \in \{10^{-3}, 10^{-4}\}$ for the outer one.

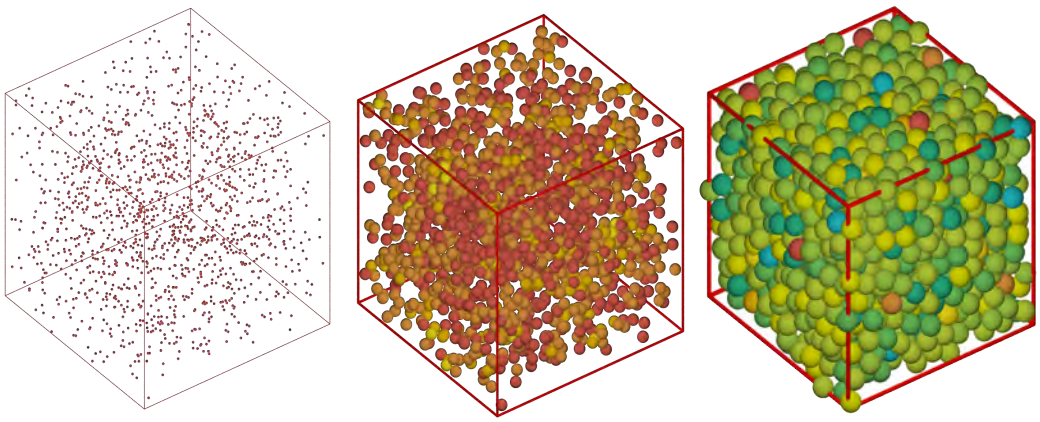

Figure 2.5: Graphical representation of several steps of a MCM process for spheres in a box with periodic boundary conditions. Left, initial configuration of randomly distributed and oriented particles. Center, an intermediate step in the MCM process. Right, final random packing of spheres with $\phi = 0.626$ and $\langle C \rangle = 5.82$.

2.1.2.2 *Concerning overlap removal*

Despite the fact that previous MCM calculations [18, 58] always used the value $\beta \approx 0.5$ for the overlap removal bias rate, this may not be the optimal one. Therefore, its influence in the particle's packing may be taken into account. Even more, there was also a parameter that created a small constant separation between particles, and it had the form of an additive factor in the summation in Equation 2.3. This last factor does not play a determinant role in all the simulations performed, and without a theoretical reason for incorporating it, it has always been set to zero. As shown in the radial distribution functions of Figure 2.6, the final particle distribution is not heavily affected by β: the final state is a random configuration, independently of the rate of overlap removal.

Whereas the particle distribution remains very similar, Figure 2.7 shows clearly how β affects the final packing fraction and mean contact number. The first one exhibits a slight increase of ϕ with β, and does not depend strongly in the small overlap allowed (and of course, either in the parameter used for outer contact detection shell). The final mean contact number shows an opposite behavior, and the effect of varying β is strongest when an outer shell radius is not taken into account.

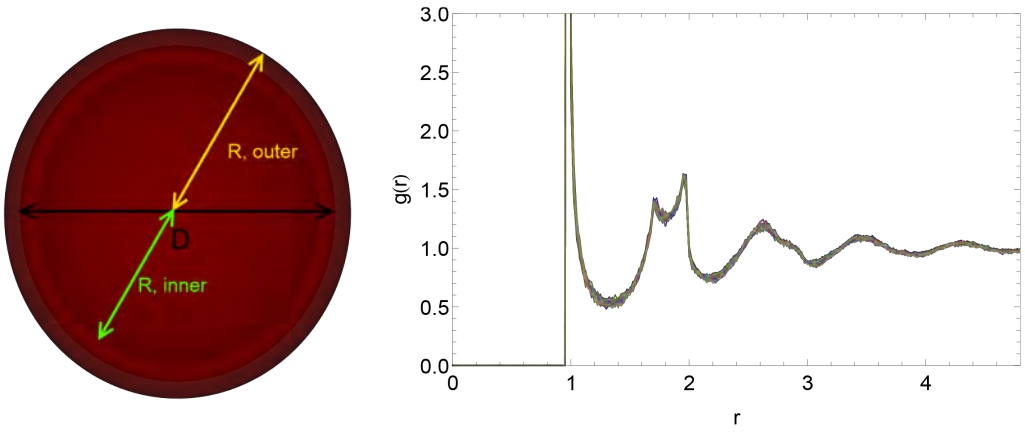

Figure 2.6: Left: A sphere and the considered inner and outer spheres for contact detection. The actual values chosen are too small to appreciate difference. The values for the overlap and contact detection are given as $R_{inner} = (R - \delta R)$ and $R_{outer} = (R + \delta R)$. Right: Collection of radial distribution functions for increasing β.

2.1.2.3 *Concerning neighboring particles*

Another set of two parameters are taken into account when performing MCM calculations. In this case, they are related with the building of the Verlet list. A Verlet list is a data structure to efficiently maintain a list of all particles within a given cut-off distance of each other, being the particles in this list the ones taken into account for the contact detection. By using this list, not all particle-particle distance are considered, but only the ones within the neighbour of each other, saving computational time. Thus, two parameters define the size of the neighborhood and how much a particle has moved with respect to its position before the Verlet list is rebuilt. An agreement of this two factors was found, such that the neighbour list was not rebuilt in excess and all particle-particle possible contacts were taken into account.

2.1.2.4 *Other considerations*

Apart from these parameters, the number of tries to remove the particle's overlap also influences the final packing configuration. A tendency of increasing final packing fraction with the number of overlap removal tries was found (not explicitly shown here). This is because the final configuration of the system will be given as the one of the squash for which overlap could be not removed any longer. Obviously, increasing the number of times the algorithm is called influences the

computational time of the simulation. A proper balance of accurate results-time is found for a number of tries of between $\{10^5, 5 \cdot 10^5\}$, whereas for 10^6 the time required for a single calculation to finish is too high. Of course, this time depends on the number of particles in the periodic box, the size of the neighbour list and the overlap removal rate. Regarding the number of particles, it should be high enough for a particle in the center of the box not feeling the influence of a particle in the side. This is required by the nearest image convention assumed.

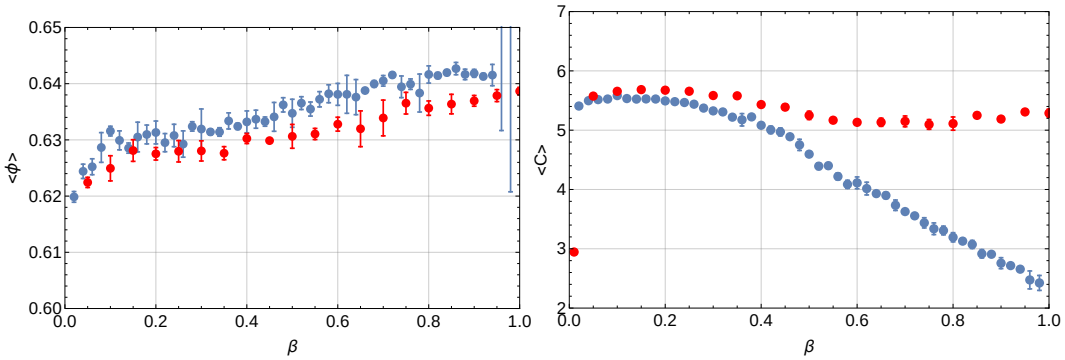

Figure 2.7: Final packing fraction and mean contact number as a function of β, averaged over three runs for a system of 1500 (blue) or 750 (red) spheres. The blue series have been performed with double number of tries for overlap removal than the ones for the red one, and without any outer shell consideration for contact detection.

The very big error bars for very high β in the blue series indicate the presence of order in the system (crystallization). In the bases of this plots, it may be notice that a lower overlap removal rate induces slightly lower possible local ordering in the system, reflected in a lower packing fraction. Regarding at Figure 2.7 it can be established that 750 spheres in a periodic box provides already good statistics for the MCM.

2.2 MCM FOR SPHEROCYLINDERS

The original paper by Williams and Philipse [58] concerned both spheres and spherocylinders. Yet the mathematical formalism for the overlap removal for spherocylinders is not general (see Chapter 4 for a description for any convex shape), here it is presented as in the original article. The spherocylindrical particle shape are of special interest as they are widely present in nature: from liquid crystal components (MMBA or 5CB) to rod like colloids (tobacco-mosaic virus, fd-virus, carbon

nanotubes, microtubuli, actin filaments ...) to amphiphilic molecules (soap, lipids, fat molecules, ...). Furthermore, membrane cells can be approximated as collections of self-assembly rods [73]. The study of the glass transition and the limit of thin rods are very interesting problems, for which the results provided by the MCM will provide some insight.

2.2.1 *Algorithm modifications*

Modifications on the algorithm for spheres are required due to the change on particle shape. Particularly, the contact detection and overlap removal for spherocylinders must account for higher rotational degrees of freedom that these particles have with respect to spheres.

2.2.1.1 *Spherocylinder: detailed description*

A spherocylinder, also called *capsule* or *rod*, is a cylinder (with length L) capped at its ends by hemi spheres with the same diameter (D) as the cylinder (Figure 2.8). A scalar magnitude to compare rods of different lengths is their aspect ratio Λ. Given a rod with centroid $\boldsymbol{x}_i$ and its orientation $\hat{r}_i$, the end points $\boldsymbol{p}_{+,i}$ and $\boldsymbol{p}_{-,i}$ of the cylinder can be obtained. Provided Λ_i, $\hat{r}_i$ and D_i, a rod is fully described.

$$\Lambda_i = \frac{L_i+D_i}{D_i} = 1+\frac{L_i}{D_i} \qquad \boldsymbol{p}_{\pm,i} = \boldsymbol{x}_i \pm \frac{1}{2}L_i\hat{r}_i \tag{2.7}$$

The normalized vector $\hat{r}_i$ gives the orientation of the rod towards its axis of symmetry: it is a vector that lays across the length of the rod (Figure 2.8). The rod length is chosen to be the z' local axes of the particle, and the other components of the rod local frame of reference are perpendicular to this one, and are constructed given $\hat{r}_i$ (see Appendix B).

2.2.1.2 *Rod-Rod contact detection*

Having an accurate rod description, a contact detection needs to be defined in order to get the overlap between particles. The contact detection used is the one defined by Vega and Lago [74], and the main ideas are here briefly summarized as a quick reference. The case of nearly-parallel rods required some special treatment by incorporating a small factor that allowed to identify whereas rods were or not actually parallel.

Let us consider the general case of two rods with lengths L_i and L_j and radius R_i and R_j. Let $\boldsymbol{k}_{ij}$ be a vector connecting two arbitrary points in the symmetry

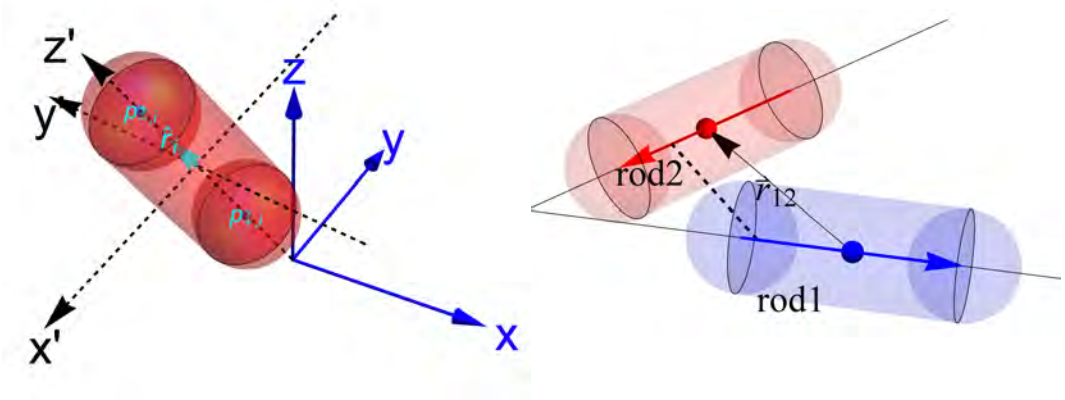

Figure 2.8: Right:The main parameters involved in the rod description, including global (blue arrows) and local (black dotted arrows) reference frames for a rod with $\Lambda = 3$. Left: Diagram for Vega and Lago contact detection algorithm between rods[74]. The dotted line indicates just the distance between two random points in the rod axes of symmetry ($\boldsymbol{r}$).

axes of the considered rods, $\boldsymbol{r}_{ij}$ the vector connecting the centroids and $\hat{r}_i$ and $\hat{r}_j$ the vectors defining each one of the rod orientations. The two points on the rod main axes will be given by a set of two scalars l_i and l_j times the corresponding unitary orientation vector.

$$\begin{aligned} \boldsymbol{k}_{ij} &= \boldsymbol{r}_{ij} - l_i\hat{r}_i + l_j\hat{r}_j, \text{with } l_m \leq \tfrac{1}{2}L_m,\ m = i,j \\ |\boldsymbol{k}_{ij}|^2 &= |\boldsymbol{r}_{ij}|^2 + (l_i)^2 + (l_j)^2 + 2l_i\boldsymbol{r}_{ij}\hat{r}_j - 2l_i\boldsymbol{r}_{ij}\hat{r}_i - 2l_il_j\hat{r}_i\hat{r}_j \end{aligned} \tag{2.8}$$

Let l_i^* and l_j^* be the values of l_k that minimize $|\boldsymbol{k}_{ij}|^2$:

$$\left.\frac{\partial|\boldsymbol{k}_{ij}|^2}{\partial l_i}\right|_{l_i^*} = 0 \ \wedge \ \left.\frac{\partial|\boldsymbol{k}_{ij}|^2}{\partial l_j}\right|_{l_j^*} = 0 \tag{2.9}$$

The obtained values l_i^* and l_j^* will provide the solution $\boldsymbol{k}_{ij}$ that provides the minimum rod-rod distance. Thus, the rod-rod contact condition will be defined in terms of the minimum distance between two points on the rod's main axis.

$$\boldsymbol{k}_{ij}^2 \leq (R_i + R_j + (\delta R_i + \delta R_j))^2 \tag{2.10}$$

, where the factor $(\delta R_i + \delta R_j)$ will play the same role as the inner/outer shell for spheres. Further details will be explained in the section concerning the parameter dependence for rods.

2.2.1.3 *Energy constraint and overlap removal*

The main features concerning the MCM for spherocylinders follow the ideas of the algorithm described for spheres. The starting configuration will be a collection of randomly positioned and oriented rods, and the standard particle scaling just moves the center of mass of the particle as it was done for spheres, whereas the particle orientation remains the same. Thus, the particle orientation will only change due to the overlap removal.

This change in the rod orientation will be given in terms of how big the overlap between them is. As it happened for spheres, the amount of overlap for rods will be given in terms of a vector $\boldsymbol{\delta}_{ij}$, such that the overlap between two particles can be expressed again as $\boldsymbol{\delta_{ij}} = \boldsymbol{k}_{ij} - \hat{\boldsymbol{k}}_{ij}(R_i + R_j)$. The relation $\frac{\partial \boldsymbol{\delta}_{ij}}{\partial t} = \frac{\partial \boldsymbol{k}_{ij}}{\partial t}$ still holds (as $\boldsymbol{\delta}_{ij}$ and $\boldsymbol{k}_{ij}$ are collinear), although $\boldsymbol{k}_{ij}$ does not have the same meaning as for spheres. The difference with to respect spheres is that now $\boldsymbol{k}_{ij}$ does not connect the particle's centers of mass themselves, but a linear translation of the center of the particle in its axis of symmetry. This main idea follows from the fact that rods can be regarded as sweep spheres, allowing for instance the use of their symmetry for a very fast contact detection algorithm. At this point, it is clear that $\boldsymbol{k}_{ij}$ is the solution of the contact detection algorithm defined in the previous section. The rod-rod contact detection is expressed as for spheres, $|\boldsymbol{\delta}_{ij}| \leq 0$ .Figure 2.9 should help to clarify the meaning of the overlapping vector for rods. Notice that yet $\boldsymbol{k}_{ij}$ and $\boldsymbol{\delta}_{ij}$ are collinear, they are in general not parallel to the vector connecting the center of masses of the rods.

For rods, overlap by means of rotational components can only be removed with rotations around the x' and y' axes (see Figure 2.8). Two extra velocity components a_4 and a_5 are introduced as the two possible rotations in the particle reference frame. Following rigid solid physics [75, 76], the particle rotation can be described in terms of rotations around the main particle axes, and within this frame of reference the matrix of inertia will be diagonal. For spherocylinders, the moments of inertia associated with rotations considered ($w_{x'}$,$w_{y'}$) that remove the overlap are equivalent (*parallel axis theorem*). The three components of the moment of inertia for rods are reduced to two, and are denoted by the scalar magnitude I in the local frame of reference (that is $I_{x'} = I_{y'}$ and $I_{z'}$). As rotations around the z' axis of the particle do not remove overlap, $I_{z'}$ can be set to zero in this particular problem

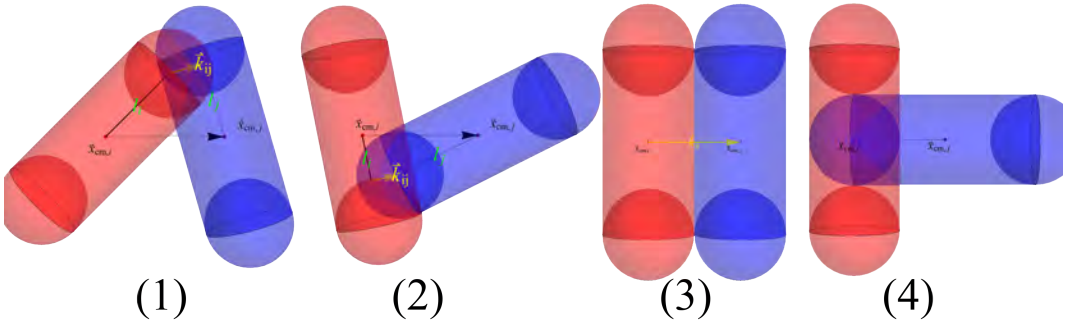

Figure 2.9: Several overlapping situations for a pair of rods. l_i and l_j, the position of the center of masses, and the vector connecting the center of masses of both rods are clearly indicated.

- (1) and (2) are two randomly oriented rods.
- (3) presents the situation of two totally aligned rods. Being $|\boldsymbol{k}_{ij}| = D$, they do not overlap.
- (4) presents the situation of two totally perpendicular rods. Being $|\boldsymbol{k}_{ij}| = 0$, they have an overlap distance $|\delta_{ij}| = D$.

(equivalently, it can be just assumed that $\omega_{z'} = 0$). This follows from the most general case, in which a $6D$ vector of scaled components of velocity is defined:

$$\begin{aligned} \boldsymbol{a}_i &= \left(\boldsymbol{a}_i^{\mathrm{L}}, \boldsymbol{a}_i^{\mathrm{R}}\right) = \left(a_i^{\mathrm{L}_x}, a_i^{\mathrm{L}_y}, a_i^{\mathrm{L}_z}, a_i^{\mathrm{R}_x}, a_i^{\mathrm{R}_y}, a_i^{\mathrm{R}_z}\right) \\ \boldsymbol{a}_i^{\mathrm{rod}} &= \left(\boldsymbol{a}_i^{\mathrm{L}}, \boldsymbol{a}_i^{\mathrm{R}}\right) = \left(a_i^{\mathrm{L}_x}, a_i^{\mathrm{L}_y}, a_i^{\mathrm{L}_z}, a_i^{\mathrm{R}_x}, a_i^{\mathrm{R}_y}, 0\right) \end{aligned} \tag{2.11}$$

R and L in Equation 2.11 stand for linear and rotational, respectively. These two extra components of the speed will of course play a role in the physical constraint, and also in the rate at which overlap is removed. The explanation that follows from here assumes a mono-modal system. The general case would only require a different arrangement of the term m_i, and can be found in Appendix B. Let's start considering the addition of the rotational term to the linear components of the kinetic energy.

$$\begin{aligned} E_{k,i} &= \tfrac{1}{2} m_i \boldsymbol{v}_i \cdot \boldsymbol{v}_i + \tfrac{1}{2} \boldsymbol{\omega}_i \boldsymbol{I}_c \boldsymbol{\omega}_i \\ \text{Assuming: } m_i &= m \forall i \quad \wedge I_{x'} = I_{y'} = I \wedge I_{z'} = 0 \wedge E_{k,i} = 1 \\ 1 &= m \boldsymbol{a}_i^{\mathrm{L}} \cdot \boldsymbol{a}_i^{\mathrm{L}} + I_i \left((a_i^{\mathrm{R}_x})^2 + (a_i^{\mathrm{R}_y})^2 \right) \end{aligned} \tag{2.12}$$

So far, we have only incorporated two extra velocity components under the numerical assumption that $2E_{k,i} = 1$, as it was done before for spheres. Now, we

consider that the density of all particles is also the same, and we set it to one. This derivation also implies a very strong fact to take into account in the dimensioning of the MCM: the density of each particle is set to 1, such that the units of mass and volume are equivalent.

$$\begin{aligned} \text{Assuming: } \rho &= 1 \quad \wedge m = V_p \\ 1 &= m\boldsymbol{a}_i^{\mathrm{L}} \cdot \boldsymbol{a}_i^{\mathrm{L}} + \tfrac{I}{V_p}\left((a_i^{\mathrm{R}_x})^2 + (a_i^{\mathrm{R}_y})^2\right) \\ 1 &= m\boldsymbol{a}_i^{\mathrm{L}} \cdot \boldsymbol{a}_i^{\mathrm{L}} + \varepsilon\left((a_i^{\mathrm{R}_x})^2 + (a_i^{\mathrm{R}_y})^2\right) \end{aligned} \tag{2.13}$$

Where $\varepsilon = \frac{I}{V_p}$ accounts for the removal of overlap by rotations. This exact definition could not be found in previous research concerning the MCM. As for rods the overlap removal by rotations is accounted by a scalar number, the effect of modifying ε in the algorithm was studied in details. Results are presented in a later section.

Considering the two possible rotations, a relatively simple overlap removal velocity between two rods can be defined: any rotation will be described as a combination of trajectories in two planes defined by x' and y' (instead of the most general case of a rotation described in three dimensions, see Appendix B). Let $\hat{u}_{x',i}$ and $\hat{u}_{y',i}$ be the unitary vectors defining the axes x' and y'. Introducing the projections of the vector defining the contact distance $\boldsymbol{k}_{ij}$ in the particle axes as $K_{ij,4} = \boldsymbol{k}_{ij} \cdot \hat{u}_{i,x'}$ and $K_{ij,5} = \boldsymbol{k}_{ij} \cdot \hat{u}_{i,y'}$, the total overlap removal rate can be defined for rods as:

$$\frac{\partial|\delta_{ij}|}{\partial t} = \boldsymbol{a}_i \cdot \hat{n}_{Cij} + l_{ij}K_{ij,x}a_i^{\mathrm{R}_x} + l_{ij}K_{ij,y}a_i^{\mathrm{R}_y} \tag{2.14}$$

Now that the energy constraint is properly defined, a constraint optimization needs to be done. In this case, the optimization consists on minimizing Equation 2.14 subject to Equation 2.13 for each particle in contact with the considered one (Equation 2.3). However, it turns up that the exact mathematical solution is quite heavy. Moreover, the effect of how much overlap is removed is at the end biased by the factor β, and the most overlapping particle parameter δ_j. Thus, an implementation of the exact solution in the code is not necessary, and it would only increase the time of that the simulation takes. The same happened when the term m_i was not taken into account for mono modal systems of spheres: it enters as a constant factor in the well defined overlap removal direction obtained via constraint optimization. Upon some considerations (see Appendix B), the simplified solution for all velocity components for rods (2.15) simply contains the linear components pre-

viously defined and incorporates the two rotational components by relating them with ϵ, l_{ij} and K_{ij}.

$$\begin{aligned} \boldsymbol{a}_i^{\mathrm{L}} &= \sum_{j=1}^{C} \delta_{ij} \hat{n}_{C,ij} \\ \boldsymbol{a}_i^{\mathrm{R}_x} &= \frac{1}{\epsilon} \sum_{j=1}^{C} \delta_{ij} l_{ij} K_{ij,x} \\ \boldsymbol{a}_i^{\mathrm{R}_y} &= \frac{1}{\epsilon} \sum_{j=1}^{C} \delta_{ij} l_{ij} K_{ij,y} \end{aligned} \tag{2.15}$$

2.2.2 *Parameter dependence for rods*

The present section will study the effect of the parameters within the MCM algorithm for rod like particles. The set of parameters present is just the same as in spheres. In Figure 2.10 it can be appreciated that the trend followed by the packing fraction with the overlap rate removing factor β is the same as the one observed for spheres. By performing linear regression for all particle aspect rations, the maximum increase in the packing fraction from the lowest to the highest β is 0.018 for $\Lambda = 10$. The same can be done for the mean contact number: it can be lowered by 0.58 with increasing β , in this case for $\Lambda = 3$. The nematic order parameter of the final configuration also constitutes a probe that the final state of the system is random, independently of the starting configuration (big error bars) or the biased rate of overlap removal (β) taken. The most appropriate choice for β regarding the dependencies of ϕ and $\langle C \rangle$ with this value is $\beta \in \{0.1, 0.3\}$. This ensures both a final random configuration and a smooth overlap removal between rods. However, this does not imply that higher values of β do not produce a final random configuration of rods.

The same considerations of inner and outer shell done for spheres concerning the contact detection is applied to rods. It may be noticed that the considered particle for contact only varies the rod diameter, not its length (Figure 2.11). This makes sense in the basis that a contact is detected taking into account the cylinder radius. Yet, the influence of this contact detection is not really big at all, and for the values taken for the simulations performed it never even arises to the 0.5% volume difference. Due to the D dependence of the contact particle shape, the contact detection is not really modified with increasing particle aspect ratio.

2.3 MCM: RESULTS FOR RODS

As expected, the main steps of the MCM are just the same for rods as for spheres. Algorithm modifications concern contact detection and overlap removal, but the

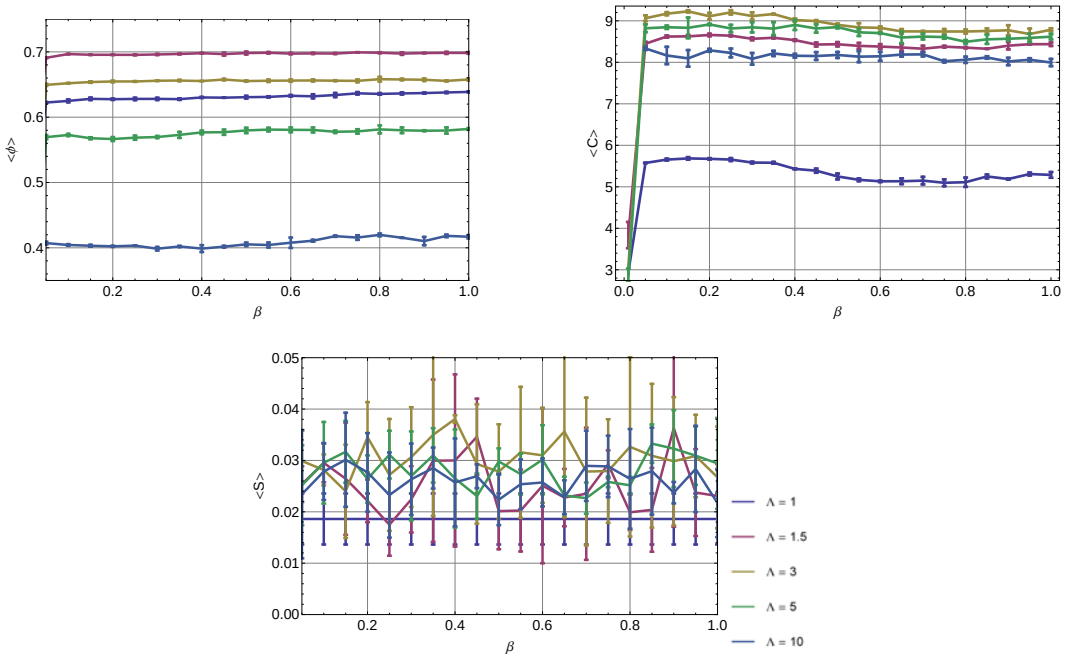

Figure 2.10: Top, left: final volume fraction as a function of β for three different initial configurations of systems of 1500 particles with different particle aspect ratios. Top right and bottom left, the same for the mean contact number and the final nematic order parameter.

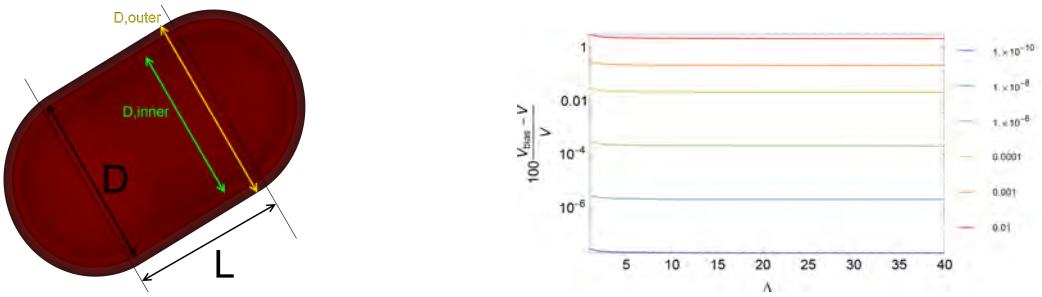

Figure 2.11: Left: Spherocylinder with $\Lambda = 1.5$ and the corresponding inner and outer shell for contact detection within the MCM (compare with Figure 2.6). Right: plot in logarithm scale of the relative difference in volume for the considered contact particle and the simulated particle, expressed in percentage. The legend shows the value of the variation in the diameter with respect to the considered particle ($\delta D = 2\delta R$): $D_{contact} = D + \delta D$.

overall picture just remains the same. This is clearly shown in Figure 2.12.

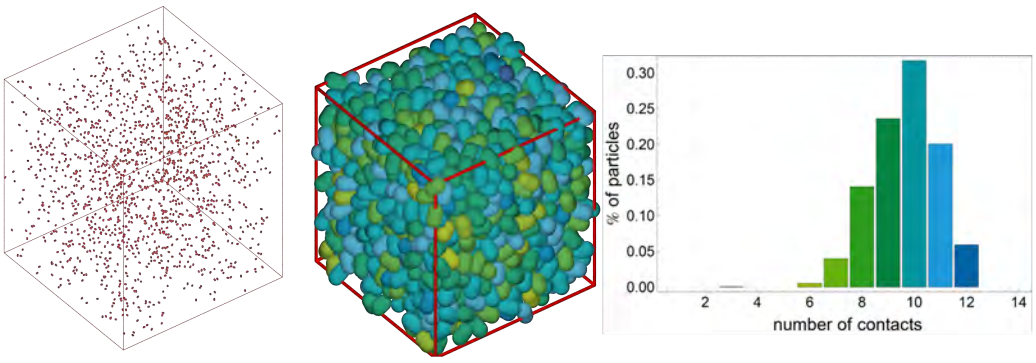

Figure 2.12: Initial (left) and final (center) configuration within a MCM simulation for a system of 1500 rods (spherocylinders) with $\Lambda = 1.5$. Right: contact number distribution for the final configuration (compare with Figure 1.4)

However, the outcome from simulations of rods will provide insight about the effect of particle's anisotropy in the final random packing configuration. Figure 2.13 presents a visualization of final configurations of random packings of rods as varying aspect ratio.

2.3.1 *Pair distribution function reflects excluded volume effects*

The excluded volume effect will increase as particle aspect ratio increases, due to the increase in anisotropy of the particle (Equation 1.2). Information about excluded volume is found in the *radial distribution function* ($g(r)$), which may be regarded as a measure of the probability of finding a particle at a distance of r away from a given reference particle, relative to that for an ideal gas. In very diluted (ideal gas like) systems, and in the limit $r \to \infty$ it always tends to one: particles that are far from each other are uncorrelated, and particle shape does not affect this state of matter.

This is shown, for instance, in Figure 2.14. For spheres, the radial distribution function shows an heterogeneous peak distribution, in contrast with the one obtained as a hard sphere system crystallizes (comparative made in Figure 1.4). The first peak is always present in the smallest particle dimension: it implies that no particle overlaps are present in the final configuration of the system. In this case, as the particle diameter is one, a peak will be always found at this value of r. For spheres, consecutive peaks will be present close to multiples of its diameter, and

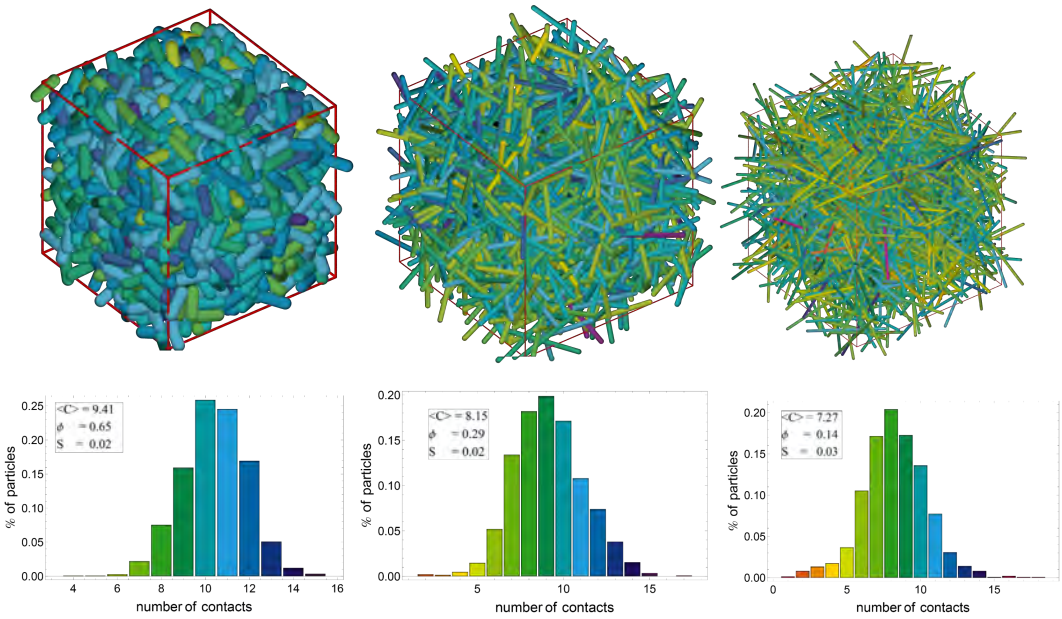

Figure 2.13: From left to right: final random packing configuration (top) and contact number distribution (bottom) of 1500 particles for rods with particle aspect ratio of 3 (short rods),15 (close to long rod limit) and 30 (long rods). The meaning of what short or long rods are is discussed later in this chapter (2.3.3.1).

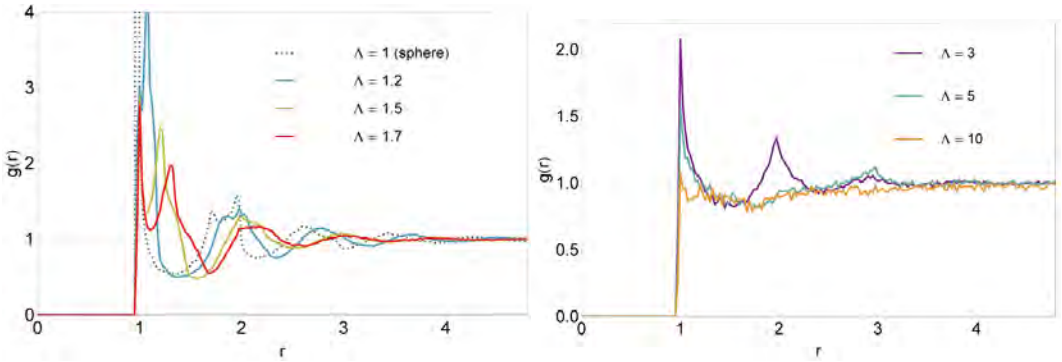

Figure 2.14: Radial distribution functions for different aspect ratios averaged over 20 runs for different particle aspect ratios.

more displaced to the left the further the particles are.

Due to the increasing particle anisotropy, as Λ increases the height of the first peak decreases. Whereas for spheres the neighboring particle distances are re-

stricted to values close to multiples of its diameter, for rods excluded volume effects induce peaks at distances in between the diameter and the length of the particle. This is clearly shown in the split of the first peak for small Λ: for low particle aspect ratios it is very likely to find another particle at a distance close to its length as well as at its diameter. This is also reflected in the fact that the height of the two peaks is almost the same. This increase in the particles relative positioning can also be connected with the higher packing density for rods that are mainly small deviations from the sphere shape (Figures 2.10 and 2.18).

This increasing of the packing fraction with particle aspect ratio reaches a maximum, and then the final packing fraction is lower than the one for spheres. For $\Lambda = 3$ a secondary peak is clearly shown at $r = 2D$, which is the particle's length and corresponds to a distance between the center of masses of two perpendicularly oriented rods (see Figure 2.15).

For higher Λ the secondary peaks decrease in amplitude as Λ increases, and $g(r)$ shows a shape close to the one of the diluted systems. For long rods, the particle extremes are simply uncorrelated, and thus the only dimension that will play a role in the case of random packings of long rods is the diameter. This also constitutes a probe that the final configuration achieved is not a nematic phase at all, but a glassy state. Upon application of Mechanical Contraction, long rods will be stacked in permanent positions due to their high probability of contact, producing glass states at very low packing fractions. Yet particles are interlocked, mechanical stability can not be ensured within the context of the MCM.

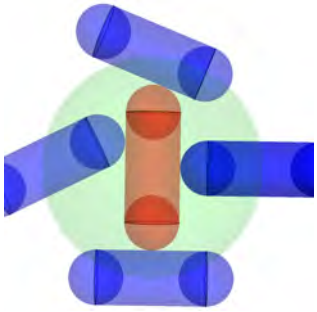

A minimal visualization of rods with $\Lambda = 3$ in contact with a central one. The green circle has the same radius as the length of the particle (notice that the distance from the center to one of the rod ends is $R + L/2$, not $L/2$).

Figure 2.15

2.3.2 ϵ *interpretation*

So far it has been assumed that the value that balances the rotational and linear components of the overlap removal velocity is well known, and results presented have taken into account the ϵ value as derived from a proper energy constraint.

However, this ϵ value did not have the particular meaning that has been given in the original Mechanical Contraction Method sources on which the present report is based ([18, 58]).

It is possible to make an interpretation of the energy constraint in terms of probability of overlap removing by means of rotations or linear movement of the particle's center of masses. Regarding the terms in the kinetic energy conservation during overlap removal, the ones that include the linear components of the speed can be assigned to a probability of remove overlap by means of a linear displacement of the rod, $P_{\boldsymbol{a}^{\mathrm{L}}}$. Equivalently, terms that include the rotational components of the velocity can be collected as a probability of removing the overlap by rotations of the rod $P_{\boldsymbol{a}^{\mathrm{R}}}$. Thus, the usage of numerically normalized components of the speed to 1 in mono-modal systems can be related then to the standard normalization of probability.

$$m\boldsymbol{a}_i^{\mathrm{L}} \cdot \boldsymbol{a}_i^{\mathrm{L}} + \epsilon \left((a_i^{\mathrm{R}_x})^2 + (a_i^{\mathrm{R}_y})^2 \right) = 1 \rightarrow P_{\boldsymbol{a}^{\mathrm{L}}} + P_{\boldsymbol{a}^{\mathrm{R}}} = 1 \tag{2.16}$$

Furthermore, expanding the terms in Equation 2.16 allows us to obtain an exact dependency of ϵ with Λ:

$$\begin{aligned} \epsilon &= \frac{I_{rod}}{V_{rod}} = \frac{\pi D^5 (\frac{\Lambda^3}{48} + \frac{\Lambda^2}{24} + \frac{3\Lambda}{64} + \frac{1}{60})}{\pi \frac{D^3}{4} (\Lambda - \frac{1}{3})} \\ \epsilon(\Lambda) &= D^2 \left(\frac{(\Lambda-1)^3}{12(\Lambda - 1/3)} + \frac{(\Lambda-1)^2}{6(\Lambda - 1/3)} + \frac{3(\Lambda-1)}{16(\Lambda - 1/3)} + \frac{1}{15(\Lambda - 1/3)} \right) \end{aligned} \tag{2.17}$$

The implications of Equation 2.17 are quite strong. First of all, the quadratic scaling of ϵ with particle aspect ratio implies that, upon a certain particle aspect ratio, all the overlaps will be removed by means of rotational components ($1 - \epsilon \left((a_i^{\mathrm{R}_x})^2 + (a_i^{\mathrm{R}_y})^2 \right) < 0$). Having a contact just parallel to the center of mass is quite improbable, and the available surface for contact increments with the length of the particles. It makes sense then that the overlap removal has a preference for rotational components the longer the particles are.

In other words, inertia dictates that for long particles, the tendency is rather to rotate than to translate: an overlap removal of a long rod only by means of center of mass translation is not optimal at all. Furthermore, in the limit of very long rods it is found that $\epsilon(\Lambda) = I(\text{thin rod})/m$: rotations completely dominate the overlap removal.

$$\lim_{\Lambda \to \infty} \epsilon(\Lambda) = \frac{1}{12} L^2 = I(\text{thin rod})/m \tag{2.18}$$

Taking into account that the volume has been set to be equal to the mass of the rods ($\rho = 1$) and that the volume of a long rod is very low with respect to its length, this limiting behavior makes sense. At high Λ, only inertia will dictate how the overlap is removed: $I/V_p \gg 1$. This situation recalls the starting configuration of the game *Mikado*, which starts with long rods being thrown under the effect of gravity. These long rods, upon touching, rotate and form the typical starting configuration of this game, which is a mess of randomly oriented long wood sticks.

Secondly, the final state of the system for non-spherical particles will be affected indeed by the biasing factor ϵ. By increasing the value of ϵ, more overlap removals by rotations will be induced, whereas by taking a too low value the overlap removal may be produced only by means of translations. If $\epsilon = 0$, rods would only remove their overlaps by translations, and thus the final packing fraction would be much lower (unphysical). This results in the fact that a MCM procedure performed for very large rods with a too low ϵ does not produce a significant number of box squashes, as far as the overlaps can not be removed when rotations are blocked after moving these long rods slightly closer. These results are clearly shown in Figure 2.16

Figure 2.17 shows a $3D$ representation of how modifying the ϵ parameter affects the final state of the system. As can be seen, the mean contact number depends on the ϵ quite heavily, and also the final packing fraction shows a dependence with this overlap removal biasing factor (specially for low Λ). Overloading ϵ, on the other hand, may induce slightly denser final configurations, but then all the physical meaning concerning the overlap removal would be lost. From all possible choices for ϵ, the one that follows the red line in Figure 2.17 is the one that provides the MCM with a physical rod-rod overlap removal.

The investigation conducted leads to a physical description of the overlap removal for rods within the MCM framework. The useful relation expressed in Equation 2.17, together with the parameters dependence and the smooth overlap removal bias factor β provide a reference for future calculations. The relation between the moment of inertia of the particle and its mass (via $\rho = 1$) finds applicability in general particle shapes (see Chapter 4 and Appendix B).

2.3.3 *Scan in Λ. Glass transition for rods*

Provided a strong and well defined MCM, a scan in particle aspect ratio must be performed. Results arising from the proper choice of ϵ should still retain the main

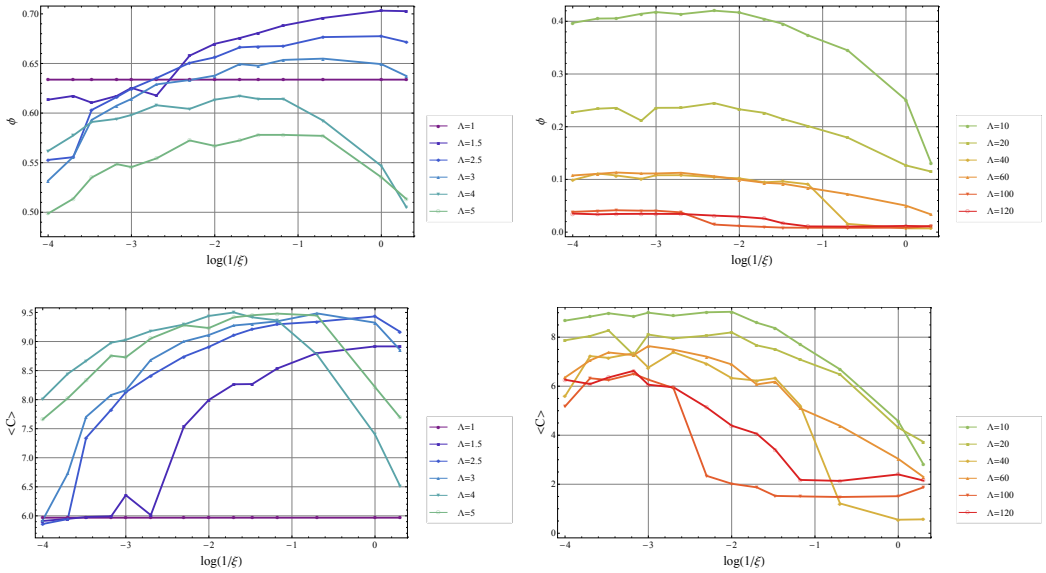

Figure 2.16: Final mean observables (ϕ and $\langle C \rangle$) of the system as a function of ϵ. Special attention to the scale of ϵ: $Log(1/\epsilon) = -3 \rightarrow \epsilon = 1000$, and so on. For the volume fraction, the red line represents the values obtained from the fitted expression for low Λ. Data collected for systems of 500 particles with $\beta = 0.1$ with a very high of tries to remove overlap (10^6).

features exhibited in previous MCM calculations. As it can be seen in Figure 2.18, for $\Lambda \approx 1.6$ the highest ϕ is obtained. This optimal aspect ratio for random packings in concordance with previous MCM results [18, 58], and thus it is a check in the feasibility of the $\epsilon(\Lambda)$ dependence derived in the research conducted.

Three different regions are defined regarding the final configuration of the packing of rods. For small sphere deviations, and as expected from the radial distribution function, the voids present in the final configuration for spheres are filled. The particle aspect ratio at which the packing fraction is the same as the one for spheres is such that $\epsilon(\Lambda = 3.66) = 1$: when the overlap has not a preference to be removed by means of linear or rotational velocity components. When this limit is reached, excluded volume effects start to play a role, decreasing ϕ as Λ increasing. Around $\Lambda \approx 3.6$ excluded volume dominates in the final random configuration, and thus the final packing fraction goes below the one of the spheres. In the long rod limit, the final packing fraction is very close to zero. Any attempt to move a particle will simply produce contact with other particles.

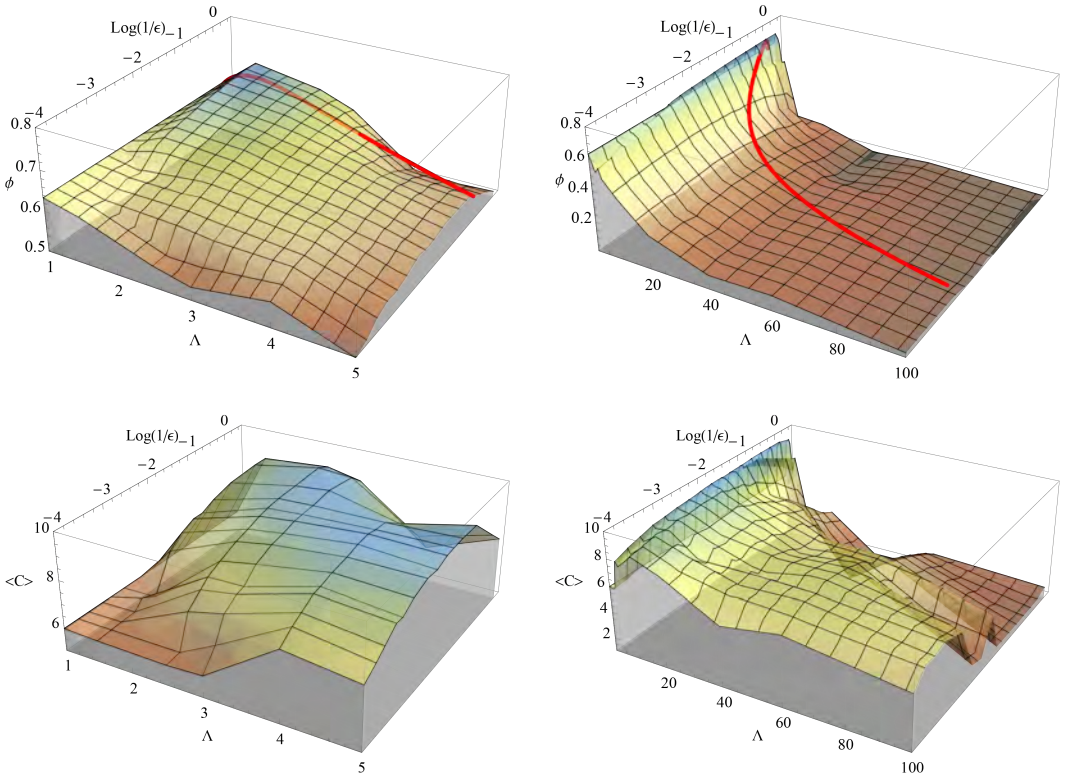

Figure 2.17: Final volume fraction (top) and mean contact number (bottom) as a function of the particle aspect ratio and the overlap removal biasing factor ϵ. Same scale as in Figure 2.16.

As expected from the results from spheres, the dependence of the final mean contact number with β is more significant than the one for the packing fraction (Figure 2.19), and it increases the smoother the overlap removal is set (the lower the β). This opposite dependence of ϕ and $\langle C \rangle$ is clearly shown in the inversion in the order of the series in Figures 2.18 and 2.19. However, the shape of the curve does not depend on the particular overlap removal rate value. Yet not shown in Figure 2.19, the error bars for the mean contact number tend to increase with the particle aspect ratio, meaning that the final configuration depends more on the starting configuration the larger the particles are. This may have been avoided by choosing a smaller starting density for long rods, or even an initial packing fraction dependent on particle aspect ratio.

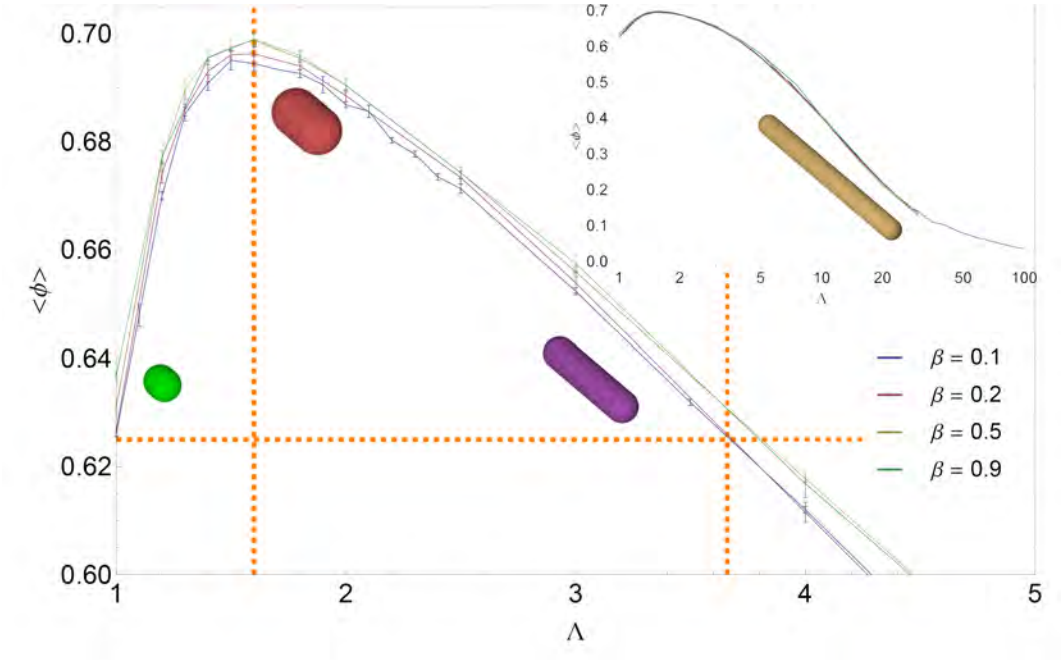

Figure 2.18: Final packing fraction as a function of the particle aspect ratio for a system of 1500 hard rods for different overlap removal rates, averaged over three different starting configurations. Inset image shows the whole range of particle aspect ratio, but with logarithmic scale in x.

2.3.3.1 *The Random Contact Equation*

Knowing the final ϕ and $\langle C \rangle$ values, it is possible to relate our simulations with the theoretical results stipulated by the *Random Contact Equation* (RCE) [31]. As the highest $\langle C \rangle$ is obtained for $\beta = 0.1$, this values will be used for comparing theory and simulations. The RCE can be interpreted as a geometrical equation of state of random packings with totally *uncorrelated contacts*:

$$\frac{\langle C \rangle}{\phi} = \frac{V_p}{V_{excl}} \tag{2.19}$$

As it is defined, the RCE assumes that the contacts on the particle are uncorrelated. This will only happen when the radial distribution function exhibits a step-like function shape, i.e. for long enough rods (see Figure 2.14). In the long rod limit, the RCE reads as [31]:

$$\frac{V_p}{V_{excl}} \equiv \frac{L}{D}\left(4\frac{D}{L} + \frac{3(L/D)}{3(L/D)+2}\right) \xrightarrow{L/D \gg 1} \frac{L}{D} \approx \frac{\langle C \rangle}{\phi} \tag{2.20}$$

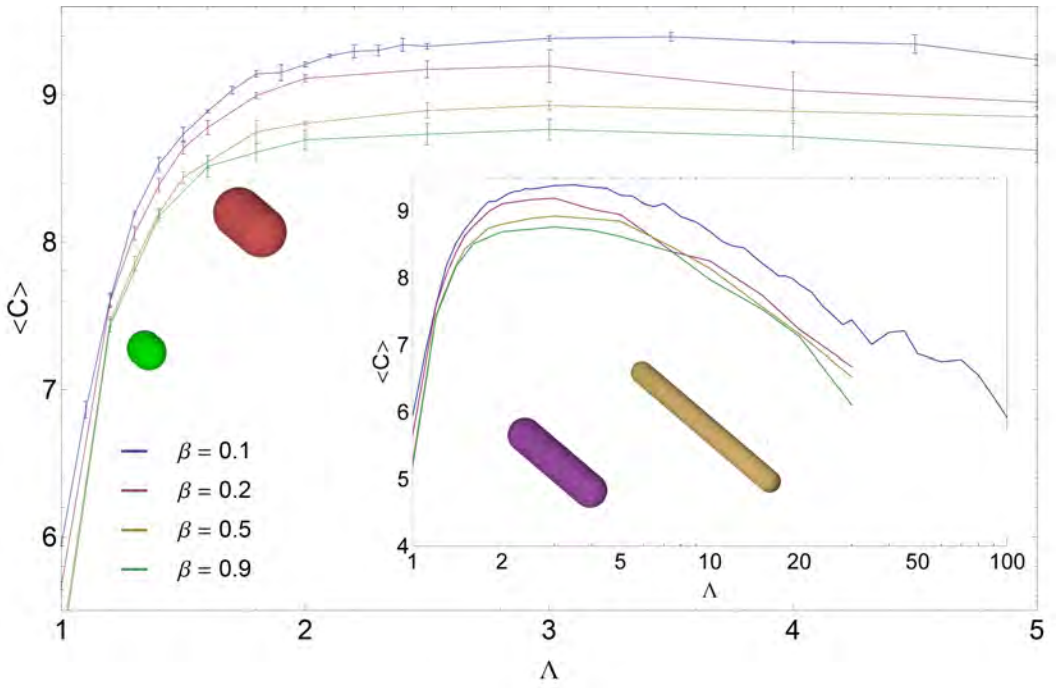

Figure 2.19: Final mean contact number as a function of the particle aspect ratio for a system of 1500 hard rods for different overlap removal rates, averaged over three different starting configurations. Inset image shows the whole range of particle aspect ratio, but with logarithm scale in x.

When two spheres are in contact, the number of ways in which a third one can be placed is lowered. The available surface for contact increases with the length of the rod, and thus the number of ways in which a third rod can be brought to contact with other two ones is higher than in the case of two spheres. Thus, contacts on a sphere will be more correlated in that sense than the ones on a long rod. This uncorrelation of contacts for long rods is also justified in terms of which relative amount of the excluded surface area due to the contact (S_C), which decays as particle elongates:

$$S_C = \frac{S_{contact}}{S_{particle}} \approx \frac{D^2}{DL} \tag{2.21}$$

Taking all this considerations into account, the outcome from the MCM can be used for establishing which is the limit for of long rods. This limit will be set when the relation between ϕ and $\langle C \rangle$ becomes linear.

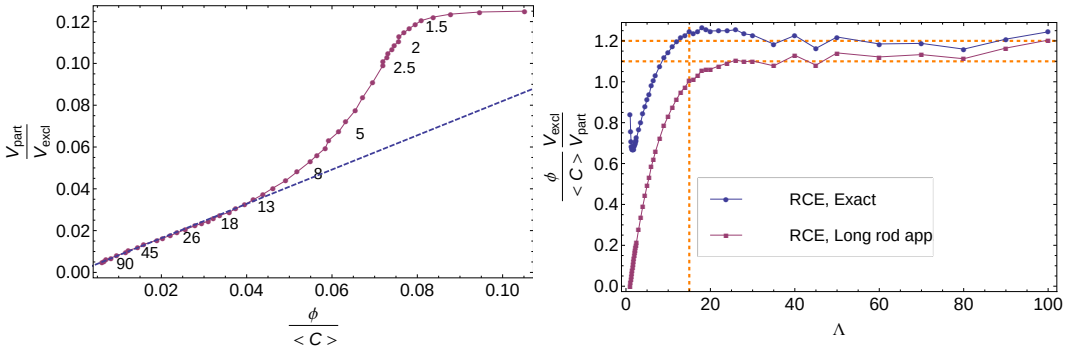

Figure 2.20: Two different checks of the feasibility of the RCE, using the final average observables (ϕ and $\langle c \rangle$) for 3 different starting random configurations of 1500 rods of different particle aspect ratio (Λ).

According to Figure 2.20, the long rod limit (uncorrelated contacts) is set for particle aspect ratio around $\Lambda \approx 15$. Depending on which correlation we look at, from this value on we get either a linear correlation (Figure 2.20, left) or we reach a plateau (Figure 2.20,right). Based on the RCE assumptions, we can set the limit for long rods from this length on, assuming that by long rods we mean that contacts on particle are uncorrelated. This agrees with the shape of the radial distribution functions obtained, being step-like function already for approximately $\Lambda > 15$ (see Figure 2.14). Why the RCE holds for such small values of Λ while being a $\Lambda \to \infty$ approximation is a very interesting discussion, out of the scope of this thesis.

2.3.3.2 *Asymptotic Equation of State for the glass transition*

The outcome of the MCM when a scan in particle aspect ratio is performed allows the construction of a glass-transition equation of state for rods. Assuming that the final state of a MCM simulation is a glass state of rods, the value of the final packing fraction actually provides some information about this state of matter and how a system approaches the glass state, even if no information about the pressure or the temperature is present in the MCM. A geometrical equation of state for the glass transition can be derived for rods, following the procedure by Peppin et al for hard spheres [77]. Knowing an expression for the low packing fraction limit and assuming an asymptotic behavior as the packing fraction goes to the final packing fractions, a complete equation can be obtained by *asymptotic matching*.

The *compressibility factor* $Z(\phi)$ accounts for deviations from the ideal gas behavior, and must also take into account the particle shape. In the limit of very low

packing fractions, it must tend to one, such that the ideal equation of gasses is retained. [78]

$$\Pi(\phi) = \frac{\phi}{V_p} k_B T Z(\phi) \tag{2.22}$$

, where ϕ and V_p stands as usual for the volume fraction and the volume of the particle respectively. Π is the pressure of the system, k_B is the Boltzmann constant and T is the temperature.

At low volume fractions, the compressibility factor can be expanded in the form of a virial series in the volume fraction. However, at higher concentrations the integrations become intractable and the coefficients are commonly obtained via computer simulations. By fitting the results of these simulations, Carnahan and Starling obtained the well-known approximate expression for the compressibility factor for spheres. This expression holds for $0 \leq \phi < 0.55$ [79]. A Carnahan-Starling (CS) -like equation of state is known for hard rods, which retrieves exactly the CS equation for $\Lambda = 1$ [80, 81]:

$$\begin{aligned} Z(\phi)_{\text{CS}} &= \tfrac{1+(3\alpha-2)\phi+(3\alpha^2-3\alpha+1)\phi^2-\alpha^2\phi^3}{(1-\phi)^3} \\ \alpha &= \tfrac{RS_p}{3V_p} \\ \alpha(\Lambda=1)=1 \quad &\rightarrow \quad Z(\phi)_{\text{CS}}^{\text{Spheres}} = \tfrac{1+\phi+\phi^2-\phi^3}{(1-\phi)^3} \end{aligned} \tag{2.23}$$

, where S_p is the surface of the particle and R is its radius.

The randomly packed state of matter implies that the pressure dominates over any thermal fluctuation: a divergence must occur near the final packing fraction in a mechanically stable hard particle configuration. Furthermore, considerations of the free volume available to a disordered system of hard spheres indicate that the pressure should diverge like $(\phi - \phi_{\text{Glass}})^{-1}$ as ϕ approaches ϕ_{Glass}. $Z(\phi)$ can be approximated near the glass transition (GT) as:

$$Z(\phi)_{\text{GT}} = \frac{\theta}{\phi_{\text{Glass}} - \phi} \tag{2.24}$$

The factor θ accounts for the exact way in which the asymptote is reached. Its particular value is known for spheres from molecular dynamic simulations ($\theta = 1.5$), but not for general particle shape. However, if we set the accuracy of our asymptotic matching up to third order, it turns out that the θ value does not play a role. The asymptotically matched equation of state can be written in terms of the coefficients a_1, a_2 , a_3.

$$Z(\phi) = \frac{1 + a_1\phi + a_2\phi + a_3\phi^3}{1 - \phi/\phi_{\text{Glass}}} \tag{2.25}$$

By taking the ϕ from the MCM simulations as ϕ_{Glass}, the limits $\phi \to 0$ and $\phi \to \phi_{\text{Glass}}$ are applied to Equations 2.23 and 2.25 to get the particular values of a_1, a_2 , a_3. Details of this mathematical procedure can be found in Appendix C. The first line in Figure 2.21 shows that actually the method provides good results for spheres. A too low polynomial order produces, at low packing fraction, already deviations from the CS equation: a first order approximation overestimates the asymptotic limit at low packing fractions. An approximation of second to third order is already good enough, even if it overestimates in this case the low packing fraction approximation near the glass transition. Discrepancies obtained from previous results [77] at fourth order are simply due to the lower packing fraction with used with respect to the MRS with $\phi = 0.64$. The second line in Figure 2.21 confirms the small deviations from a second to a third order polynomial approximation. As expected from the shape of Figure 2.18, first $Z(\phi)$ is displaced to the right and upon a certain limit ($\Lambda \approx 1.6$) it is displaced to the right, as the final packing fraction from the MCM lowers upon this value.

The interest of doing this asymptotic match is comparing how particle aspect ratio affects the glass transition. In order to compare all particle aspect ratios at once, a scaling of coordinates must be done. This is done by performing the change $\phi' \to \frac{\phi_{\text{Glass}}}{\phi}$, such that all fitted glass equations of state diverge at $\phi' = 1$.

The results exhibited in Figure 2.22 clearly show the behavior that is intuitively proper: the more anisotropic the particles are, the harder to compress. For very elongated rods, a fast compression (not allowing thermodynamic particle rearrangement) produces a very fast transition to a glass state. Furthermore, the glass transition is less peaked the shorter the rods are, meaning that due to their lower excluded volume they have a higher change to reorganize than the longer ones. Notice that this equation of state is not an accurate one, but a describes qualitatively the effect of particle elongation in the glass transition.

The meaning of the compressibility factor is retained in this equation of state. For very long rods, a small and fast compression of the system induces already a glassy state due to the fact that particles are kinetically trapped before they can reach thermodynamic equilibrium.

2.4 CONCLUSION AND OUTLOOK

We have simulated hard rods in the whole range of aspect ratio by MCM. A proper analysis of the overlap removal has provided more robustness to the method,

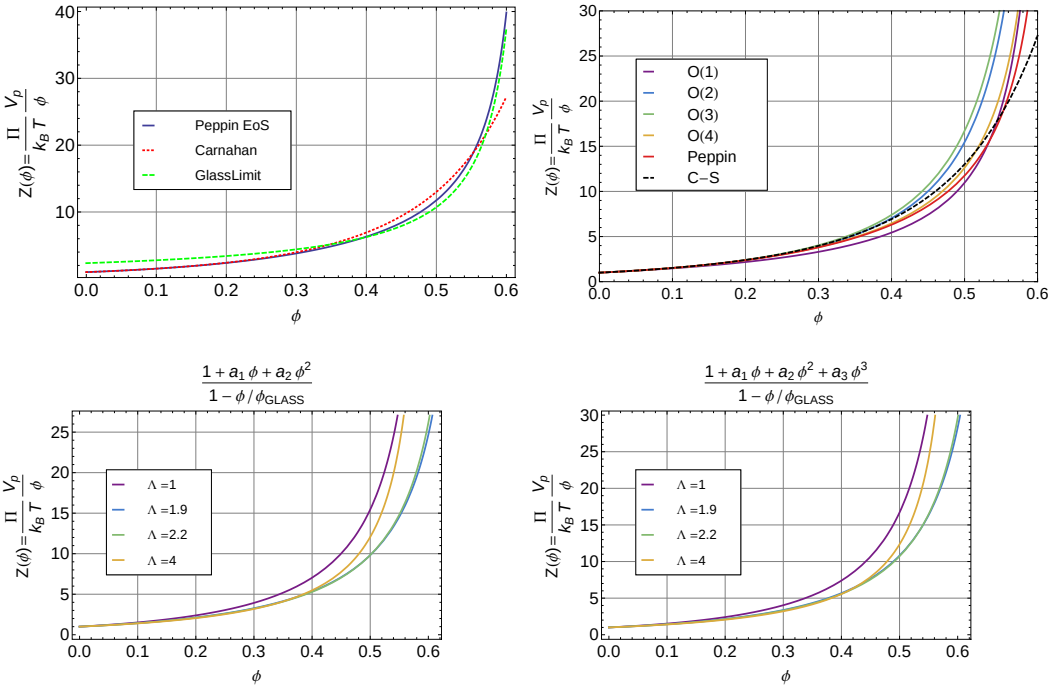

Figure 2.21: Top, left: the asymptotic matching as done by Peppin [77]. Top, right: comparison among different order of the polynomial describing the glass equation of state with the final packing fraction achieved via MCM for spheres. Bottom, left: second order approximation for the glass equation of state for different particle aspect ratios for the final packing fraction provided by the MCM. Bottom, right: as bottom right but up to third order.

while keeping the expected results from previous simulations. The set of parameters in which the MCM was initially dependent have been optimized and clarified. We have analyzed the final packing structure by means of the radial distribution function, which provided insight in the long rod limit. This long rod limit was later studied in details, connecting the simulations results with the theoretical predictions of the Random Contact Equation. Finally, an equation of state for the glass transition for rods of any aspect ratio has been studied, whose shape agrees with the definition of the compressibility factor.

Physical meaning have been brought to the large amount of variables in which the algorithm was dependent. Results from previous publications have been not only retrieved, but furthermore reinterpreted. The randomness of the final state of packings produced under the MCM algorithm has been probed, independently of

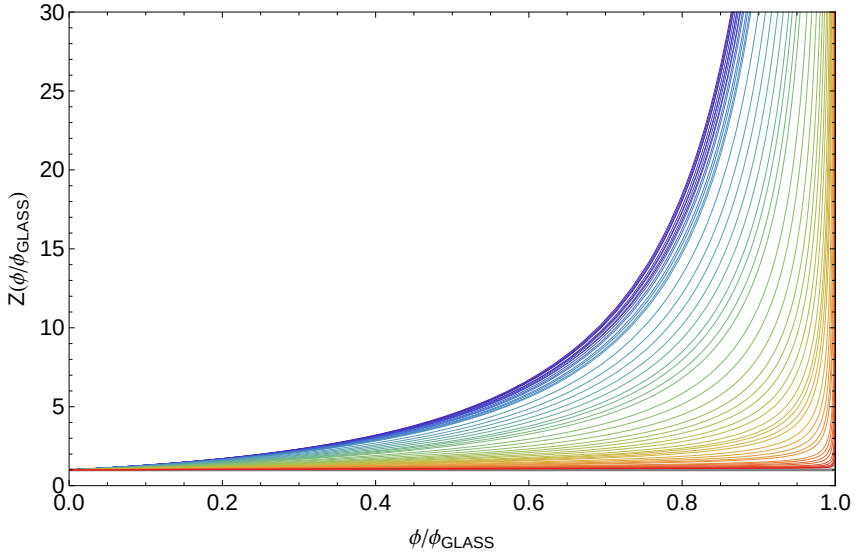

Figure 2.22: Scaled geometrical equations of state obtained from increasing particle aspect ratio in the rainbow sequence of colors: violet means $\Lambda = 1$ and red stands for $\Lambda = 120$.

the set of parameters chosen. Moreover, the magnitudes involved in the overlap removal have been provided to be meaningful, not just a mere choice of numerical values. Having proper definitions of the overlap removal direction, two overlapping particles have, different choices in which direction have a preference to remove overlap could have been done.

Whereas previous MCM studies employed Monte Carlo simulations once the mechanical equilibrium was reached, this project has focused on the MCM itself, proving that the packing fraction depends on how smooth the algorithm is performed. The random configurations achieved have been ensured to be random, but never claimed to be in the Maximally Random State (the higher packing fraction within a random configuration). However, by means of how it is produced, the final state is probably one of the most random configurations achievable.

A connection has been made for defining the *long rod* limit from the point of view of the random state of matter. This lower bound has been set connecting the results of a well defined MCM with the Random Contact Equation and the radial distribution functions obtained. The geometrical equation of state for the gas-liquid-glass transition in the whole range of rod particle aspect ratio must not be the most accurate one, but produces proper quantitative results. Moreover, as-

suming that the trend exhibited for a third order approximation must remain in a fourth order approximation, an finer equation for the glass transition could be obtained by calculating the equivalent to the θ term present for spheres.

All the results presented concern mono modal systems, but the formalism developed here is general. The understanding of the overlap removal probability (via ϵ) may be extended to bimodal random packings, where the volume (equivalently, the mass) of each particle will determine the relative speed at which they remove the overlap: it is expected that particles with less mass (volume) will move faster upon collision. The proper considerations for the energy constraint may allow the MCM to be well defined for system of non equal particles, both in size and shape. Even the results for bimodal packings of spheres would improve with the velocity component dependence on particle mass: being this not really necessary for particles with similar volume, it would be really critical for spheres of very different size. Furthermore, following the steps in the derivations presented we can see that it may be even possible to properly simulate system of particles with equal volume but different density: heavier particles would simply remove less overlap that the lighter ones.

As it was commented, an even more diluted starting configuration may be necessary for very long rods. Moreover, the way in which the boundaries are squashed may influence the final random configuration. Thus, an easy test to be made in the future is a linear scaling of the box, instead of the faster box-size dependent scaling used.

Furthermore, for rods it may be worth to study initial configurations of an intermediate density of ordered (equally oriented) rods. Thus, an algorithm modification that produces small random deviations of the orientation, together with the Mechanical Contraction Method, could allow the study of local defects on Nematic Liquid Crystals. Furthermore, a totally hybrid algorithm between the MCM here described and a NVT Monte Carlo simulation could actually balance which final configuration is obtained in terms of how long do we let our particles reorganize before the box is scaled. Such an algorithm would balance the effect of the simulated Brownian Motion (via Monte Carlo) with the forced blocking of particle movements induced via MCM.

3 RANDOM PACKINGS IN HARD BOUNDARY CONDITIONS VIA MECHANICAL CONTRACTION

In this chapter, random packings of spherocylinders are generated via the Mechanical Contraction Method (MCM) in hard boundary conditions. First, random packings of particles are generated inside a hard cylinder with hard boundaries and also in cylinder periodic in the z-axis. Additionally, an algorithm is defined to generate random packings within a container with the shape of a hard wedge.

The outcome from both simulations is comparable with experimental results in which the boundaries of the system affect the local particle distribution. A general method to particle-wall detection within the MCM framework is here also presented.

3.1 RELEVANCE OF HARD BOUNDARIES

How hard boundaries affect a system is indeed an interesting topic [65, 82]: periodic boundary conditions are an imaginary situation never reachable in real life. Moreover, experiments on random packings of particles will be always performed in a recipient [21, 29, 35, 83]. Periodicity is normally assumed because experimental set-ups should be performed in a way that the wall effects are negligible when observables such as packing density, final mean contact number or radial distribution functions are measured. A large enough system usually accounts for this.

The present chapter provides insight in the actual influence of hard boundary conditions on random packing of particles by comparing the results with the ideal case of periodic boundaries. The volume fraction with hard boundaries will be always lower than the one in periodic boundary conditions, as far as not a single part of the particle can leave the box any longer: the walls themselves are restricting a certain a volume to the particles. How large the influence of the boundary is clearly of interest due to the connection with real experiments: an experimental setup can actually be simulated. A simulation with a large enough number of particles may, in principle, recover the results of the periodic boundary conditions.

Already the early experiments in the search of the Random Close Packing (RCP) limit for spheres were performed inside a cylindrical container [29]. Experimental setups for different particle shapes are also performed within a cylinder [21, 35, 83]. Recently, it has been stated that helical and zig-zag rearrangements of spheres within a thin cylinder is mainly driven by the geometry of the particles [66], and this can also happen for different particle shapes [84]. Finally, the final packing configuration of rods in a cylinder could be regarded as the network of magnetizable particles for a magnetic separation chamber (see Section 1.4).

On the other hand, the interest of a sharp corner relates to how some experimental techniques induce order in colloidal crystals formation. When particles are randomly placed within a wedge, it can be expected that the sharp corner will induce some order in the particle configuration. Indeed, some colloidal crystallization techniques actually use a sharp corner to induce order, which is reflected, for instance, in the methods named *drying droplet* (DD), *horizontal deposition* (HD) and *Flow-Controlled vertical deposition* [85]. How strong the effect of the geometry is in this experiments can be studied via computer simulations using MCM.

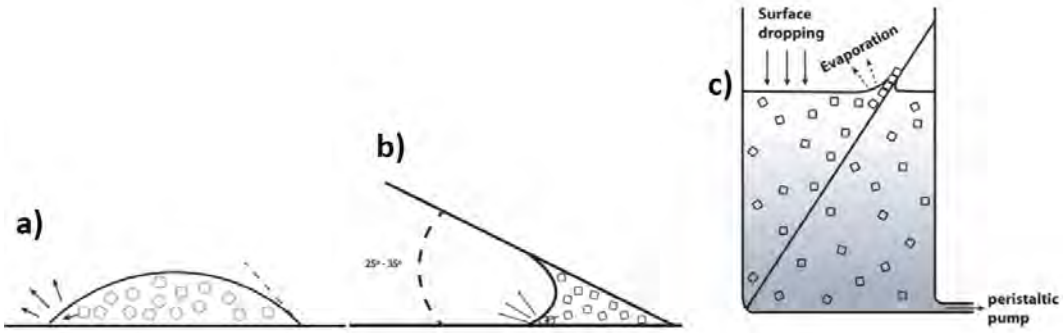

Figure 3.1: Illustrations of the side view of setups used in Convective Assembly experiments with a) the DD method b) the HD method and c) the FCVD method. Image from [85]

One of the main steps in MCM is the scaling of particle positions: starting from an initial configuration of randomly distributed particles, the boundaries are squashed and particles come closer and closer as the routine is performed. For periodic boundary conditions, this squash can only lead to particle-particle overlaps, which are removed according to a certain constraint (see Chapter 2). When hard boundaries play a role, the position rescaling and particles overlap removal can also lead to particle-boundary overlaps, which need to be removed. Under hard

boundary conditions two kind of overlaps can take place: particle-particle and particle-wall. Modifications of the general algorithm are therefore needed when the boundaries are not periodic. As in Chapter 2, the methods described in the present chapter are general, but all simulations were done for mono-modal random packings.

3.2 CYLINDRICAL BOUNDARY CONDITIONS

The present section goes into the details of generating a random packing within a cylinder of length L_{cyl} and diameter D_{cyl} via Mechanical Contraction Method. The motivation behind these simulations is clear regarding the discussion made in the introduction of the present chapter.

3.2.1 *Algorithm modifications*

A change in the geometry of the simulation box will require modifications of the general algorithm defined in Chapter 2. The particle-hard wall contact detection and the corresponding overlap removal need to be incorporated within the steps of the Mechanical Contraction Method.

3.2.1.1 *Container description. The virtual particle method.*

First it must be defined the origin of the reference frame of the particular container. For the cylinder, it was chosen as its geometrical center which is at half its length and in the center of the circular base. The endpoints $\boldsymbol{p}_{+,i}$ and $\boldsymbol{p}_{-,i}$ of a rod with centroid in $\boldsymbol{x}_i$, length L and orientation $\hat{r}_i$ will determine the region of possible hard boundary contact. As explained in details in Chapter 2, these endpoints are given by:

$$\boldsymbol{p}_{\pm,i} = \boldsymbol{x}_i \pm \frac{1}{2} L_i \hat{r}_i \tag{3.1}$$

Two different hard boundaries can be set: in the radial coordinates and in the z-axis. In order to avoid penetration of rods towards the top and bottom of the cylindrical boundary, particles are pushed back when any of the z-coordinates of their end points satisfy $|p_{i,\pm,z}| > \frac{1}{2} L_{\text{cyl}}$. This is not taken into account when only radial hard boundaries play a role, because then the cylinder is considered to be periodic in the z direction.

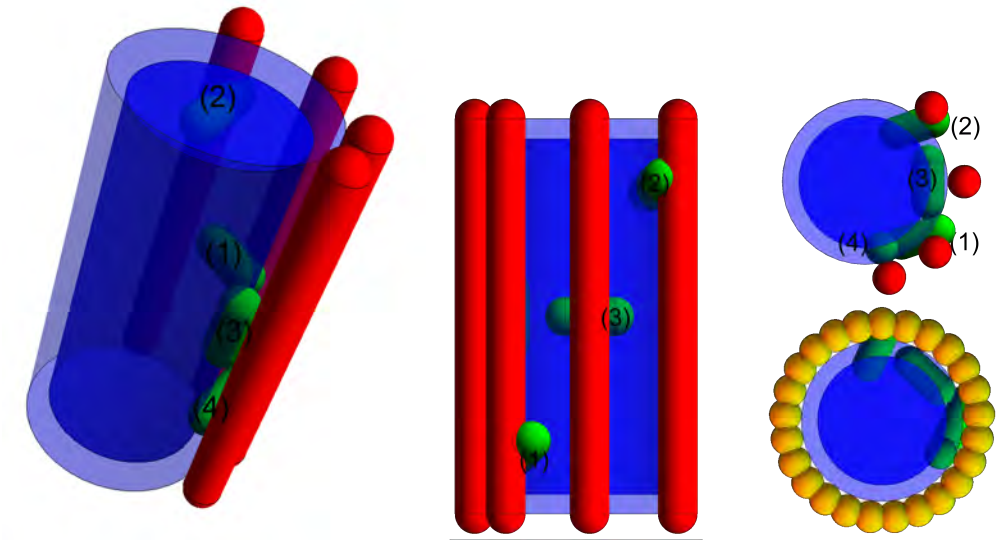

Figure 3.2: The rod-wall contact detection algorithm for different wall penetration situations labeled from (1) to (4). Lighter blue stands for the wall-contact region: any rod whose centroid is within this region will have a chance of contacting or penetrating the wall. The virtual rods placed for the wall overlap removal are plotted in red. Left, a global perspective. Right: side and top views. The second plot of the top view with the yellow circle of spheres represents how the hard boundary is taken into account as a mesh of wall-touching spherocylinders with length L_{cyl}.

Any time a contact between a rod and a hard-wall is detected (see text below), a virtual rod is placed. Figure 3.2 presents how virtual rod for the the wall-contact detection is placed:

- (1) and (2) are randomly oriented rods penetrating the hard radial boundary.
- (3) is a rod whose orientation is perpendicular to the z-axis, and any rod whose x,y coordinates of the centroid are further from this point will be in the region of possible wall contact.
- (4) is a rod whose orientation is parallel to the z-axis. Together with (3), they represent the maximum radial coordinates for the rod centroid coordinates.

From the limiting cases (3) and (4), it is not difficult to set the actual conditions that requires the contact detection algorithm to be called. Equation 3.2 presents the inequalities from which a rod may be in contact with the hard boundaries. The first line stands for the radial coordinates, whereas the second one holds for

the z-axis (only required when the cylinder is not periodic in length). When a particle is in the contact region with the cylinder wall (radial boundary condition), a virtual rod with the length of the cylinder (L_{cyl}) and the same radius of the particle (R_i) is placed in the appropriate coordinates (see Figure 3.2). Then, the considered rod-rod contact detection is performed [74].

$$\begin{aligned} (\boldsymbol{p}_{x,\pm,i})^2 + (\boldsymbol{p}_{y,\pm,i})^2 &> \left(\frac{1}{2}D_{\text{cyl}} - R_i\right)^2 \\ \mid \boldsymbol{p}_{z,\pm,i} \mid &> \frac{1}{2}L_{\text{cyl}} \end{aligned} \tag{3.2}$$

3.2.1.2 *Starting configuration*

As happened in periodic boundary conditions, the starting configuration for the MCM is a collection of randomly distributed particles at low packing fraction. The starting random distribution of particles inside a cylinder is achieved by generating the x, y coordinates of the centroid of rod i randomly distributed within a circle of radius $\frac{1}{2}D_{\text{cyl}} - R_i$, and by randomly positioned the height of the centroid such that $\mid z_i \mid < L_{\text{cyl}} - R_i$, with R_i the radius of the considered particle. The contact detection algorithm is called any time a rod is placed in the region of possible contact (darker blue volume in Figure 3.2). When contact is found in the generation of the starting configuration, it is simply rejected. As happened for periodic boundary conditions (Chapter 2), we actually do a Random Sequential addition of particles, in this case within a cylinder. The same will hold for any other container shape.

3.2.1.3 *Container squash*

Concerning the squash of the cylindrical boundaries, the diameter D_{cyl} is kept constant, whereas its length (L_{cyl}) is scaled by a factor α. This implies that scaling of particle positions only happens in the z-axis, and not in the radial coordinates of the cylinder, providing a constant curvature of the cylinder during the simulation. Particles are contracted towards the geometrical center of the cylinder as the squash of the boundaries takes place, as in the cubic periodic conditions particles would approach the geometrical center of the box. The centroid position will be scaled in each iteration as:

$$\begin{aligned} V_{\text{Box}}^{m+1} &= \alpha V_{\text{Box}}^{m} \\ \boldsymbol{x}_i^{m+1} &= (x_i^m, y_i^m, z_i^m L_{\text{cyl}}(1-\alpha)) \end{aligned} \tag{3.3}$$

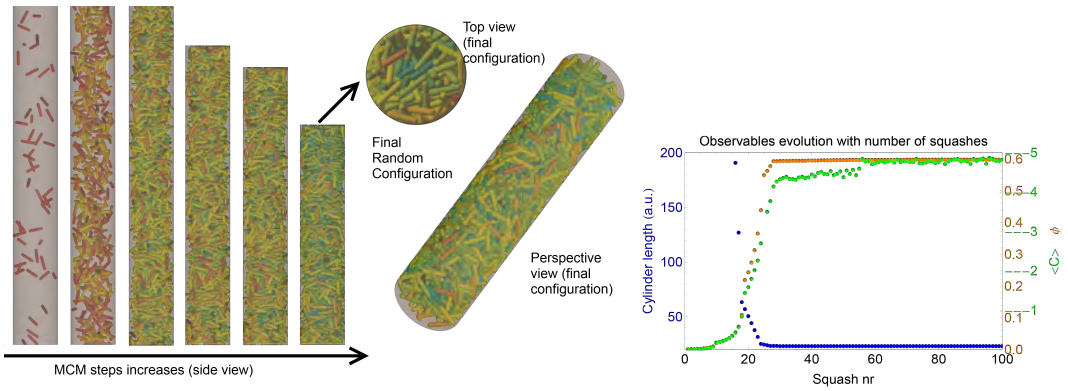

Figure 3.3: Left: Graphical visualization of the Mechanical Contraction Method with hard cylindrical boundary conditions, for a system of 1500 spherocylinders with aspect ratio 5 being squashed in a cylinder with diameter 15. Right: cylinder length L_{cyl}, packing fraction ϕ and mean contact number $\langle C \rangle$ evolution with the number of cylinder scalings (squashes).

Figure 3.3 shows graphically how the squashing of particles within the cylinder is performed, as well as the change on the main system variables. Notice that the units referring the diameter of the cylinder are arbitrary units of length; all dimensions of the system are set with respect to the diameter of the particles. As expected, as the cylinder shrinks in length the volume fraction increases, and so does the mean contact number following a similar trend. This packing fraction-contact number dependence was already observed in periodic boundary conditions, and the difference in the observables evolution shape is due to the way in which the container is compressed (compare with Figure 2.2).

Due to how the container scaling takes place, a balance between the number of particles in the initial configuration and the cylinder diameter is needed to avoid too flat final configurations. From how the squash of the boundaries is performed, it is expected that the dependence of the packing fraction with the number of particles and container diameter for the totally hard cylinder is higher than the one for the cylinder periodic in length. In any case, for very large cylinder diameters the number of particles needs to be very high, such that a relatively big amount of particle layers are present in the final random packing. Notice that periodic boundary conditions are actually recovered in the limiting case ($D \to \infty$, $N \to \infty$).

3.2.2 *Simulation results in a totally hard cylinder*

The behavior of the algorithm was checked by varying the overlap removal rate β, whose role in the algorithm is biasing how much of the overlap is removed at each one of the overlap removal steps (see Section 2.1.2). As the overlap removal rate increases, the contact number decays and the volume fraction gets higher (Figure 3.5), which is the same trend exhibited for periodic boundary conditions. The rest of the parameters on which the MCM depends were also checked, and the results always showed the same trend as for the periodic boundary conditions.

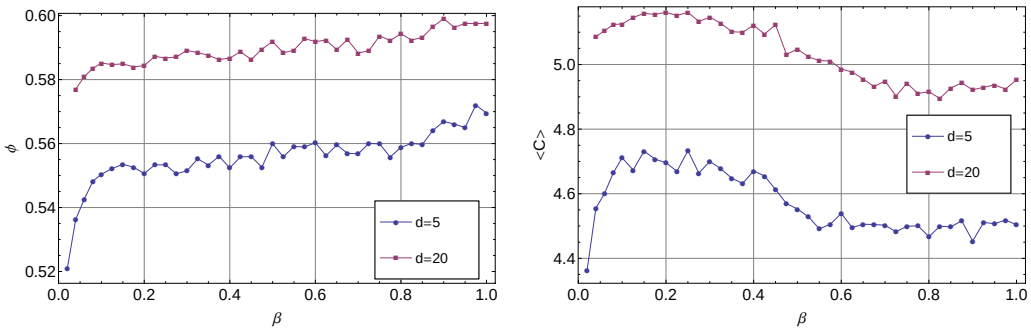

Figure 3.4: Final packing fraction (left) and mean contact number (right) as a function of the removal overlap rate factor (β) for a system of 1500 hard spheres undergoing a Mechanical Contraction Method in hard cylinder boundary conditions.

Simulations were performed in a hard cylinder with different curvature for varying the particle aspect ratio with a constant number of particles. (Figure 3.5). A peak is present for ϕ and $\langle C \rangle$ as the D_{cyl} increases, but then their value decays due to too flat final configurations (not enough layers of particles between the cylinder ends in the final configuration). A trend in increasing the nematic order parameter S_2 as the cylinder diameter decreases is also exhibited: in a very thin cylinder, particles can only occupy less space if they align. Yet, S_2 for diameters high enough was lower than 0.2, meaning that for rods not partial orientational ordering is achieved under MCM procedure within totally hard cylinder boundaries. The peculiarities at low values of D_{cyl} for all observables exhibited in Figure 3.5 will be treated in detail in the next section.

It can be observed that the maximum for the mean contact number $\langle C \rangle$ and packing fraction ϕ displaces to the left as the particle aspect ratio Λ increases. This dependence of the observables with the diameter of the radial boundary can be

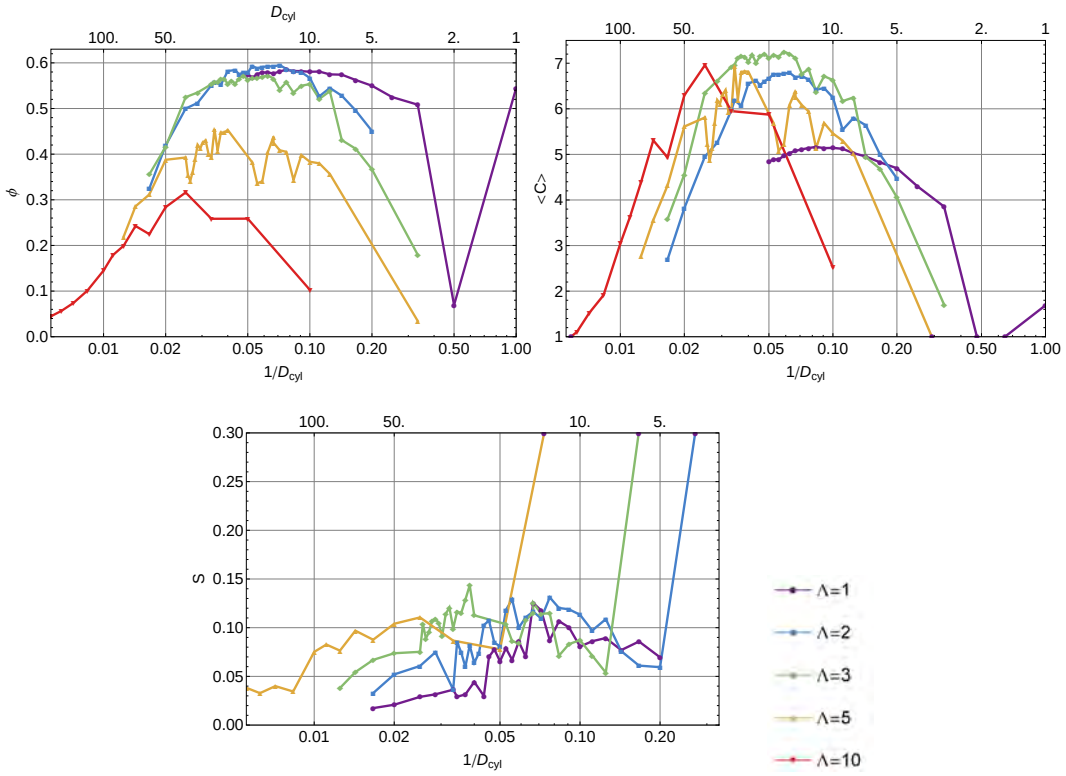

Figure 3.5: Final packing fraction (top, left), mean contact number (top, right) and nematic order parameter (bottom) as a function of the boundary curvature ($\frac{1}{D_{cyl}}$) for a system of 1500 rods of different particle aspect ratio undergoing a Mechanical Contraction Method in hard cylinder boundary conditions.

avoided if the effect of the curvature can be isolated, resembling a situation closer to the one of the actual experiments.

3.2.3 *Simulation results in a z-periodic cylinder*

With the purpose of isolating as much as possible the effect of the curvature of the boundary, simulations were performed in cylinder periodic in the z-axis with increasing number of particles with D_{cyl} for several particle aspect ratios (Figure 3.7). This would approach more the actual experimental setups, as discussed in the introduction.

First, the results obtained for spheres are explained in detail. Figure 3.6 shows a graph with the same axes presented for experimental setups in the search of the

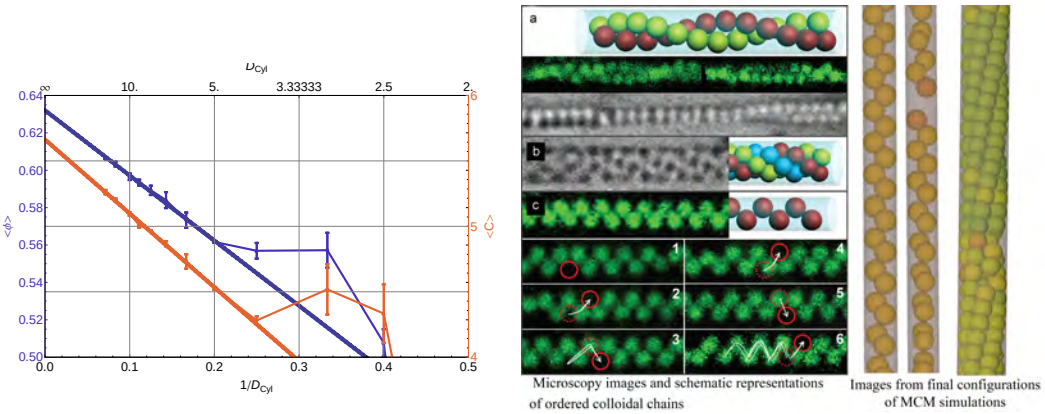

Figure 3.6: Left: final mean observables (packing fraction and contact number) for simulations using Mechanical Contraction Method (MCM) with hard radial boundary conditions with increasing number of particles as the curvature of the boundary decreases.Right: comparison among Helical Colloidal Sphere Structures through Thermo-Reversible Co-Assembly with Molecular Microtubes and the the same organizations achieved by performing a MCM simulation for spheres with hard radial boundary conditions with $D_{\text{cyl}} = 1.5$ and $D_{\text{cyl}} = 2.5$, referred to spheres with $D = 1.0$

RCP of spheres [29]. Once a certain cylinder diameter is reached, a tendency to increase the packing fraction as the curvature goes to zero is observed, just as in the early experimental setups to get the RCP limit. In the limit of small cylinder diameters, a geometrically induced ordering of particles is observed, showing the same characteristics as recent experiments in the confinement effect of colloidal spheres in cylinders [66].

By extrapolating the linear fit of the packing fraction for values far from the geometrical reorganization, a limiting value for the RCP can be obtained as the intersection of the linear with the y axis. As expected, the trend followed by the packing fraction and the mean contact number is the same. The linear fit provides values of $\phi = 0.632$ and $\langle C \rangle = 5.663$ when $D_{\text{cyl}} = 0$, in concordance with the calculations performed in periodic boundary conditions (Chapter 2) which were 0.623 ± 0.0004 and $\langle C \rangle = 5.674 \pm 0.0152$, and also with the value obtained from the same procedure in an experimental set-up (0.6366 ± 0.0005 , [29]).

The same study can be extended to non spherical particles (Figure 3.7). The trend followed by all particle aspect ratios studied is the same as for spheres in a z-periodic cylinder, except for the simulations for $\Lambda = 4$. The peaked shape in this

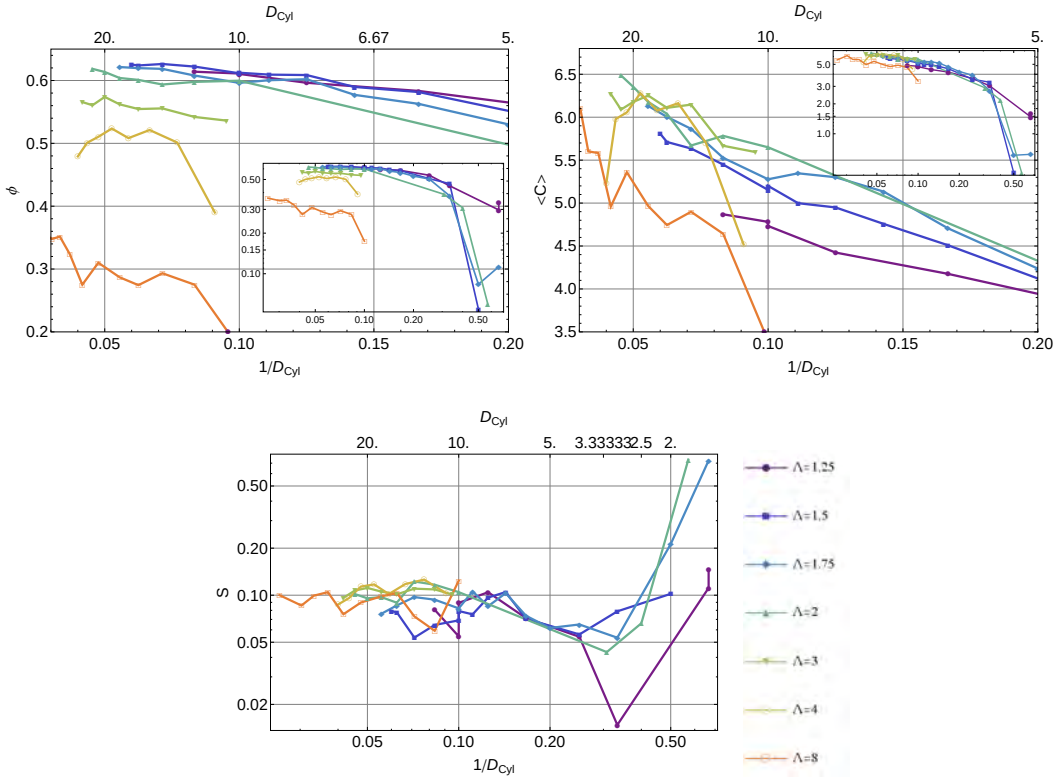

Figure 3.7: Mean observables of the system (final packing fraction ϕ, mean contact $\langle C \rangle$ number and nematic order parameterS_2) as functions of radial boundary curvature ($1/D_{\text{cyl}}$). The main plots for ϕ and $\langle C \rangle$ are in a linear scale, whereas in the inset plots both axes are in a logarithm scale. The plot for S also has both axes in a logarithm scale. Number of particles in the system increases with the diameter of the cylindrical container.

series of data indicates that even considering periodicity in z, the increase of the number of particles in the simulation with D_{cyl} was not big enough. An explosion in the nematic order parameter S_2 for low cylinder diameters is clearly present, meaning that geometric rearrangement takes place for non spherical particles.

For all Λ studied except $\Lambda = 4$, an almost linear trend for both the contact number and the packing fraction when extrapolating to infinity the diameter of the container is obtained (Figure 3.7). The trend for ϕ and $\langle C \rangle$ when $D \to \infty$ has the same shape in periodic boundary conditions (Figure 3.8, left). The lowering in the contact number accounts for the fact particle-wall contacts were not taken into account. However, the limiting value $\phi_{D\to\infty}$ for rods is also lowered with respect

to the case of periodic boundary conditions. As this did not happen for spheres, it can be concluded that the effect of a hard boundary is enhanced by the anisotropy of the particles.

The combined effect hard walls-anisotropy of particles can be further exploited in the search of local particle rearrangements. The deviation from final volume fraction with respect to the one of the periodic limit tends to balance upon a certain ratio of the particle aspect ratio Λ over D_{Cyl} (Figure 3.8, right). Which kind of local particle configurations are present within this region is out of the scope of this project. Furthermore, plots are not presented with averaged values due to the long time that these simulations take.

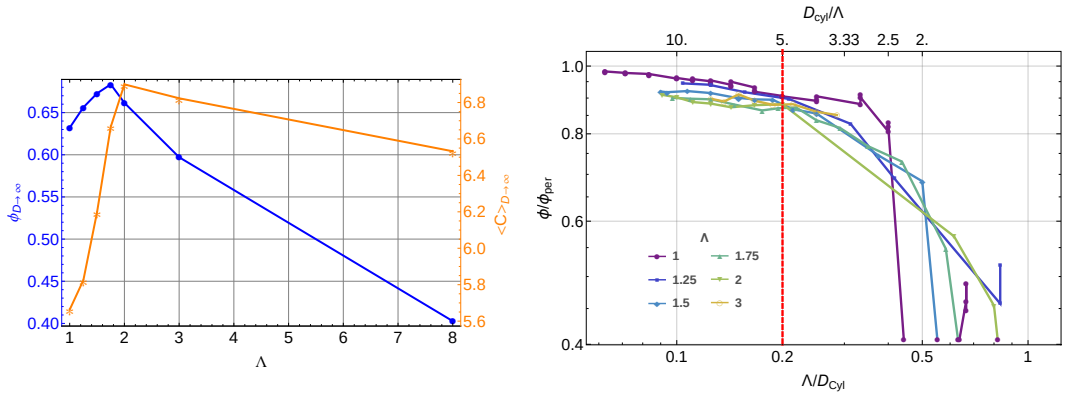

Figure 3.8: Left: ϕ and $\langle C \rangle$ against Λ from the fitted linear model of the MCM insider a z-periodic cylinder. Right: deviation from the periodic limit versus Λ/D_{Cyl}. This ratio accounts both for the anisotropy of the particles and the curvature of the walls.

3.3 RANDOM PACKINGS CONFINED IN A WEDGE

Provided a method to describe the hard boundaries (the *virtual rod method*), more constraint boundaries for random packings via MCM can be set. Concretely, here a container with the shape of a wedge is studied. As discussed in the introduction of the present chapter, the sharp corner of a wedge container is used in particle assembly techniques. How relevant this geometric effect is can be studied within an algorithm that provides random configurations under periodic boundary conditions.

3.3.1 *Algorithm modifications*

As happened with the generation of random packing of rods within a cylinder, the general schema of the MCM requires some modifications that account for the presence of the hard walls. In this case, the wedge is describe as a set of planes, and the virtual rod method is used in the inclined plane.

3.3.1.1 *Container description and initial configuration.*

Given a wedge with base, height and depth w_{b},w_{h} and w_{d}, the actual volume of the rods' centroids will be restricted to a certain inner wedge coordinates, described by $w_{\mathrm{b,in}}$,$w_{\mathrm{h,in}}$ and $w_{\mathrm{d,in}}$. The particular values will be given in terms of two variables, Δx and Δy which clearly depend on the angle θ of the wedge. Δx and Δy are symmetric with respect to $\theta = \frac{\pi}{4}$, as expected for a right triangle. It has been chosen to define the aspect ratio γ of the wedge as $\gamma = w_{\mathrm{b}}/w_{\mathrm{d}}$. With the three variables w_{b}, θ and γ the geometry of the outer and inner wedge for a rod i with radius R_i is perfectly defined. The geometry of the wedge and the different values that describe its shape are given in Figure 3.9.

As in all other cases, the starting configuration for the MCM is a low packing fraction collection of rods randomly distributed within the wedge. This initial configuration will be given in terms of the inner wedge coordinates and the rods endpoints ($\boldsymbol{p}_{\pm,i}$) as:

$$\begin{aligned} 0 < \boldsymbol{p}_{x,\pm,i} &< -w_{\mathrm{b,in}} \\ 0 < \boldsymbol{p}_{y,\pm,i} &< (\tan\theta \boldsymbol{p}_{x,\pm,i} + w_{\mathrm{h,in}}) \\ \mid \boldsymbol{p}_{z,\pm,i} \mid &< \frac{w_{\mathrm{d,in}}}{2} \end{aligned} \tag{3.4}$$

Here, $\boldsymbol{p}_{k,\pm,i}$ is the kth-component of the endpoints ($\pm$) of a rod i, referred to a system with origin of coordinates in the middle point of the right angle of the wedge (purple arrows in Figure 3.9). The position of the center of masses of the rods $\boldsymbol{x}_i$ are randomly regenerated until there are no overlaps among them and the conditions in Equation 3.4 are satisfied for all rods. The rod rod contact detection performed is, as in the other algorithm modifications, the one defined by Vega and Lago [74].

An important remark to take into account when dealing with the rather strong boundary conditions imposed by a hard wedge is how big the inaccessible volume to the particles inside is.

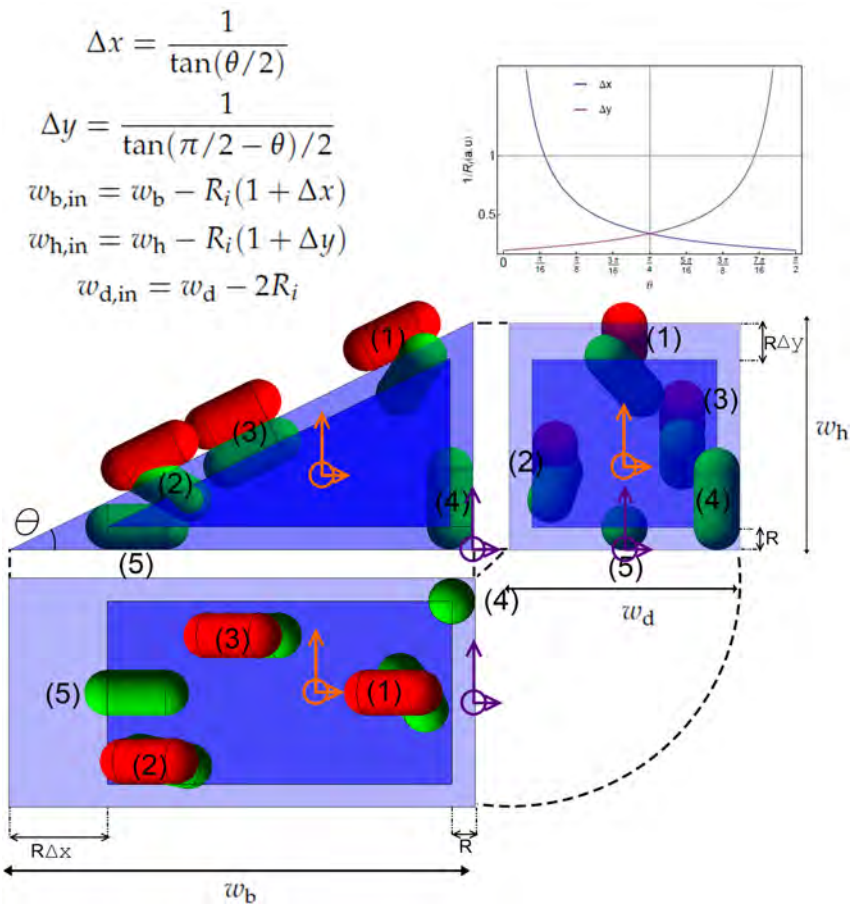

Figure 3.9: Different perspectives of a wedge and the parameters involved in its description. In lighter blue is the inaccessible volume for the rods centroid (contact region). In purple is the origin for the random starting configuration, and indicated in orange are the barycentric coordinates. Several rods inside the wedge are also presented (green) and labeled from (1) to (5), with their corresponding virtual rod for overlap removal.

3.3.1.2 *Container scaling and virtual rod method.*

Provided this starting configuration of non overlapping rods, the centers of mass are translated towards the barycenter of the wedge (orange arrows in Figure 3.9). Squash of particles is performed towards this point as the volume of the wedge is reduced. This contraction is performed in such a way that the shape of the wedge does not change (both γ and θ do not change). Provided a standard scaling factor

α, the values that define how the wedge and the coordinates are scaled in a step $(m+1)$ with respect to the previous one (m) are given by:

$$\begin{gathered} V_{\text{Box}}^{m+1} = \alpha V_{\text{Box}}^{m} \\ w_{\text{b}}^{m+1} = w_{\text{b}}^{m}\alpha^{1/3} \qquad w_{\text{h}}^{m+1} = w_{\text{b}}^{m+1}\tan\theta \qquad w_{\text{d}}^{m+1} = w_{\text{b}}^{m+1}/\gamma \end{gathered} \tag{3.5}$$

The particles and boundaries within the MCM procedure can lead not only particle-particle overlaps, but also contacts with the hard wedge boundaries, as it happened for the cylindrical boundary conditions. For all the planes parallel to the reference frame , any time that a rod endpoint is beyond the overlap region, its centroid is pushed back the distance necessary for being just in contact with the considered plane. Let k be the set of x, y, z coordinates, and $k_{\pm}$ the maximum and minimum values that the rod centroid coordinates can have. Then, the minimum particle movement for removing wall penetration with a plane will be given as:

$$\boldsymbol{x}_{k,i} = \boldsymbol{x}_{k,i} - \left(\boldsymbol{p}_{k,\pm,i} - k_{\pm}\right) \tag{3.6}$$

On the other hand, when a rod is in contact or overlap with the slope, an identical virtual rod is placed parallel to the slope (Figure 3.9), in a position such that the overlap between the rod that is out of the wedge and the virtual rod is maximum. The center of mass of this virtual rod is given by Equation 3.7, and how this position is derived can be found in Appendix D.

$$\boldsymbol{x}_{i,\text{virtual}} = \begin{pmatrix} \cos\theta\left(\left(\boldsymbol{p}_{x,i}\cos\theta + (\boldsymbol{p}_{y,i} - wh/3)\sin\theta - R_i\tan\theta\right)\right. \\ \sin\theta\left(\left(\boldsymbol{p}_{x,i} + wb/3\right)\cos\theta + \boldsymbol{p}_{y,i}\sin\theta + R_i/\tan\theta\right) \\ \boldsymbol{p}_{z,i} \end{pmatrix} \tag{3.7}$$

Once the virtual rod is placed, the contact detection algorithm between rods is then called [74], and the overlap is removed in the usual fashion. The possible contacts are represented in Figure 3.9, such that:

- (1) and (2) are randomly oriented rods penetrating the slope.
- (3) is a rod parallel to the slope. It is clearly appreciated from this situation why the inner wedge is defined in terms of the rod radius.
- (4) is a rod whose orientation is parallel to the y-axis, and placed in the corner of the wedge.
- (5) is a rod whose orientation is parallel to the x-axis, and placed in the peak of the wedge.

Provided that all the hard bounds are properly defined, a MCM is performed. It was chosen to scale the wedge towards its barycenter, but alternatives are possible. One of the main issues with this modification was answering the question of *which is the most isotropic way of reducing the area a triangle*. This is very determinant, because particle position scaling will be defined with respect to this point. Another option was taking, for instance, the incircle of the triangle, which is the largest circle that will fit inside the triangle. Each side of the triangle is a tangent to this circle, and thus the centroid position scaling will differ with respect to the one performed.

3.3.2 *Simulation results. Scan in angle*

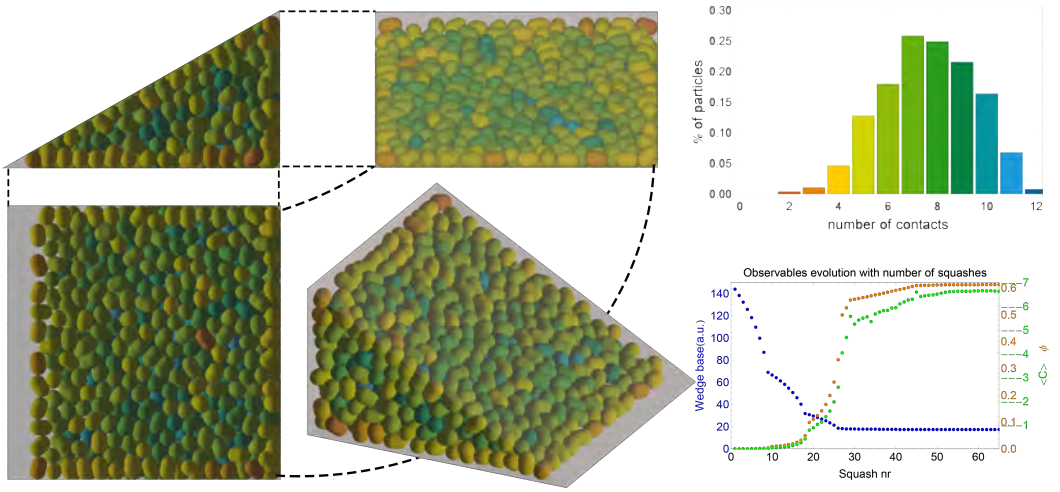

Figure 3.10: Right: Different perspectives of the final configuration of a Mechanical Contraction Method for 1000 rods with $\Lambda = 1.5$ within a wedge of angle $\frac{4}{25}\pi$ and aspect $\gamma = 1$, the particle position scaling performed with respect to barycentric coordinates. Left: final contact number distribution (top) and observables evolution with number of squashes of the wedge (bottom). Final values are $\phi = 0.61$, $\langle C \rangle = 6.64$ and $S = 0.04$. The color code for the contacts proves that actually particles touching the boundaries have clearly less contacts than the ones in the bulk of the wedge.

Already from Figure 3.10, a very general and expected result of how the algorithm is defined can be established: the hard boundary condition dramatically lowers the packing fraction and the contact number of the final configuration, whereas the nematic order parameters increases a little bit due to induced particle alignment in the wedge corner. Concerning how the scaling of the wedge hard

boundary is performed, it can be actually appreciated how the shape of the observables evolution is actually the same as for the particles in a box with periodic boundary conditions (Figure 2.2 in Section 2.1). As observed for the cylinder, geometrically induced alignment due to the wedge is also clearly present, overall in the peak of the wedge.

A first guess concerning the influence of the wedge angle θ could be that the highest packing fraction is obtained for angles close to $\pi/4$: for this angle the shape will be exactly just half of a cube. This is dismissed when one notices that actually the sharper the wedge, the more geometric rearrangement near the peak is produced. Being this clear for spheres, it may be considered the ways in which a rod can actually align with the corner of the wedge. The top view in Figure 3.10 shows how actually a rod can align parallel to two possible axes, either in the direction of the bases of the wedge (x) or perpendicular to it (z). Moreover, Figure 3.11 shows that whereas for sharp wedges rods align in the corner with either the x or the z-axis, for more open wedges alignment with actual slope is quite present. For spheres, the effect of the wedge is strong enough to even induce frustrated hexagonal sphere structures near the hard boundaries. The locally ordered arrangements of particles are actually obtained during well-controlled experiments [69, 86]. As far as MCM is a purely geometric method, the importance of the particle and container shape is clearly exhibited in these simulations.

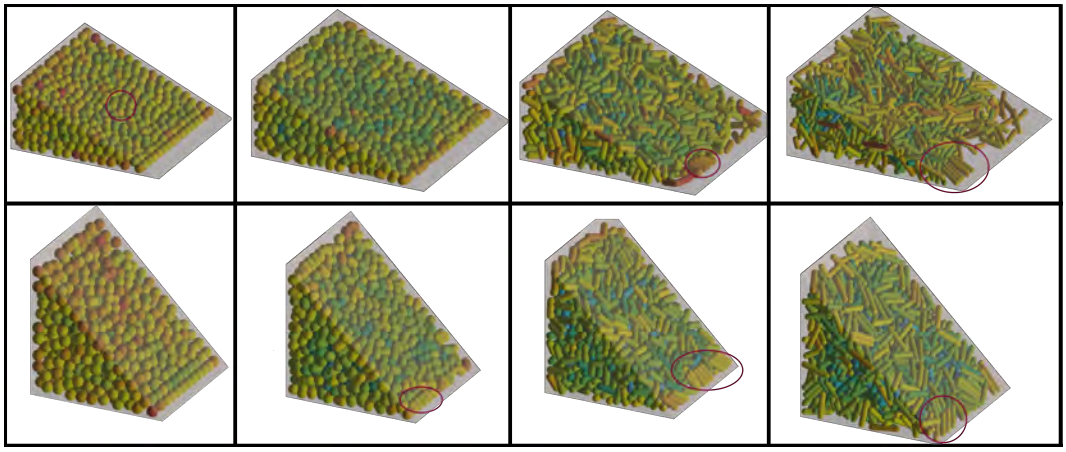

Figure 3.11: Final random configuration of 1000 hard rods inside a wedge of angles $\theta = 0.13\pi$ (top) and $\theta = \frac{1}{4}\pi$ (bottom) with increasing aspect ratio (from left to right): $\Lambda = 1, \Lambda = 1.5, \Lambda = 3$ and $\Lambda = 5$. Circles in red represent clearly geometrically arranged particles.

The final configurations exhibit a strong dependence in the initial random configuration, which is reflected in the big error bars of the final results, and thus no solid conclusions can be actually obtained. These big error bars could also be justified in terms of the possible local arrangements of particles: due to how the overlaps are removal, it can be expected that the possible local configurations we find actually vary depending on the particular case. The error bar could actually imply that the squash of the wedge is indeed so random that no possible conclusion, in the MCM framework, is possible. A bigger number of particles in the system and a bigger number of tries to remove the overlap would produce better results as well.

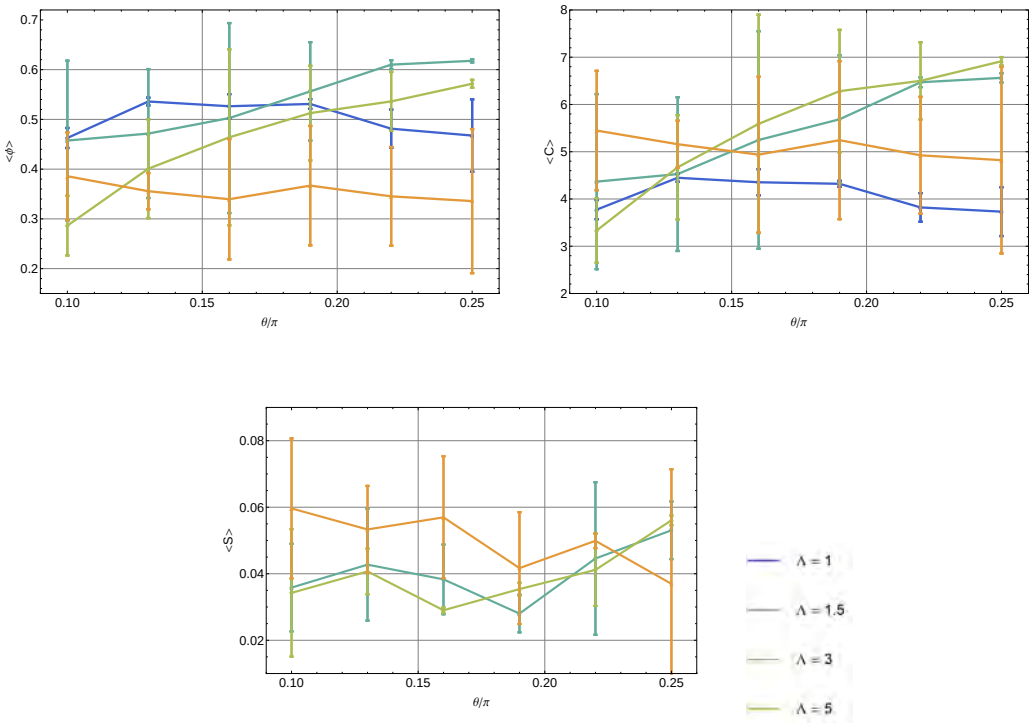

Figure 3.12: Final mean observables averaged over three runs of 1000 hard rods of different aspect ratios undergoing a Mechanical Contraction Method as a function of the π fraction of the angle θ of the hard wedge considered.

It is expected to find a symmetric shape on the dependence of the final observables around $\pi/4$ (as far as a wedge with angle θ should be equivalent to one with angle $\pi/2 - \theta$). Here it has been chosen to study values of $\theta < \frac{\pi}{4}$. Within the

algorithm modifications, only the slope contact detection was removed by means of a virtual rod, and this step was performed after the regular push back with the other planes. A proper definition of the wedge would require to define virtual rod contact detection with all planes, and perform all overlaps removal in the same step of the program. Furthermore, it is quite clear that the simulations within a wedge would require a higher number of initial random configurations, in order to get a proper averaged final value, and also simulations with a saturating number of trials to remove overlap should be carried out. Further studies on the wedge hard boundary should include as well the influence of the wedge aspect ratio.

3.4 CONCLUSION AND OUTLOOK

A general method to generalize the Mechanical Contraction Method to any hard boundary condition has been developed: the virtual rod method. The final configurations in both a hard wedge and a hard cylinder do not present either particle-particle or particle-boundary overlap. The long time that simulations take are the have been a limiting factor in the interpretation of the results.

For the cylinder, the final configurations resemble experimental results, and the dependence of the main observables keep the same dependence with the aspect ratio as in periodic boundary conditions. In the case of spheres, the limit of geometric self-organization happens only by means of geometry at very low boundary radii (about 2 to 3 times the radius of the particle). It shows a very interesting result: it constitutes a check that the effect of the hard boundary is already strong enough to induce only by geometrical means an ordered structure. Starting from this initial configuration of spheres in confinement, further studies in the dynamics of such system could be done.

Hard walls induce more differences in the final random configuration for rods than for spheres due to the combined effect of the curvature of the hard walls and the anisotropy of the particles. As rough estimation for the value from which this effect remains constant is $D_{\mathrm{Cyl}} \approx 5\Lambda$. Future research could provide insight in which kind of local particle arrangements are present in this region.

For the wedge, a proper analysis of the peak can actually provide information about the relevance of the boundary geometry in colloidal crystallization. Yet not a proper parameter dependence scan could be done, a case-by-case study actually shows that geometric rearrangement is clearly exhibited due to hard boundaries. As happened with the hard cylindrical container, the combined effect of the geom-

etry of the boundaries and the particle anisotropy play a key role in how do they achieve order.

The results presented in this chapter prove that the hard boundary description is suitable for spherocylinders and spheres. Studying the geometrical self-arrangement for low cylinder diameters for shapes that slightly deviate from spheres could provide deviations from the zig-zag and helical structures, and even shown new geometric ensembles not studied yet. For instance, a detailed studied of rods which deviate slightly from spheres could provide a sort of helical rotator structure. Recently, geometrical rearrangement of colloidal superballs have been performed ([84]), and thus simulating these particles inside a periodic cylinder via MCM could provide some idea about the geometries expected for the final configurations.

As done for the cylinder, a way of isolating the effect of the wedge would be, in this case, to make the wedge periodic in depth, and use the virtual rod method with all the planes would ensure a smoother approach to the final configuration. The mean issue here is indeed how the MCM is defined. The fact that the simulation stops when any particle overlap removal is not possible limits the ways in which the wedge squash can be performed. Indeed, if we consider only squash the X plane, very soon in the simulation we may find that particles in the wedge peak can not remove the overlap among them, whereas particles far from the slope will be in a diluted state.

Not only for different particle shape, but also for different containers the method of the virtual particle can be in principle applicable: by placing a virtual particle in the proper position, overlap with a hard boundary can always be removed. The main ideas presented in this chapter can be thus expanded to any container shape, allowing the study of the MCM in arbitrary hard boundaries.

As happened in periodic boundary conditions Chapter 2, the formulas presented in this chapter are general. The possible algorithm modifications described in the conclusion of Chapter 2 are then applicable also in hard boundaries.

4 RANDOM PACKING OF SUPERQUADRICS VIA MECHANICAL CONTRACTION

Beyond the interesting behavior of a collection of hard spheres, studying other shapes provides insight in the influence of particle geometry on the final configuration of a systems of hard bodies. It is known that non-spherical hard particles exhibit a more complex phase behavior, shown by the existence of anisotropic phases such as smectic, nematic, columnar and cubatic liquid crystal. Studying random packing configurations of a general particle shape is then a fundamental task, as these configurations do not belong to the phase diagram of hard particles.

The Mechanical Contraction Method has been previously applied to rods, ellipsoids and cut spheres [58, 63]. However, the algorithm for a general particle shape was not yet developed. Here the most general possible schema for an analytical surface is presented, together with novel results of MCM applied to superballs. The contact detection algorithm here developed finds applicability in any other computer simulation.

4.1 INTRODUCTION

The present chapter deals with random packing of superquadric particle shapes in periodic boundary conditions using the Mechanical Contraction Method. Superquadrics are, in essence, a generalization of ellipsoids. As for any other surface, at very low densities particle shape does not play a role, and excluded volume effects are exhibited as packing fraction increases. The features arising from the random packing of superballs simulated on the next section require to understand why this shape is important and the applicability that such particles found in research.

4.1.1 *Superquadrics, Superellipsoids and Superballs*

Although widely studied, there exists some confusion in the terminology concerning superquadrics and superellipsoids. We adhere to the following definition of the most general equation for superquadrics:

$$F(x,y,z) = \left(\frac{x}{a_x}\right)^{\varepsilon_x} + \left(\frac{y}{a_y}\right)^{\varepsilon_y} + \left(\frac{z}{a_z}\right)^{\varepsilon_z} - 1 \leq 0 \tag{4.1}$$

Here, a_k are the *surface parameters* and represent the length of the particle's semi axes; and ε_k are called *surface implicit parameters* and they determine the asphericity of the particle. $F(x,y,z)$ is the *inside-outside function*: all points that satisfy $F(x,y,z) \leq 1$ are inside ($<$) or exactly on the surface ($=$) of the superquadric. More well-known shapes are obtained when we consider the case in which $\varepsilon_x = \varepsilon_y = \varepsilon_z = 2\gamma$, and furthermore by taking $a_x = a_y = a_z = 1$. The last case, known as *superballs* [9–11, 19, 57], are deviations from the sphere equation ($\gamma = 2$), and will be the ones for which the simulations are performed. Equation 4.2 presents the particular equation for superballs.

$$\left|\frac{x}{a_1}\right|^{2\gamma} + \left|\frac{y}{a_2}\right|^{2\gamma} + \left|\frac{z}{a_3}\right|^{2\gamma} = 1 \tag{4.2}$$

Now γ, called *deformation parameter*, is any positive real number that determines the curvature of the particle (how round or sharp it is). For superballs:

- $\gamma < 1$ provides a concave shape ranging from a cross ($\gamma = 0$) to the convex octahedron ($\gamma = 0.5$) and deformations from the octahedron, rounding its corners.
- $\gamma = 1$ retakes the equation of the sphere.
- $\gamma > 1$: a cube with rounded edges and corners. In the infinite case, we will recover the cube.

A completely different family of shapes but more widely used are the superellipsoids [87], whose most general equation is given by:

$$F(x,y,z) = \left(\left(\frac{x}{a_1}\right)^{\frac{2}{\gamma_2}} + \left(\frac{y}{a_2}\right)^{\frac{2}{\gamma_2}}\right)^{\frac{\gamma_2}{\gamma_1}} + \left(\frac{z}{a_3}\right)^{\frac{2}{\gamma_1}} \tag{4.3}$$

When the three implicit parameters $\varepsilon_{(x,y,z)}$ for the superquadric equation are all equal, and the two implicit parameters $\gamma_{(1,2)}$ are also the same, the family of surfaces defined by the superquadric equation is equivalent to the one of the superellipsoids. It may be remarked that this is not the general case, and neither

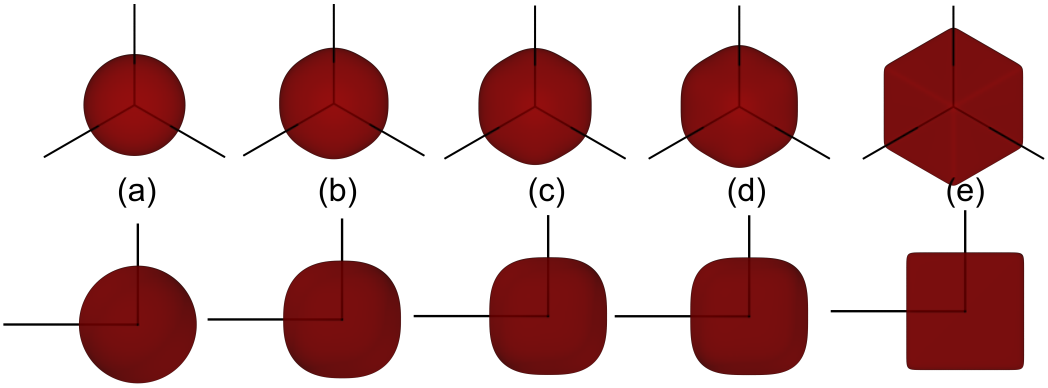

Figure 4.1: Superballs for certain deformation parameter, from a general perspective and from top view. (a) $\gamma = 1$, (b) $\gamma = \frac{5}{4}$, (c) $\gamma = \frac{10}{7}$, (d) $\gamma = \frac{5}{3}$, and (e) $\gamma \approx \infty$.

.

family is contained in each other. Superballs and supercuboids are just a very specific case which belong to both families. Appendix A contains some geometrical properties of the shapes here studied.

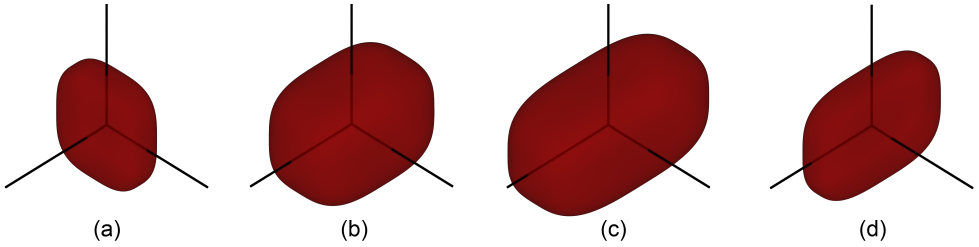

Figure 4.2: Superquadrics with $\gamma = \frac{5}{3}$ with their three principal non-equivalent axes. (a) $a_x = 0.5a_y, a_z = a_y$, (b) $a_x = 1.5a_y, a_z = a_y$, (c) $a_x = 2a_y, a_z = a_y$, and (d) $a_x = 3a_z, a_y = 2a_z$. As the implicit indexes are all equal, this particles are both superellipsoids and superquadrics: supercuboids.

The case studied in the present document is $\gamma > 1$. Non-equally axed superquadrics as in the second line of Equation 4.2 may be compared with cuboids with round edges (Figure 4.2), and therefore they will be named in as *supercuboids*.

4.1.2 *Packings of Superballs*

Yet not within the framework of the Mechanical Contraction Method, research can be found concerning packings of superballs. The present section will go through some of the experiments and simulations of this particular shape.

4.1.2.1 *Colloidal superballs*

Increasing the parameter γ for superball induces a sharpening in the particle edges and corners, producing for instance an increasing excluded volume. This interesting property have lead to the study of the phase diagrams of superballs[10, 11]. Upon increasing the packing density, we can appreciate for any deviation from the sphere to more cubic shapes three different phases: fluid, plastic FCC and deformed C_1 (Figure 4.3, left). The cubatic liquid crystal phase is characterized by ordering of the particles in three mutually perpendicular directions while they retain translational mobility [10], and it is of special interest because it may lead to novel optical, rheological and transport properties.

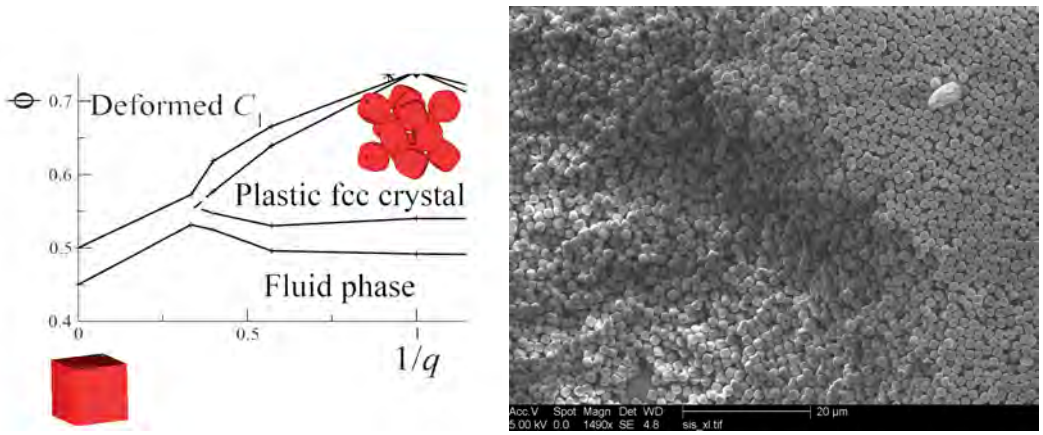

Figure 4.3: Left: Phase diagram for hard superballs. Image taken from [11]. Right: Scanning Electron Microscopy (SEM) image of colloidal superballs composed of hematite. The colloids have been assembled / packed by force sedimentation. Order is clearly present in the first top/bottom layers, whereas more a random packing is found where particles are not in contact with the boundaries.

Since amorphous silica spheres are a classic topic in the field of colloid and materials science, other silica shapes in the form of superballs have been also studied [19, 88]. Superballs can crystallize into simple-cubic arrays, and sediment into macroscopic mosaic tilings (Figure 4.3, right) [89, 90]. This can lead to novel

photonic crystals, where the different lengths involved are used. Furthermore, synthesis of colloidal supercuboids may lead to a new state of liquid crystal, where up to three different optical axes could be exploited. Colloidal cuboids have been already applied in the degradation of organic dyes [91]. Hollow silica cubes are of potential interest for designing ceramic membranes that also exploit functionality stored in these cubes, for example a catalyst in the form of iron-oxide particles. Iron-oxide would provide the cubes with a magnetic moment, inducing self-assembly of cubes.

4.1.2.2 *Characterization of Superball Packings*

The state of a system constituted by superballs is determined by measures of its order (*order parameters*) and particles' position distribution (*radial distribution function*). The *radial distribution function*, $g(r)$, describes how density varies as a function of distance from a reference particle: it is the measure of the probability of finding a particle at a distance r away from a given reference particle, relative to that of an ideal gas. How this function behaves is well known for a hard sphere system, being this the reference system. When $r \to \infty$ and when the system is very diluted, this function tends to unity.

For measuring the orientational order, two different parameters are normally taken into account: the *nematic* and the *cubatic* order parameters, $S_{2,j}$ and S_4, respectively. Both parameters have been calculated as specified by Torquato [10]. The nematic order parameter for a particular set of axes j is defined as in Equation 4.4. The formula for S_2 has been the one considered also for rods, but it is here explicitly present.

$$S_{2,j} = max_{\boldsymbol{n}_j} \frac{1}{N} \sum_{i=1}^{N} \left(\frac{3}{2} | \, \boldsymbol{u_{ij}} \cdot \boldsymbol{n_j} \, |^2 - \frac{1}{2} \right) \tag{4.4}$$

Where N is the number of of particles, $\boldsymbol{u}_{ij}$ is a set of particle axes, and $\boldsymbol{n}_j$ is the director for direction j. This value is then obtained solving an eigenvalue problem.

The cubatic order parameter S_4 is a more appropriate scalar metric for ordering in superballs as far as it takes into account the particle axes. In this case, we look for its maximum value among a set of trial vectors $\boldsymbol{n}$. The set of trial vectors was chosen to be the conjunct of the three principal axes of all particles in the system. It can be easily checked that $S_4 = 1$ when any of the three principal particle axis is in the same direction for all particles.

$$S_4 = max_{\boldsymbol{n}} \frac{1}{14N} \sum_{i=1}^{N} \left(\sum_{j=1}^{3} (35 \mid \boldsymbol{u_{ij}} \cdot \boldsymbol{n} \mid^4 - 30 \mid \boldsymbol{u_{ij}} \cdot \boldsymbol{n} \mid^2 + 3) \right) \tag{4.5}$$

4.2 MCM FOR SUPERQUADRICS

The present section presents the formalism underlying the MCM for any superquadric shape (which includes all convex shapes) and general systems constituted by different particles. As happened in previous chapters (Chapter 2 and Chapter 3), the explanation presented is general, but the simulations performed only deal with mono-modal systems of superballs.

4.2.1 *Energy constraint and overlap removal for general convex shape.*

In order to use the MCM with superquadrics, a generalization of the algorithm as provided in Chapter 2 is needed. The initial configuration and scaling of the system periodic boundaries will be the same. However, it must be taken into consideration how the overlap is removed between two general convex bodies, according to the general energy constraint defined. A proper contact detection (explained in detail in the next subsection) that provides the minimum particle-particle distance or the overlapping distance is necessary. Moreover, such contact detection must provide a proper definition of the normals to the surface at the contact points.

The velocity vector $\boldsymbol{a}_i$ defined in Chapter 2 is defined again. Considering the kinetic energy of a particle i that translates and rotates with rotations defined around its main axes, the most general energy constraint reads as:

$$\begin{array}{lll} E_{k,i} & = & \frac{1}{2} m_i \boldsymbol{v}_i \cdot \boldsymbol{v}_i + \frac{1}{2} \boldsymbol{\omega}_i \boldsymbol{I}_{i_c} \boldsymbol{\omega}_i \\ \text{In general:} & m_i \neq m_j \forall (i,j) & \wedge I_{i,x'} \neq I_{i,y'} \neq I_{i,z'} \\ 1 & = & m_i \boldsymbol{a}_i^{\mathrm{L}} \cdot \boldsymbol{a}_i^{\mathrm{L}} + \boldsymbol{a}_i^{\mathrm{R}} \cdot \hat{I}_{i,S} \cdot \boldsymbol{a}_i^{\mathrm{R}} \end{array} \tag{4.6}$$

Again, the $6D$ vector $\boldsymbol{a}_i$ simply represents the translational and rotational components of the velocity, according with the numerical choice for the overlap removal: $2E_{k,i} = m_i \forall ! i$. As discussed before, what this choice implies is that simply larger/denser particles move less than smaller/less dense ones, according to the common physical picture. Any other choice would just imply a constant factor in the equations present.

$$\boldsymbol{a}_i \;=\; \left(\boldsymbol{a}_i^{\mathrm{L}}, \boldsymbol{a}_i^{\mathrm{R}}\right) \;=\; \left(a_i^{\mathrm{L}_x}, a_i^{\mathrm{L}_y}, a_i^{\mathrm{L}_z}, a_i^{\mathrm{R}_x}, a_i^{\mathrm{R}_y}, a_i^{\mathrm{R}_z}\right) \tag{4.7}$$

With the previous magnitudes considered and provided a good surface characterization, the dot product of the total scaled components of the velocity of particle

i in the contact point with the normal to each surface at this point will give (up to first order) the rate at which the overlap of particle i with particle j changes. Further details concerning dynamics of rigid bodies can be found in the book *Rigid Body Dynamics Algorithms* [92].

$$\frac{\partial|\boldsymbol{\delta}_{ij}|}{\partial t} = (\boldsymbol{a}_{i,\mathrm{L}} + \boldsymbol{a}_{i,\mathrm{R}} \times \boldsymbol{r}_{Cij}) \cdot \hat{\boldsymbol{n}}_{Cij} \tag{4.8}$$

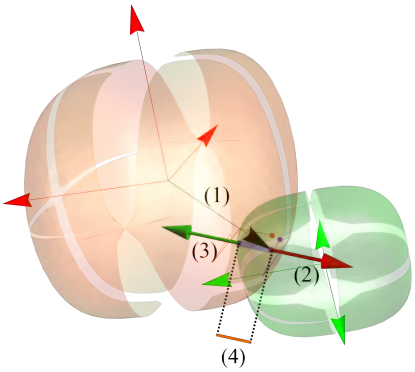

Figure 4.4

Figure 4.4 presents the parameters involved in the contact detection and overlap removal for superquadrics are presented. (1) is the vector connecting the center of masses of particle i with the contact point with particle j on its surface: $\boldsymbol{r}_{Cij}$; (2) and (3) are the normals to to surfaces i and j at the contact points: $\hat{n}_{Cji}$ and $\hat{n}_{Cij}$; and (4) is the overlap distance $\boldsymbol{\delta_{ij}}$, which moduli determinate the overlap removal rate.

When particle i is in contact with a number of particles C, the main features defined for rods remain in the formulation. Then, factor that accounts for the most overlapping contact δ_{ij}, and a overlap removal rate β are present such that the total overlap removal can be expressed as:

$$s_i = \sum_{j=1}^{C} \beta|\boldsymbol{\delta}_{ij}| \frac{\partial|\boldsymbol{\delta}_{ij}|}{\partial t} \tag{4.9}$$

Provided the direction of overlap removal from the linear and rotational velocity components, by minimizing via Lagrange constraint optimization Equation 4.9 subject to Equation 4.6 the the relative importance of each velocity component is obtained. As happened for rods, the solution of the exact Lagrangian is again quite extensive and can be found in Appendix B. Notice that the overlap removal is finally also determined by the overlap removal rate β and the bias factor δ_{ij} when several overlaps are present.

$$\begin{aligned} \boldsymbol{a}_i^{\mathrm{L}} &= \tfrac{1}{\sqrt{m_i}} \textstyle\sum_{j=1}^{C} \delta_{ij} \hat{n}_{Cij} \\ \boldsymbol{a}_i^{\mathrm{R}} &= \tfrac{1}{\boldsymbol{\epsilon}\sqrt{m_i}} \textstyle\sum_{j=1}^{C} \delta_{ij} \left(\boldsymbol{r}_{Cij} \times \hat{n}_{Cij}\right), \text{ with } \boldsymbol{\epsilon} = \tfrac{1}{m_i}(I_{i,x'}, I_{i,y'}, I_{i,z'}) \end{aligned} \tag{4.10}$$

As expected for what was discussed already in Chapter 2, setting the density of all particles in the system to 1 reduces the dimensions of mass and volume to the same, thus connecting the speed at which a particle removes overlap with its dimension: the smaller the particle the faster it removes the overlap. Notice that the the case in which only translational overlap removal are considered reduces to the case of spheres. As far as what matters is the relative importance of each component of $\boldsymbol{a}$ for mono-modal systems the pre-factor $\frac{1}{\sqrt{m_i}}$ is simply not playing a role (is taken into account in β anyway). The center of mass and the rotation of a particle when overlap is tried to be removed depends on their previous values and change according to the velocities optimized.

$$\begin{aligned} \boldsymbol{x}_{\mathrm{cm},i}^{m+1} &= \boldsymbol{x}_{\mathrm{cm},i}^{m} + \mathrm{d}t\boldsymbol{a}_{i,\mathrm{linear}} \\ \hat{r}_i^{m+1} &= \mathrm{d}t\hat{r}_i^{m} \cdot \boldsymbol{a}_{i,\mathrm{rotational}} \end{aligned} \tag{4.11}$$

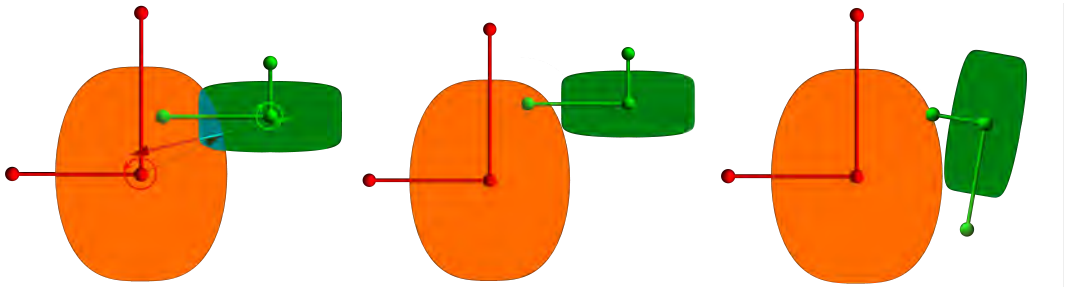

Figure 4.5: A minimalist visualization of the overlap removal for two general convex shapes (in $2D$). Left: original overlap situation, with the overlap distance in light blue. Center: overlap between particles removed only by translational movement. Right: overlap removed only by rotational components. The optimal overlap removal would be a combination of the two movements.

4.2.2 *Contact Detection Algorithm between Superquadrics*

A contact detection algorithm is need in order to perform any kind of hard particle simulation. For spheres, the contact detection only requires the radii of the particles involved. The symmetry of rods is used for building a fast contact detection algorithm [74]. Looking at the contact detection of superquadrics is a challenging task, and will be the most computationally expensive part of the code: jacobians of the surface are needed, and its calculation is not trivial. For efficiency, the number of times that the actual contact detection algorithm is called must be minimized.

The first check towards particle-particle contact detection evokes a simpler shape that envelopes it. When particles have a chance of being in contact, an iterative method needs to be called. A good starting estimate is essential to ensure the stability of such method. A study of which pair of points provide the faster convergence is required before incorporating the contact detection algorithm in a more evolved program: a very slow convergence will imply a too slow algorithm.

4.2.2.1 *Enveloping sphere radii r_{env}*

The *Separating Axes Test* (SAT) provides the starting points by evaluating the possible crosses of the axes that define the box that encloses a given particle [93]. However, superquadrics can be also approximated by the smallest sphere that contains its shape. Thus, when the enveloping spheres of two general superquadrics intersect, the contact detection algorithm is called. The calculation of this enveloping sphere radius was performed using a general Lagrange Constraint optimization method: minimize $d = x^2 + y^2 + z^2$ (square distance to the center) subject to $F(x, y, z) = 1$ (point is on particle surface). Details in this calculation and the possible analytical solutions are presented in Appendix E. The assumptions beyond this idea were checked by performing the same simulation with a proper (minimal) and an overestimated first contact distance, and the results provided were the same. Figure 4.6 summarizes the main features of this enveloping sphere.

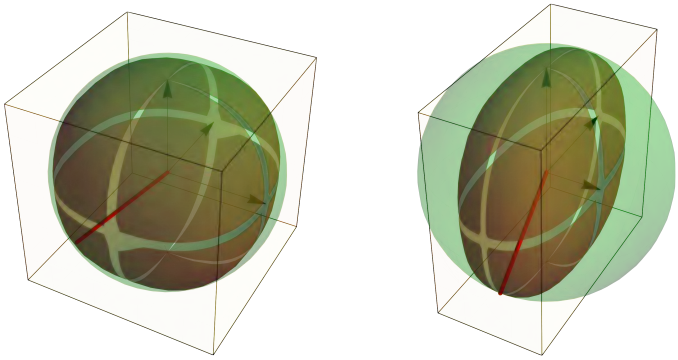

Figure 4.6: From inner shape to outer shape: supercuboids (brown) with its three principal axes (black) and the solution provided by the Lagrange constraint optimization (red). The sphere enveloping this shape (green) defines the cut-off distance. Outer box: axis that may be evaluated using Separating Axes Test. Both superquadrics have an implicit surface parameter $\gamma = \frac{5}{3}$. Left:$a_x = a_y = a_z$, right: $a_y = a_z = 2a_x$.

4.2.2.2 *First points estimate.*

When two particles are within the possible contact distance, a point on each superquadric surface is calculated considering that this point lies on the line connecting the center of the two bodies. This first point has been calculated as specified by Portal [93], and consists of solving a nonlinear equation (Equation 4.12) for a certain χ in the local reference frame of each particle:

$$\begin{aligned}(R_1)^{\varepsilon_x} + (R_2)^{\varepsilon_y} + (R_3)^{\varepsilon_z} - 1 = 0 \\ R_i = \frac{\chi}{a_i}\hat{\boldsymbol{T}}^T(\boldsymbol{p}_{\boldsymbol{x}_B} - \boldsymbol{p}_{\boldsymbol{x}_A})\end{aligned} \tag{4.12}$$

Here, $\boldsymbol{p}_{\boldsymbol{x}_k}$ is the position of the center of particle k and $\hat{\boldsymbol{T}}$ is the transformation matrix that describes its orientation. With this procedure, we obtain the values χ_A and χ_B, and thus the initial guess in the global reference frame will be given as $\boldsymbol{x}_{A,G} = \boldsymbol{p}_{\boldsymbol{x}_A} + \chi_A(\boldsymbol{p}_{\boldsymbol{x}_B} - \boldsymbol{p}_{\boldsymbol{x}_A})$ and $\boldsymbol{x}_{B,G} = \boldsymbol{p}_{\boldsymbol{x}_B} - \chi_B(\boldsymbol{p}_{\boldsymbol{x}_B} - \boldsymbol{p}_{\boldsymbol{x}_A})$.

4.2.2.3 *Iterative Solution*

Using this first point estimate, a set of equations is solved using the Newton-Rhapson method in order to get the closest point between surfaces. This was implemented as specified by the contact detection algorithm developed by Lopes [94]. It essentially consists in solving a system of non-linear equations that contains the set of geometrical constraints imposed, thus exploiting the numerical behavior with analytical Jacobians. Care must be taken here: the jacobian for very weird particles or orientations could be ill-defined, carrying a non proper final solution.

Let $\boldsymbol{q}^G$ be the 6 dimensional set of values that define the points P and Q on surfaces A and B in global coordinates. Let $\boldsymbol{d}_{PQ}$ be the distance between these points, $\boldsymbol{\Phi}^G(\boldsymbol{q}^G) = \boldsymbol{0}$ the set of constraints to minimize and $\boldsymbol{\Phi}^G_q$ the Jacobian matrix of the geometric constraints. The geometrical idea in this set of constraints is as follows:

1. The final solution respects the definition of the normal vector, thus having two mutually perpendicular vectors: the tangent ($\boldsymbol{t}_{OP}$) and the binormal vector ($\boldsymbol{b}_{OP}$).

2. The normals on opposite surfaces are anti-parallel. This condition will be expressed towards the binormal ($\boldsymbol{b}_{OQ}$) and the tangent ($\boldsymbol{t}_{OQ}$) vectors.

3. Points are on particles' surfaces $F_{\mathrm{A}}(x,y,z) = 0$ and $F_{\mathrm{B}}(x,y,z) = 0$ (surfaces as given by Equation 4.1).

The Newton-Rhapson solution will iterate until the difference between q_{k+1}^G and q_k^G is smaller than a certain tolerance. A proper convergence is obtained usually when the initial guess is a good one. The iterative method and the set are shown in Equation 4.13 in their mathematical form, and Figure 4.7 shows graphically how the contact detection behaves.

$$
\begin{aligned}
q_{k+1}^G &= q_k^G - (\mathbf{\Phi}^G(q_k^G))^{-1}\mathbf{\Phi}^G(q_k^G) \\
\mathbf{\Phi}^{G,6}(q^G) = \mathbf{0} \Leftrightarrow &\begin{pmatrix} n_{OP}^T \cdot t_{OQ} \\ n_{OP}^T \cdot b_{OQ} \\ d_{PQ}^T \cdot t_{OQ} \\ d_{PQ}^T \cdot b_{OQ} \\ F_A \\ F_B \end{pmatrix} = \mathbf{0}
\end{aligned}
\tag{4.13}
$$

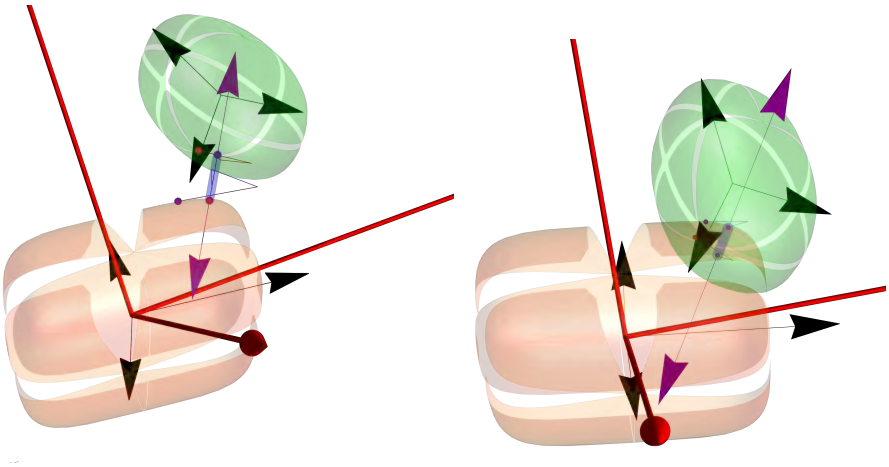

Figure 4.7: Two snapshots of the contact detection algorithm for a non-contact (left) and a contact (right) situation. Red arrows: global reference frame. Black arrows: local reference frames of each particle (principal axes). Purple arrows: normals to surface of the final solution. Blue tube: final optimization result. The iterations from the first point estimation are also shown. None of the three axis of the particles are the same, and the deformation parameter has been chosen as $\gamma = \frac{5}{3}$.

4.2.2.4 *Towards the most stable solution*

A proper solution for an iteratively solved optimization requires good first point estimation, so that stationary points (local minima) and divergences are avoided.

Thus, when the solution provided by the points on the surfaces defined before did not converge in 500 iterations several alternatives were considered. The main particle axes with minimum distance were calculated. The points on each surface crossing those axis were taken as the first point estimations (considering a segment-segment intersection as defined for rods [74]). This improved the iterative solution for certain orientations. If even this second optimization did not converge, then the original estimation given by Lopes [94] in the contact detection was used. However, it must be remarked that this first points estimate did not lie on particle surface, but near it.

Within each one of this set of possible starting point estimations, two possible alternatives were considered concerning the steps of the Newton-Rapshon iterative procedure. There is not in principle a reason for the distance between two iterative solutions to be bounded. However, this can lead to very big steps between two steps of the solution. When the regular iterations did not converge in the user-defined number of iterations, a step-size controlled iteration was performed. This prevented divergences in the different steps towards the solution. However, oscillatory solutions could be still present.

When none any of these combinations converged, the minimum distance of the considered initial first point estimate was taken as a final solution. It can be remarked that this does not happen for superballs in a significant percentage of cases: initial first points estimation performed is already a optimization by itself. Moreover, for superballs with low deformation parameter the Portal first point estimate is very close to the final solution.

Another possibility considered was generating a very small random particle rotation upon arrival to a non convergent solution, such that the Jacobians could not be ill defined with the new particle orientations. Yet this last possibility was investigated, it was not incorporated in the program used for generating the results later presented.

4.2.2.5 *Contact criteria.*

Provided a final solution on each one of the particles surfaces, and knowing the normals to the superquadrics at each point analytically, a contact is define in terms of the normal to the considered optimized solution on each particle surface. Two particles are defined to be in contact when they satisfy:

$$\boldsymbol{n}_{\mathrm{OP}} \cdot \boldsymbol{d}_{\mathrm{OP}} < \varepsilon \tag{4.14}$$

where ε is a small factor ($\varepsilon \leq -10^{-7}$) used to alleviate numerical problems (see next section).

4.3 PARAMETER DEPENDENCE FOR SUPERBALLS

Has happened before for rods, the MCM requires a set of parameters concerning contact detection, size of neighbour list and rate of overlap per step. Due to the change in the contact detection and overlap removal explained in this chapter with respect to the previous cases (Chapter 2 and Chapter 3), it is worth to study the parameter dependence for superballs.

Strictly, the factor ε in Equation 4.14 must be zero. However, values of $\varepsilon \in \{-10^{-7} - 10^{-10}\}$ were tested to keep the idea of allowing a small overlap between particles, as done for spherocylinders. Moreover, the contact detection is defined again as a positive deviation from the contact detection test, $\varepsilon \approx 0.001$. This is equivalent to the inner and outer shells defined for rods (Chapter 2). The values for the small overlap and contact detection were set as the ones that retrieve the expected contact number for spheres, provided that the other observables present in the random packings generated by applying the different considerations, were equivalent to the ones previously obtained.

An important factor to take into account is the computational cost of the contact detection algorithm. As it can be guessed, these simulations take more time as the contact detection algorithm requires many heavy computations. The limiting factor implemented by the user is the number of tries to remove particle overlaps, and knowing that the higher its value the higher the final packing fraction, it was set in the calculations performed to 10^5 for systems with 750 particles. This was done in the basis that calculation time scales with N^2 and this number of particles provides a good statistics.

Although the overlap removal rate factor was kept, how particle rotations are removed is modified in the general convex shape schema of the MCM. We observed that due to the relatively low number of tries to remove overlap, a sufficiently high overlap removal rate must be chosen ($\beta > 0.4$). For superballs with $\gamma = 5/4$ (Figure 4.8) a very different result is achieved in terms of β. On the bases of Figure 4.8, the simulations performed where carried out with $\beta = 0.5$.

For any set of parameters chosen, the average cubatic order parameter was always lower than 0.2, whereas the nematic order parameter was lower than 0.12 showing a slightly increasing final value with increasing β. It can be noticed here that a better choice of the trial axes in the calculation of S_4 is a big set of randomly oriented unit vectors. Also, analytical implementation of the S_4 factor is found, and should be taken into account for future improvements [95].

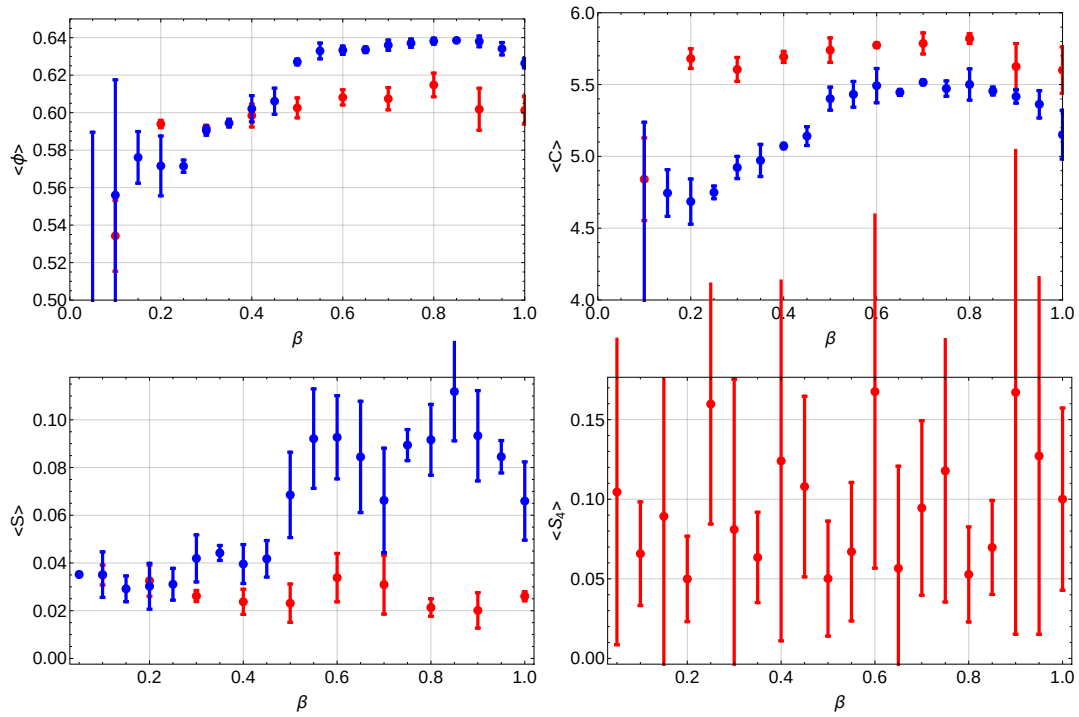

Figure 4.8: Final packing fraction ϕ (top,left), mean contact number $\langle C \rangle$ (top, right), nematic order parameter S_2 and cubatic order parameter S_4 as a function of the overlap removal rate β for spheres (blue) and small sphere deviation ($\gamma = 5/4$) (red) averaged over three different initial configuration of 750 hard superballs.

4.4 RESULTS FOR SUPERBALLS

Provided a good contact detection algorithm, how overlap between particles is removed and the best choice of intrinsic parameters to the method, the Mechanical Contraction Method for superquadrics can be applied. Due to the computational cost of this algorithm due to the complexity of the contact detection, we restricted

the simulations performed to superballs.

Two different random distribution of 750 non-overlapping superballs were set for different values of γ. In each one of these configurations, mechanical contraction was applied with the same set of intrinsic MCM parameters. For the ones related with the contact detection, the set that provided the closest final mean contact number obtained for spheres undergoing MCM was chosen ($\langle C \rangle = 5.84 \pm 0.04$).

4.4.1 *Pair distribution function reflects excluded volume effects.*

As the deformation parameter γ increases, a sharpening of the particle edges and corners takes place, inducing anisotropy of the superballs and an increase in its excluded volume. The analytical expression for the average excluded volume of two convex bodies is [96]:

$$V_{\text{exc}}^{(i,j)} = V_i + V_j + \frac{A_i R_{c,i} + A_j R_{c,j}}{4\pi} \tag{4.15}$$

where V_i is the volume of each convex particle, A_i is its surface area and $R_{c,i}$ is its total mean curvature: the average radius of the local surface curvature, integrated over the entire surface. It is worth mentioning that there is not an exact solution for the area of a superball. Furthermore, the main curvature of a superball has to be calculated providing both the normal and tangent vectors at each point [97], and later on integrated over its non analytical area.

This increase in the excluded volume as particle becomes more cubic is clear considering the excluded volume of a pair of cubes with length $L_i = 1$ and the one of the pair of spheres that contains them (with diameter $d_i = \sqrt{3}$). The shapes here discussed are shown in Figure 4.9 The excluded volume of two spheres is 4 times their volume ($V_{\text{exc}}^{\text{spheres}} = 4V_{\text{sphere}} = 2\pi\sqrt{3}$). By solving Equation 4.15 we can calculate the excluded volume for two cubes ($V_{\text{exc}}^{\text{cubes}} = 11$). The ratio between this two excluded volumes is almost 1 ($\frac{V_{\text{exc}}^{\text{spheres}}}{V_{\text{exc}}^{\text{cubes}}} = 0.99$).

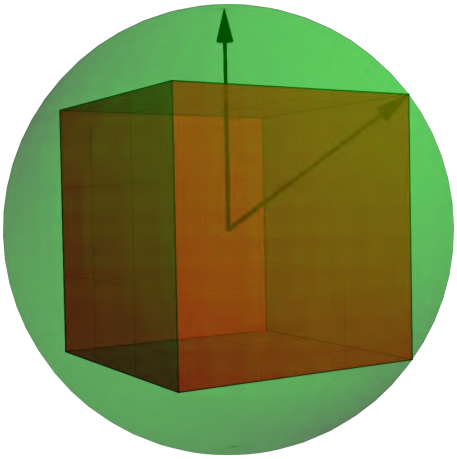

The sphere enveloping a cube used for comparing excluded volume of two particles. In essence, the excluded volume of two red cubes will be the one of two green spheres.

Figure 4.9

This implies that a cube excludes on average to another cube a volume almost equivalent to the volume of the sphere that envelops it. Having each enveloping sphere a volume 2.72 times bigger than each cube, the excluded volume for the two spheres is almost the same as for the two cubes. This makes sense in terms of the possible positions of the corners of the cube, that will always lay on the surface of the enveloping sphere. A geometrical first approximation for the excluded volume of two superballs will be then 4 times the volume of its enveloping sphere.

This increasing excluded volume with γ is clearly shown in the radial distribution functions, $g(r)$. In Figure 4.10 the value of the surface parameter is set to 0.5, so that for $\gamma = 1$ we have a sphere of diameter 1.0. For both a more common Monte Carlo simulation [98] or the final random state undergoing a Mechanical Contraction Method, the position of the first peak always lies between 1.0 and twice the radius of the enveloping sphere (which increases as expected with γ). This makes sense as far as the lowest distance between two superballs will be 1, but larger values are also possible. As an effect of the anisotropy of the particles, contact neighbours are not restricted to $r = 1$, which produces a lowering in the peaks as γ increases and a displacement of the peaks position to the right.

Regarding at Table 4.4.1, the relation between the position of the first peak of $g(r)$ and the radius of the enveloping sphere becomes more clear. The diameter of the enveloping sphere is always slightly higher than the position of the first peak, and it increases as particles become sharper. This indicates again the possibility of superballs to be closer due to their anisotropy. This is also connected with the faster convergence with γ for the volume of the superballs than for the volume of

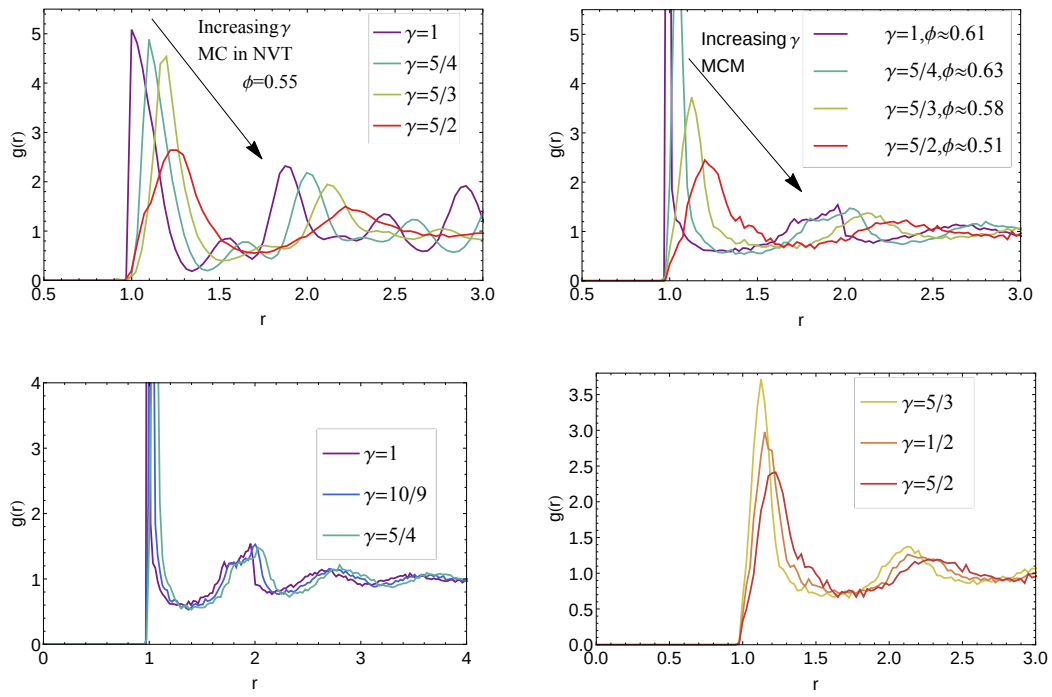

Figure 4.10: Top, left: averaged radial distribution function of a Monte Carlo simulation in the NVT ensemble for systems of 256 hard superballs with increasing γ. Top, right: final radial distribution function for different surface deformation parameters γ averaged over three runs of the final configuration of systems of hard 750 superballs. Bottom line as top left.

the corresponding enveloping sphere.

γ	V_p	$2 * r_{\text{env}}$	x_1^{app}	$V_{\text{exc}}^{\text{app}}$
1.0	$\pi/6$	1.00	1.00	$4\frac{\pi}{6}$
5/4	0.634	1.12	1.10	2.91
5/3	0.752	1.25	1.20	4.05
5/2	0.866	1.39	1.25	6.11

Table 4.1: Values involved in the enveloping sphere calculation and the approximate excluded volume for different deformation parameters.

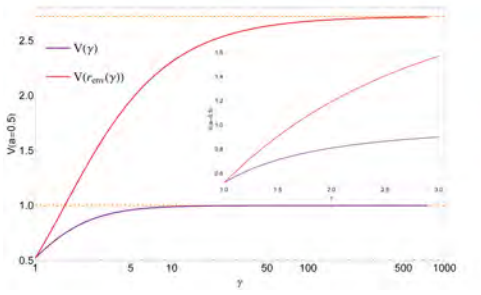

Figure 4.11: Volume of particle and the enveloping sphere approximation. Inset plot in logarithmic scale.

As it can be observed in Figure 4.10, for small deformation parameters γ the radial distribution function in a final random configuration is like the one for a

hard sphere system, whereas above a certain critical deformation it becomes more different. As it happens for small rods aspect ratio (Chapter 2), a small perturbation in particle shape produces a higher packing fraction due to a higher filling of the voids in the system. However, when particles become sharper (too cubic), the excluded volume effect dominates and the allowed maximum packing fraction decreases. This can provide an estimation of when a superball geometry is closer to the one of the sphere or closer to the one of the cube. For high enough deformation parameters the radial distribution function has a shape similar to the one of a sphere fluid. This is due not only to the lower final packing fraction, but also due to the lack of a local order in the final configuration achieved.

The calculation of the smallest enveloping sphere can be extended to superquadrics. The largest position from the particle center will cover upon all possible rotations this enveloping sphere (see Appendix E). However, a better first approximation of a general shape may be the smallest spheroid that envelopes it.

4.4.2 *Scan in deformation parameter γ*

As it happened for rods, for small deformations from the sphere an increase of the packing fraction is expected, as far as the corners are not sharp enough in this case to kinetically trap other superballs (to restrict dramatically other superballs positions). When corners and edges are sharp enough to limit other particle positions, the packing fraction decreases. Mechanical equilibrium is not ensure ever withing the MCM framework, and friction between particles is not considered. It has been shown that that frictionless random packings have just enough constraints to completely define the random state of spheres. But this does not hold for non-spherical packings [57].

However, particles arrive to situation in which their positions are fixed in the sense that any further increase in the packing fraction will induce an overlap. This does not imply that some cubes are not caged inside clusters of blocked particles (rattles). The effect of local particle reorganization is minimized, as far as a situation where cubes align their flat phases upon overlap removal is not favorable. The cubatic order parameter is always lower than 0.2, and does not show any pattern with increasing γ. The nematic order parameter S_2 reaches a maximum of 0.06 and does not present a correlation with γ either.

The behavior of S_4 is clearly different from the one in a Maximally Random Jammed (MRJ) of Superballs [57]. In a MRJ simulation the measured cubatic order

parameter is such that $S_4 \approx 0.03$ to 0.32, increasing as $\gamma - 1$. The final mean contact number distribution shows that when superballs undergo MCM the fraction of rattles increases with the deformation parameter (see Figure 4.4.2). This is also a clear different with respect to the MRJ state of superballs, in which the fraction of rattlers decreases with increasing γ. These differences with respect to the MCM is a clear indication that the state achieved for sharp superballs undergoing MCM upon a certain critical deformation parameter is not a MRJ state, but for sure a random packing superballs. This makes sense if we realize that even the random state for spheres obtained with the MCM is not strictly 0.64, but a sightly lower value of 0.62. It may be always taken into account that the stopping criteria for the MCM is that not a single particle overlap can be removed, and that the particles are considered to be frictionless in this framework. Further force calculations (with totally different algorithms) in the final configuration would provide information about the mechanical equilibrium.

Provided that the contact number obtained for spheres is the expected one within the MCM framework, Figure 4.12 shows that the contact number decreases linearly as particles become sharper. Comparison with the long rod case is here also possible. The effect of the higher available contact area for rods provided a higher contact number than for spheres in the final random configuration. The anisotropy arising from increasing γ for superballs produce an increasing in their surface by sharpening the particle. The independence of S_4 with γ indicates that flat faces do not align (even at high γ). The contact surface actually decreases, lowering the average contact number per particle in the final random state. This lack of alignment among the flat faces of particles is direct consequence of how the MCM approaches the random state. Particles are frozen, and their orientation and position are only modified upon squash of the simulation box. From a physical point of view, all fluctuations are simply neglected within this framework (as if the box were squashed at a infinity speed).

Figure 4.4.2 presents the final configuration of the system with increasing γ, from spheres to very cubic particles. As can be seen, not particle alignment is ever present, and the final random configuration is confirmed by the radial distribution functions and the order parameters. Not being the maximally jammed random sate possible for superballs, what the MCM procedure produces is for sure the highest packing fraction at the most random configuration of superballs.

This situation of superballs undergoing MCM is really far from reality. Due to the flatting of the particle faces superballs tend very quickly to align with the container walls and also to align the flat faces between them, producing a higher packing fraction. Even more, macroscopic packings of dice show that flat faces

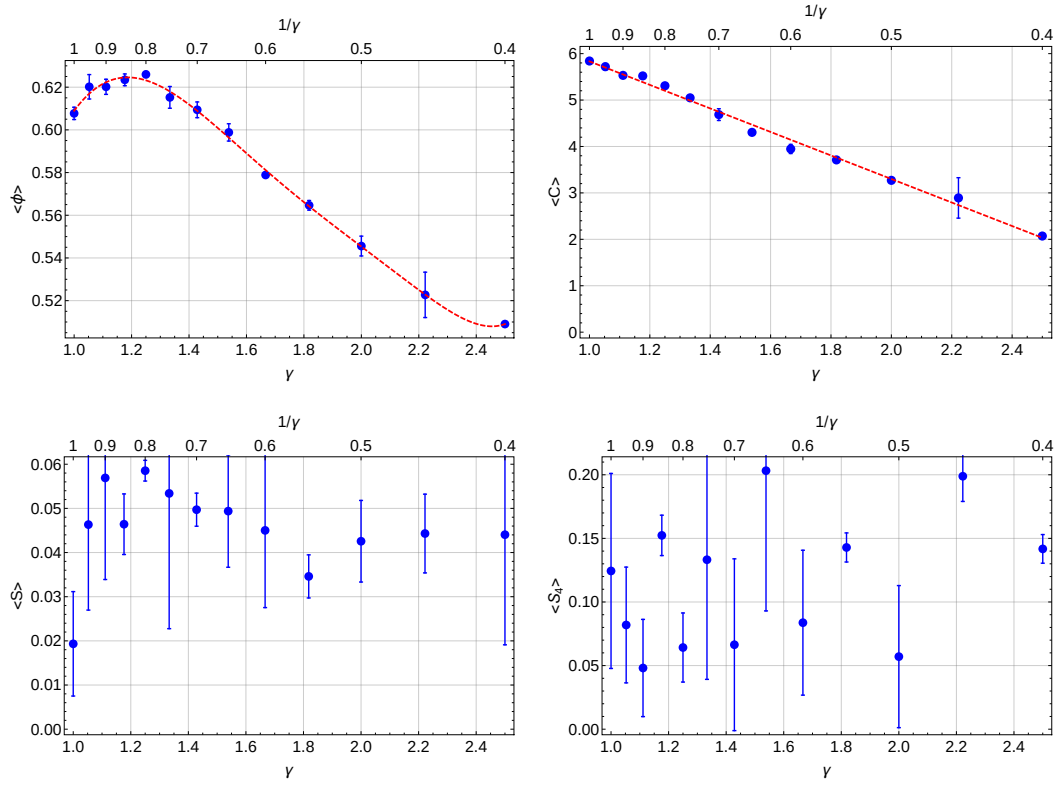

Figure 4.12: Final packing fraction ϕ (top, left), mean contact number $\langle C \rangle$ (top,right), nematic order parameter S_2 (bottom, left) and cubatic order parameter S_4 (bottom, right) as a function of the overlap removal rate β for spheres and small sphere deviation ($\gamma = 5/4$) averaged over three different initial configuration of 750 hard superballs. The red line present for the packing fraction comes from a sixth polynomial order approximation of the results. Red line for the final mean contact number is obtained by a simple linear model fit.

align, and this situation does not recall any kind of energy fluctuations. This must be related then with the lack of friction in the MCM.

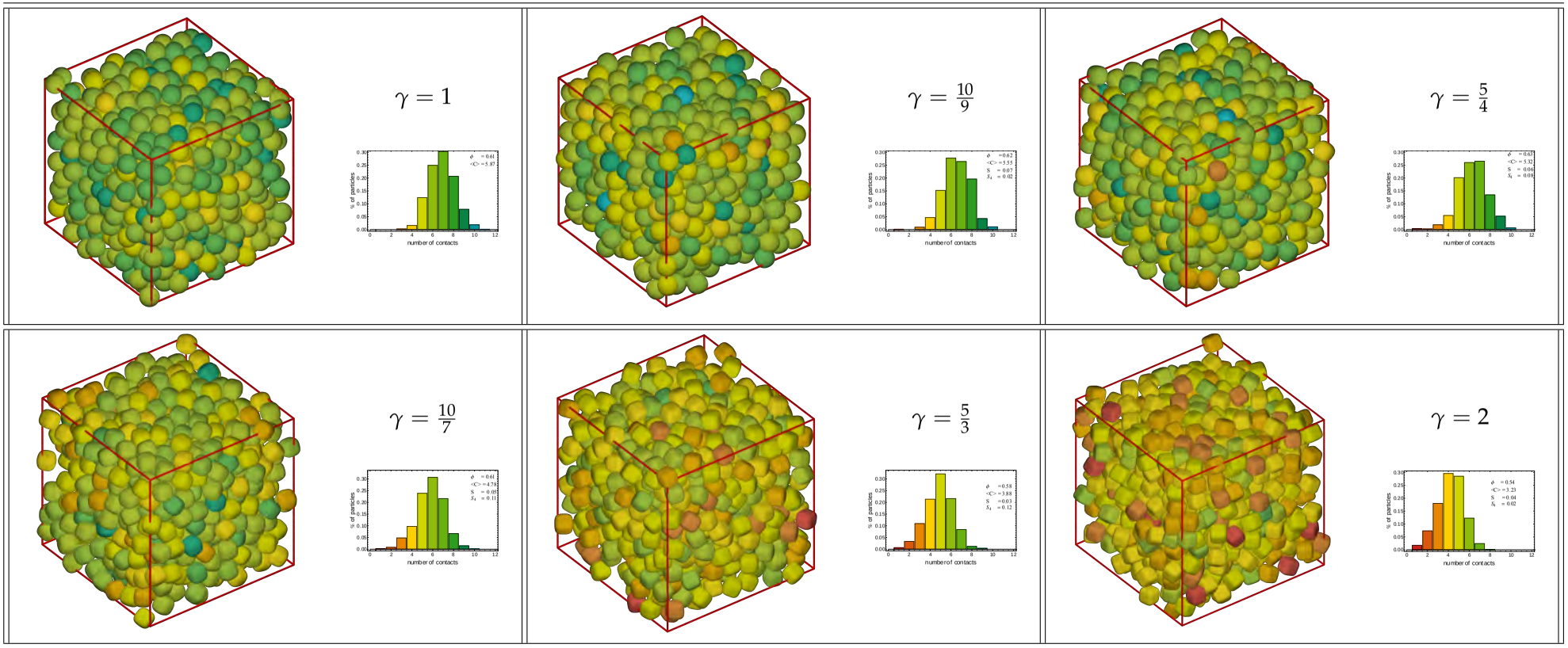

Table 4.2: Final random configuration for a system of 150 hard superballs undergoing a Mechanical Contraction Method, with their corresponding final mean observables and contact number distribution. The colors of the particles in the simulation box and in the contact distribution follow a one to one relation.

The Mechanical Contraction Method has been implemented for general convex shapes. Results arising from random packings of superballs are compared the only available literature available, showing the clear difference between the two algorithms. The characteristics exhibited by this random state of superball are meaningful, and the state achieved is probably the most random packing achievable for superballs (yet not the most dense). Not the maximally random jammed state though, but a state in which the cubatic order parameter does not exhibit a dependence with particle asphericity. Applicability of the ideas here present (enveloping sphere approximation, accurate contact detection) for superballs should be applied in other simulation methods and expanded of course to the general superquadric equation.

Experimental analysis of the structure of colloidal cubes with the height in a sedimentation procedure would actually provide information of the regions where a crystal, plastic crystal and random packing can be found. Further studies in the simulations performed should provide better insight in the actual final state of a random packing of superballs via MCM: the radial distribution function at $\gamma = 5/4$ for MCM looks similar to the one of a MC simulation in the NVT ensemble at a similar packing fraction. Tracing the boundaries between plastic fcc crystal phase and random packings of superball could eventually produce equation of state for the glass transition for superballs, as was done for rods in Chapter 2.

Although the results presented concern the packing properties of a random state of superballs, the contact detection algorithm presented here opens a window for a broad range of superquadric shapes. The feasibility of this contact detection was checked by means of Monte Carlo Simulations [98], and this may provide insight in the search of new phases in between the ones exhibited by rods and ellipsoids. All algorithm modifications explained or suggested along in this project also find its applicability for superquadrics. Another direction is moving towards the random states of bimodal superballs. Being the packing of rod-sphere mixture already defined, it can be of interest studying the final configuration for cubic-like and spheres mixtures. The major advantage of using superquadrics is clear: they recover almost any analytical shape with the proper choice of parameters.

A

SHAPES, VOLUMES AND SURFACES

Here some of the main features concerning the shapes studied in this document are presented. The table on the next page provides a quick reference for further studies on these shapes. An example of the considered shape is presented, together with its surface definition (implicit equation), its volume and its surface area.

The latter presents some mathematical complications. Whereas a volume can be defined as an integral over infinitesimal volume elements, the calculation of the surface area requires derivatives of the parametric equation. Provided a general parametric surface which is *piecewise smooth*:
$S_D : \vec{r} = \vec{r}(u, v)$ with $(u, v) \in D$
with a continuously differentiable function $\vec{r}$, the area of an individual piece is defined by $A(S_D) = \int\int_D |\vec{r}_u \times \vec{r}_v|$, where $\vec{r}_u$ and $\vec{r}_v$ are the partial derivatives of the surface $\vec{r}$ with respect to its parameters u and v. Figure A.1 presents the results obtained for extended superballs (either concave and convex) with its polynomial approximation (up to a fith-order).

$$\vec{r}(\theta,\phi) = \left(a_x \cos^{\varepsilon_x}\theta \cos^{\varepsilon_x}\phi, a_y \cos^{\varepsilon_y}\theta \sin^{\varepsilon_y}\phi, a_z \sin^{\varepsilon_z}\theta\right)$$

$$A(S_D) = \int\int_D |\vec{r}_\theta \times \vec{r}_\phi| =$$

$$8\int_0^{\pi/2}\int_0^{\pi/2} \Bigg(\left(a_x a_y \varepsilon_x \varepsilon_y \sin\theta \cos^{\varepsilon_x - 1}\phi \sin^{\varepsilon_y - 1}\phi \cos^{\varepsilon_x + \varepsilon_y - 1}\theta\right)^2$$

$$+ \left(a_x a_z \varepsilon_x \varepsilon_z \sin\phi \cos^{\varepsilon_x + 1}\theta \cos^{\varepsilon_x - 1}\phi \sin^{\varepsilon_z - 1}\theta\right)^2$$

$$+ \left(a_y a_z \varepsilon_y \varepsilon_z \cos\phi \cos^{\varepsilon_y + 1}\theta \sin^{\varepsilon_y - 1}\phi \sin^{\varepsilon_z - 1}\theta\right)^2 \Bigg)^{1/2}$$

$$\mathrm{d}v\ \mathrm{d}u$$

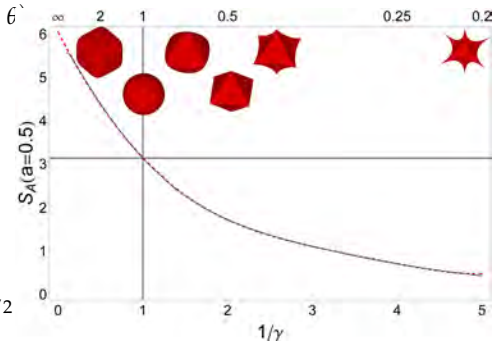

Figure A.1

The general method described can be applied to all shapes in Table A.1. Notice that already the surface area for an ellipsoid requires the incomplete elliptic integrals of first ($F(\phi, k)$) and second ($E(\phi, k)$) kind. The concrete expression for superball's surface is retrieved by taking ($a_1 = a_2 = a_3$) and ($\epsilon_1 = \epsilon_2 = \epsilon_3 = 2\gamma$). Notice that for the integration the *parametric form* of the surface equation is needed,

whereas the surface definitions presented are in the *implicit form*. The book *Segmentation and Recovery of Superquadrics* [97] presents further details about superquadric shapes.

Shape	Sample image	Implicit surface definition	Volume	Surface area
Sphere	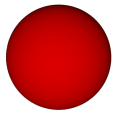	$x^2+y^2+z^2=R^2$	$\frac{4}{3}\pi R^3$	$4\pi R^2$
Spherocylinder		$\begin{cases} x^2+y^2=R^2, \text{ if } \lvert z\rvert \le \frac{L}{2} \\ \sum\limits_{k=x,y,z}(k-\frac{L}{2})^2, \text{ if } \lvert z\rvert > \frac{L}{2} \end{cases}$	$\frac{4}{3}\pi R^3+\pi R^2 L$	$4\pi R^2+2\pi RL$
Ellipsoid	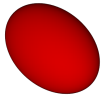	$(\frac{x}{a_x})^2+(\frac{y}{a_y})^2+(\frac{z}{a_z})^2=1$	$\frac{4}{3}\pi a_x a_y a_z$	$4\pi a_z^2+\frac{2\pi a_x a_y}{\sin\phi}$ $\left(E(\phi,k)\sin^2\phi+F(\phi,k)\cos^2\phi\right)$ $\cos\phi=\frac{a_z}{a_x}$, $k^2=\frac{a_x^2(a_y^2+a_z^2)}{a_y^2(a_x^2-a_z^2)}$, $a_x \ge a_y \ge a_z$
Cube		$\lvert k\rvert = L/2$, $k=x,y,z$	L^3	$6L^2$
Superball	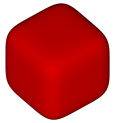	$\lvert x\rvert^{2\gamma}+\lvert y\rvert^{2\gamma}+\lvert z\rvert^{2\gamma}=a^{2\gamma}$	$\frac{8a^3\Gamma\left(1+\frac{1}{2\gamma}\right)^3}{\Gamma\left(1+\frac{3}{2\gamma}\right)}$	$6.058-3.822(1/\gamma)+0.953(1/\gamma)^2$ $-0.012(1/\gamma)^3-0.032(1/\gamma)^4$ $+0.004(1/\gamma)^5$
Supercuboid	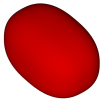	$\lvert \frac{x}{a_x}\rvert^{2\gamma}+\lvert \frac{y}{a_y}\rvert^{2\gamma}+\lvert \frac{z}{a_z}\rvert^{2\gamma}=1$	$\frac{8a_x a_y a_z\Gamma\left(1+\frac{1}{2\gamma}\right)^3}{\Gamma\left(1+\frac{3}{2\gamma}\right)}$	Non analytical
Superellipsoid	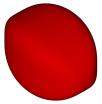	$\left(\left(\frac{x}{a_x}\right)^{\frac{2}{\gamma_2}}+\left(\frac{y}{a_y}\right)^{\frac{2}{\gamma_2}}\right)^{\frac{\gamma_2}{\gamma_1}}+\left(\frac{z}{a_z}\right)^{\frac{2}{\gamma_1}}=1$	$2a_x a_y a_z\gamma_1\gamma_2$ $\frac{\Gamma\left(\frac{\gamma_1}{2}+1\right)\Gamma(\gamma_1)\Gamma\left(\frac{\gamma_2}{2}\right)\Gamma\left(\frac{\gamma_2}{2}\right)}{\Gamma\left(\frac{3\gamma_1}{2}+1\right)\Gamma(\gamma_2)}$	Non analytical
Superquadric		$\left(\frac{x}{a_x}\right)^{\varepsilon_x}+\left(\frac{y}{a_y}\right)^{\varepsilon_y}+\left(\frac{z}{a_z}\right)^{\varepsilon_z}=1$	$\frac{8a_x a_y a_z}{\varepsilon_z}\frac{\Gamma\left(1+\frac{1}{\varepsilon_x}\right)\Gamma\left(1+\frac{1}{\varepsilon_y}\right)\Gamma\left(\frac{1}{\varepsilon_z}\right)}{\Gamma\left(1+\frac{1}{\varepsilon_y}+\frac{1}{\varepsilon_z}+\frac{1}{\varepsilon_x}\right)}$	Non analytical

Table A.1

B

OVERLAP REMOVAL DETAILS

The present appendix is of high relevance concerning the overlap removal defined in the Mechanical Contraction method. The details of the energy-constraint solution are derived here in details, together with which simplifications or numerical approximations are taken into account. Yet the order of the chapters explain the MCM as increasing particle complexity, here the optimization problem is presented in a general case. The particular derivation for spheres and rods come upon certain considerations. In any case, the method used to optimize the velocity of overlap removal is Lagrange constraint optimization.
The minimization is performed assuming that only one contact is present: particle i removes its overlap upon contact with particle j. Generalization for the sum of all overlaps as presented in the corresponding chapters is straightforward. A simplified version of the analytical solution here presented is used in the actual program code (except for spheres). In the case of the mono modal simulations actually performed, this did not affect the final configuration, but for future expansion of the MCM the incorporation of the full analytical solution should be taken into account.

The $6D$ velocity vector that contains all overlap removal velocities is defined as:

$$\boldsymbol{a}_i \;=\; \left(\boldsymbol{a}_i^{\mathrm{L}}, \boldsymbol{a}_i^{\mathrm{R}}\right) \;=\; \left(a_i^{\mathrm{L}x}, a_i^{\mathrm{L}y}, a_i^{\mathrm{L}z}, a_i^{\mathrm{R}x}, a_i^{\mathrm{R}y}, a_i^{\mathrm{R}z}\right) \tag{B.1}$$

$\boldsymbol{a}_i$ was chosen as the velocity vector for keeping the notation set in the original paper [58]. Any other numerical choice is possible: instead of having a factor of 1 in all derivations, a constant factor will be present.

B.1 GENERAL CONVEX SHAPE

With the definition of the $6D$ velocity vector of overlap removal defined with the numerical approximation $2E_k = m_i$ for each particle i, the most general case to get the velocity components consist of minimizing:

$$\frac{\partial|\boldsymbol{\delta}_{ij}|}{\partial t} = \left(\boldsymbol{a}_{i,\mathrm{L}} + \boldsymbol{a}_{i,\mathrm{R}} \times \boldsymbol{r}_{Cij}\right) \cdot \hat{\boldsymbol{n}}_{Cij} \tag{B.2}$$

subject to the kinetic energy constraint upon considering the general numerical approximation $2E_{k,i} = m_i$. What this implies (as will be shown in the final solution)

is that bigger/denser particles will move less than smaller/less dense ones . The moment of inertia of a particle i with a certain shape S can be always expressed by a diagonal matrix $\hat{I}_{i,S}$ when the rotational axes are the main axes of the particle:

$$\hat{I}_{i,S} = \begin{pmatrix} I_{i,x'} & 0 & 0 \\ 0 & I_{i,y'} & 0 \\ 0 & 0 & I_{i,z'} \end{pmatrix} \tag{B.3}$$

The kinetic energy constraint can be then be expressed as:

$$m_i \boldsymbol{a}_i^{\mathrm{L}} \cdot \boldsymbol{a}_i^{\mathrm{L}} + \boldsymbol{a}_i^{\mathrm{R}} \cdot \hat{I}_{i,S} \cdot \boldsymbol{a}_i^{\mathrm{R}} - 1 \;=\; 0 \tag{B.4}$$

Using all this information the Lagrangian, all derivatives of the Lagrangian are expressed in terms of one unique parameter λ. This factor is obtained by substituting its value in the energy like constraint.

$$\begin{array}{lcl} F(\boldsymbol{a}_i, \lambda) & = & \boldsymbol{a}_i^{\mathrm{L}} \cdot \hat{\boldsymbol{n}}_{Cij} + (\boldsymbol{a}_i^{\mathrm{R}} \times \boldsymbol{r}_{Cij}) \cdot \hat{\boldsymbol{n}}_{Cij} - \lambda \left(m_i \boldsymbol{a}_i^{\mathrm{L}} \cdot \boldsymbol{a}_i^{\mathrm{L}} + \boldsymbol{a}_i^{\mathrm{R}} \cdot \hat{I}_{i,C} \cdot \boldsymbol{a}_i^{\mathrm{R}} - 1 \right) \\ \frac{\partial F(\boldsymbol{a}_i,\lambda)}{\partial \boldsymbol{a}_i^{\mathrm{L}}} & = & 0 \rightarrow \boldsymbol{a}_i^{\mathrm{L}} = \frac{\hat{n}_{Cij}}{2\lambda m_i} \\ \frac{\partial F(\boldsymbol{a}_i,\lambda)}{\partial \boldsymbol{a}_i^{\mathrm{R}}} & = & 0 \rightarrow \boldsymbol{a}_i^{\mathrm{R}} = \frac{\left(\hat{n}_{Cij} \times \boldsymbol{r}_{Cij}\right)}{2\lambda m_i \boldsymbol{\epsilon}}, \text{ with } \boldsymbol{\epsilon} = \frac{1}{m_i}(I_{i,x'}, I_{i,y'}, I_{i,z'}) \\ \frac{\partial F(\boldsymbol{a}_i,\lambda)}{\partial \lambda} & = & m_i \boldsymbol{a}_i^{\mathrm{L}} \cdot \boldsymbol{a}_i^{\mathrm{L}} + \boldsymbol{a}_i^{\mathrm{R}} \cdot \hat{I}_i^{C} \cdot \boldsymbol{a}_i^{\mathrm{R}} - 1 \\ \lambda & = & \frac{1}{2\sqrt{m_i}} \sqrt{1 + m_i \left(1 + (\boldsymbol{r}_{Cij} \times \hat{n}_{Cij}) \cdot (\hat{I}_{i,S})^{-1} \cdot (\boldsymbol{r}_{Cij} \times \hat{n}_{Cij})\right)} \end{array} \tag{B.5}$$

For the partial derivative with respect to the rotational components, the scalar triple product properties have been taken into account:

$$\begin{array}{lcl} \left(\boldsymbol{a}_i^R \times \boldsymbol{r}_{Cij}\right) \cdot \hat{n}_{Cij} & = & \hat{n}_{Cij} \cdot \left(\boldsymbol{a}_i^R \times \boldsymbol{r}_{Cij}\right) \\ \hat{n}_{Cij} \cdot \left(\boldsymbol{a}_i^R \times \boldsymbol{r}_{Cij}\right) & = & \boldsymbol{a}_i^R \cdot \left(\boldsymbol{r}_{Cij} \times \hat{n}_{Cij}\right) \\ \frac{\partial F(\boldsymbol{a}_i,\lambda)}{\partial \boldsymbol{a}_i^{\mathrm{R}}} & = & \frac{\partial \left(\boldsymbol{a}_i^R \cdot \left(\boldsymbol{r}_{Cij} \times \hat{n}_{Cij}\right)\right)}{\partial \boldsymbol{a}_i^{\mathrm{R}}} - \lambda \frac{\left(\boldsymbol{a}_i^{\mathrm{R}} \cdot \hat{I}_{i,C} \cdot \boldsymbol{a}_i^{\mathrm{R}}\right)}{\partial \boldsymbol{a}_i^{\mathrm{R}}} \\ \frac{\partial F(\boldsymbol{a}_i,\lambda)}{\partial \boldsymbol{a}_i^{\mathrm{R}}} & = & \left(\boldsymbol{r}_{Cij} \times \hat{n}_{Cij}\right) - 2 m_i \lambda \boldsymbol{a}_i^{\mathrm{R}} \cdot \boldsymbol{\epsilon}, \text{ with } \boldsymbol{\epsilon} = \frac{1}{m_i}(I_{i,x'}, I_{i,y'}, I_{i,z'}) \end{array} \tag{B.6}$$

The final components of the velocity are finally obtained by replacing λ for its particular value. Step by step derivation of the term $(\boldsymbol{r}_{Cij} \times \hat{n}_{Cij}) \cdot (\hat{I}_{i,S})^{-1} \cdot (\boldsymbol{r}_{Cij} \times \hat{n}_{Cij})$ can be sent upon request.

$$\begin{array}{l} \boldsymbol{a}_i^{\mathrm{L}} = \frac{\hat{n}_{Cij}}{\sqrt{m_i}\sqrt{1+m_i\left(1+(\boldsymbol{r}_{Cij}\times\hat{n}_{Cij})\cdot(\hat{I}_{i,S})^{-1}\cdot(\boldsymbol{r}_{Cij}\times\hat{n}_{Cij})\right)}} \\ \boldsymbol{a}_i^{\mathrm{R}} = \frac{\left(\boldsymbol{r}_{Cij}\times\hat{n}_{Cij}\right)}{\boldsymbol{\epsilon}\sqrt{m_i}\sqrt{1+m_i\left(1+(\boldsymbol{r}_{Cij}\times\hat{n}_{Cij})\cdot(\hat{I}_{i,S})^{-1}\cdot(\boldsymbol{r}_{Cij}\times\hat{n}_{Cij})\right)}}, \text{ with } \boldsymbol{\epsilon} = \frac{1}{m_i}(I_{i,x'}, I_{i,y'}, I_{i,z'}) \end{array} \tag{B.7}$$

B.2 SPHERES

The case of spheres is retrieved from the general convex shape just by considering $\hat{I}_{i,sphere} = \mathbf{0} \rightarrow (\hat{I}_{i,sphere})^{-1} = \mathbf{0}$, the formalism for spheres is here shortly expressed. Another way of approaching the problem is by considering that spheres are rotational invariant, and thus overlap will not be removed by any rotation: the $6D$ overlap removal speed is reduce to a $3D$ case such that $\boldsymbol{a}_i = \left(\boldsymbol{a}_i^{\mathrm{L}}, \mathbf{0}\right)$. The optimization consists then on minimizing

$$\frac{\partial |\boldsymbol{\delta}_{ij}|}{\partial t} = \boldsymbol{a}_i^{\mathrm{L}} \cdot \hat{\boldsymbol{n}}_{Cij} \tag{B.8}$$

subject to

$$m_i \boldsymbol{a}_i^{\mathrm{L}} \cdot \boldsymbol{a}_i^{\mathrm{L}} - 1 \;=\; 0 \tag{B.9}$$

Which produces the simple system:

$$\begin{array}{lcl} F(\boldsymbol{a}_i^{\mathrm{L}}, \lambda) & = & \boldsymbol{a}_i^{\mathrm{L}} \cdot \hat{\boldsymbol{n}}_{Cij} - \lambda \left(m_i \boldsymbol{a}_i^{\mathrm{L}} \cdot \boldsymbol{a}_i^{\mathrm{L}} - 1 \right) \rightarrow \boldsymbol{a}_i^{\mathrm{L}} = \frac{\hat{n}_{Cij}}{2\lambda m_i} \rightarrow \boldsymbol{a}_i^{\mathrm{L}} = \frac{\hat{n}_{Cij}}{\sqrt{m_i}} \\ \frac{\partial F(\boldsymbol{a}_i, \lambda)}{\partial \lambda} & = & m_i \boldsymbol{a}_i^{\mathrm{L}} \cdot \boldsymbol{a}_i^{\mathrm{L}} - 1 \\ \lambda & = & \frac{1}{2\sqrt{m_i}} \end{array} \tag{B.10}$$

B.3 SPHEROCYLINDERS

The case of spherocylinders is indeed the most special one. It is clear that overlaps will not be removed by rotations around the z' axes of the particles, chosen to be the main particle axes (see the corresponding rod description in Chapter 2). Taking into account that rods are essentially sweep spheres, it is not surprising to find that the other two particle axes are *degenerated*: it can be an infinite choice of $\hat{u}_{x'}$ and $\hat{u}_{y'}$ particle axes of the cylinder. Thus, the general formalism here used for convex shape can not be directly applied to spherocylinders, as far as we are dealing with a degenerated inertia tensor [99]. It is compulsory to express our rotations according to the particular set of x' and y' vectors chosen. Thus, the usage of distance to the contact point in terms of $K_{ij,x} = \boldsymbol{k}_{ij} \cdot \hat{u}_{i,x'}$ and $K_{ij,y} = \boldsymbol{k}_{ij} \cdot \hat{u}_{i,y'}$ is comprehensible. Furthermore, can use instead of a matrix a simple scalar magnitude, the inertia moment. Independently of the local axes chosen, the moments of inertia associated with rotations ($w_{x'}$,$w_{y'}$) that remove the overlap are equivalent (*parallel axis theorem*), and its expression for rods is well known [100, 101]. It will be simply denoted by I.

Now the constraint optimization problem will consist of minimizing

$$\frac{\partial |\boldsymbol{\delta}_{ij}|}{\partial t} \;=\; \boldsymbol{a}_i \cdot \hat{n}_{Cij} + l_{ij} K_{ij,x} a_i^{\mathrm{R}_x} + l_{ij} K_{ij,y} a_i^{\mathrm{R}_y} \tag{B.11}$$

As an infinite number of particle axes can be chosen for the rods, their moment of inertia is degenerated, but any rotation can be expressed as a combination of trajectories in two planes instead of the most general case of a trajectory being described by three well defined planes. One of the planes is univocally defined by the placement of the first one, which orientation is arbitrary but tangent to z'

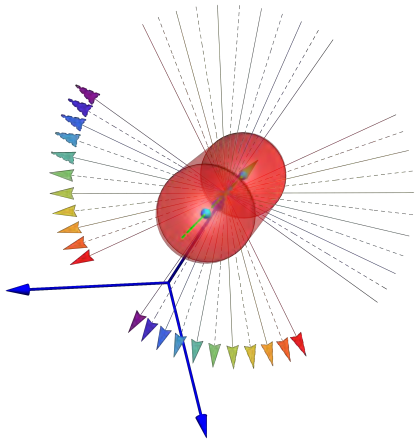

subject to

$$m_i \boldsymbol{a}_i^{\mathrm{L}} \cdot \boldsymbol{a}_i^{\mathrm{L}} + I_i \left((a_i^{\mathrm{R}_x})^2 + (a_i^{\mathrm{R}_y})^2 \right) - 1 = 0 \tag{B.12}$$

Following the same procedure as before, we got:

$$\begin{aligned}
F(\boldsymbol{a}_i, \lambda) &= \boldsymbol{a}_i \cdot \hat{n}_{Cij} + l_{ij} K_{ij,x} a_i^{\mathrm{R}_x} + l_{ij} K_{ij,y} a_i^{\mathrm{R}_y} - \lambda \left(m_i \boldsymbol{a}_i^{\mathrm{L}} \cdot \boldsymbol{a}_i^{\mathrm{L}} + I \left((a_i^{\mathrm{R}_x})^2 + (a_i^{\mathrm{R}_y})^2 \right) - 1 \right) \\
\frac{\partial F(\boldsymbol{a}_i, \lambda)}{\partial \boldsymbol{a}_i^{\mathrm{L}}} &= 0 \rightarrow \boldsymbol{a}_i^{\mathrm{L}} = \frac{\hat{n}_{Cij}}{2\lambda m_i} \\
\frac{\partial F(\boldsymbol{a}_i, \lambda)}{\partial \boldsymbol{a}_i^{\mathrm{R}_x}} &= 0 \rightarrow \boldsymbol{a}_i^{\mathrm{R}_x} = \frac{K_{ij}^x l_{ij}}{2I\lambda} \\
\frac{\partial F(\boldsymbol{a}_i, \lambda)}{\partial \boldsymbol{a}_i^{\mathrm{R}_y}} &= 0 \rightarrow \boldsymbol{a}_i^{\mathrm{R}_y} = \frac{K_{ij}^x l_{ij}}{2I\lambda} \\
\frac{\partial F(\boldsymbol{a}_i, \lambda)}{\partial \lambda} &= m_i \boldsymbol{a}_i^{\mathrm{L}} \cdot \boldsymbol{a}_i^{\mathrm{L}} + I \left((a_i^{\mathrm{R}_x})^2 + (a_i^{\mathrm{R}_y})^2 \right) - 1 \\
\lambda &= \frac{1}{2\sqrt{m_i}} \sqrt{1 + \frac{1}{\epsilon} \left(K_{ij,x}^2 + K_{ji,y}^2 \right)} \text{ ,with } \epsilon = \frac{\mathrm{I}_i}{m_i}
\end{aligned} \tag{B.13}$$

And the final solution for the velocity components will be given as:

$$\begin{aligned}
\boldsymbol{a}_i^{\mathrm{L}} &= \frac{\hat{n}_{Cij}}{\sqrt{m_i} \sqrt{1 + \frac{l_{ij}^2 \left(K_{ij,x}^2 + K_{ij,y}^2 \right)}{\epsilon}}} \\
\boldsymbol{a}_i^{\mathrm{R}_x} &= \frac{K_{ij,x} l_{ij}}{\sqrt{m_i} \epsilon \sqrt{1 + \frac{l_{ij}^2 \left(K_{ij,x}^2 + K_{ij,y}^2 \right)}{\epsilon}}} \\
\boldsymbol{a}_i^{\mathrm{R}_y} &= \frac{K_{ij,y} l_{ij}}{\sqrt{m_i} \epsilon \sqrt{1 + \frac{l_{ij}^2 \left(K_{ij,x}^2 + K_{ij,y}^2 \right)}{\epsilon}}}
\end{aligned} \tag{B.14}$$

In the case of rods, the preference to remove overlap will be simply given in terms of the scalar ϵ: it can be tuned to produce different collections of rods that rotate more or less than expected.

B.4 EXPRESSIONS FOR THE MOMENT OF INERTIA

In this section the particular expressions for the moment of inertia of spherocylinders and the components of the diagonal of the inertia tensor for superquadrics are presented, for future reference and due to the role the play in the overlap removal. In they case of superquadrics, they have been calculated following the procedure for superellipsoids defined in [97]. The moment of inertia with respect to a certain axes, assuming particles with constant density, is given by the distance to the axis r as:

$$I = \int_0^{m_i} r^2 \, \mathrm{d}m \xrightarrow{\rho cst} I = \rho \int_0^V r^2 \, \mathrm{d}V \tag{B.15}$$

B.4.1 *Spherocylinders*

Given a rod with length L_i and diameter D_i, such that $R_i = \frac{D_i}{2}$, its moment of inertia is given is expressed as [100, 101]:

$$\mathrm{I} = \frac{1}{60}\pi\rho R^2 \left(5L^3 + 20L^2R + 45LR^2 + 32R^3\right) \tag{B.16}$$

B.4.2 *Superquadrics*

Following the integration procedure, the moments of inertia with respect to the particle axes for a general superquadric shape (see Appendix A) are given as:

$$\begin{aligned}
I_{i,x'} &= 4a_x a_y a_z \Gamma\left(1+\tfrac{1}{2\varepsilon_x}\right)\left(\frac{a_y^2\Gamma\left(\frac{3}{2\varepsilon_y}\right)\Gamma\left(1+\frac{1}{2\varepsilon_z}\right)}{\varepsilon_y\Gamma\left(\frac{1}{2}\left(\frac{3}{\varepsilon_y}+\frac{1}{\varepsilon_z}+2+\frac{1}{\varepsilon_x}\right)\right)} + \frac{a_z^2\Gamma\left(1+\frac{1}{2\varepsilon_y}\right)\Gamma\left(\frac{3}{2\varepsilon_z}\right)}{\varepsilon_z\Gamma\left(\frac{1}{2}\left(\frac{1}{\varepsilon_y}+\frac{3}{\varepsilon_z}+2+\frac{1}{\varepsilon_x}\right)\right)}\right) \\
I_{i,y'} &= \tfrac{8}{3}a_x a_y a_z \Gamma\left(1+\tfrac{1}{2\varepsilon_y}\right)\left(\frac{a_x^2\Gamma\left(1+\frac{3}{2\varepsilon_x}\right)\Gamma\left(1+\frac{1}{2\varepsilon_z}\right)}{\Gamma\left(\frac{1}{2}\left(\frac{1}{\varepsilon_y}+\frac{1}{\varepsilon_z}+2+\frac{3}{\varepsilon_x}\right)\right)} + \frac{a_z^2\Gamma\left(1+\frac{1}{2\varepsilon_x}\right)\Gamma\left(1+\frac{3}{2\varepsilon_z}\right)}{\Gamma\left(\frac{1}{2}\left(\frac{1}{\varepsilon_y}+\frac{3}{\varepsilon_z}+2+\frac{1}{\varepsilon_x}\right)\right)}\right) \\
I_{i,z'} &= \frac{a_x a_y a_z}{\varepsilon_x\varepsilon_y\varepsilon_z}\Gamma\left(\frac{1}{2\varepsilon_z}\right)\left(\frac{a_x^2\Gamma\left(\frac{3}{2\varepsilon_x}\right)\Gamma\left(\frac{1}{2\varepsilon_y}\right)}{\Gamma\left(\frac{1}{2}\left(\frac{1}{\varepsilon_y}+\frac{1}{\varepsilon_z}+2+\frac{3}{\varepsilon_x}\right)\right)} + \frac{z_y^2\Gamma\left(\frac{1}{2\varepsilon_x}\right)\Gamma\left(\frac{3}{2\varepsilon_y}\right)}{\Gamma\left(\frac{1}{2}\left(\frac{3}{\varepsilon_y}+\frac{1}{\varepsilon_z}+2+\frac{1}{\varepsilon_x}\right)\right)}\right)
\end{aligned} \tag{B.17}$$

Despite its complexity, the expressions successfully reduce to the well known formulas for the moments of inertia for ellipsoids and cubes or the proper choice of ϵ.

As can be seen, the dependence of both linear and rotational components of the velocity with the mass of the particle that is moving when solving analytically the Lagrange optimization problem set is in all cases as $\frac{1}{\sqrt{m_i}}$. Thus, for mono-modal systems it can be simply assumed that $\rho = 1$, and do not incorporate the volume of the particle in any way: the total overlap removal is finally controlled by the overlap removal factor β. As the moment of inertia used for the superballs MCM pack was incorporated by assuming $\rho = 1$ and without dividing by the particle volume, it makes sense that actually a bigger overlap removal rate was indeed needed. In the case of long rods this will not really affect the final result (see Chapter 2, ϵ interpretation). For future expansion to systems of very different particle shape, very different particle volumes or particles with really different density, incorporating this term would provide an improvement. Tuning the density of the particles of the system would allow to simulate, for example, a mixture of frozen spheres (really dense ones, which do not move when the overlap removal takes place) with spheres with $\rho = 1$.

The results from the simulations presented in this report have been done with the simplification

$$\sqrt{1 + m_i \left(1 + (\boldsymbol{r}_{Cij} \times \hat{n}_{Cij}) \cdot (\hat{I}_{i,S})^{-1} \cdot (\boldsymbol{r}_{Cij} \times \hat{n}_{Cij})\right)} \approx 1 \tag{B.18}$$

For very long particles, m_i/I will be very low. For short particles, the distance to the contact point can not be larger than the particle dimensions itself ($\sqrt{a_x^2 + a_y^2 + a_z^2}$). Taking into account that the units used set $D = 1$ for an sphere and that $\rho = 1 \rightarrow m_i = V_i = \pi/6$, this term could actually contribute, but it would produce a higher computational time for our code. This is taken into account by the factor δ_{ij} that accounts for the particles that overlap the most. The formal derivations presented in this appendix should be regarded as a clear improvement for general systems, but it will not really affect the results of mono-modal ones.

C

THE GLASS TRANSITION ASYMPTOTIC MATCHING

This appendix presents in detail the asymptotic matching procedure for the geometrical equation of state for rods (Chapter 2). The three basic equations involved for any rod aspect ratio are:

$$\begin{aligned} Z(\phi)_{\mathrm{CS}} &= \tfrac{1+(3\alpha-2)\phi+(3\alpha-3\alpha+1)\phi^2-\alpha^2\phi^3}{(1-\phi)^3} \\ \alpha &= \tfrac{RS_p}{3V_p} \end{aligned} \tag{C.1}$$

$$Z(\phi)_{\mathrm{GT}} = \frac{\theta}{\phi_{\mathrm{Glass}} - \phi} \tag{C.2}$$

$$Z(\phi)_{\mathrm{full}} = \frac{1 + a_1\phi + a_2\phi + a_3\phi^3}{1 - \phi/\phi_{\mathrm{Glass}}} \tag{C.3}$$

For shorter notation, from now on beyond the final packing fraction produced via MCM will be donoted as ϕ_{G} instead of ϕ_{Glass}. The expansion of $Z(\phi)_{\mathrm{CS}}$ when ϕ is tends to zero is approximate by Taylor expansion up to third order of $(1-\phi)^{-3}$. The results are collected in polynomial terms of ϕ.

$$\begin{aligned} \lim_{\phi\to 0} Z(\phi)_{\mathrm{CS}} &= \left(1 + (3\alpha-2)\phi + (3\alpha-3\alpha+1)\phi^2 - \alpha^2\phi^3\right)\left(1 + 3\phi + \phi^2 + 10\phi^3 + \ldots\right) \\ &= 1 + (3\alpha+1)\phi + \left(3\alpha^2+6\alpha+1\right)\phi^2 + \left(8\alpha^2+9\alpha+1\right)\phi^3 + \ldots \end{aligned} \tag{C.4}$$

The expansion of $Z(\phi)_{\mathrm{full}}$ when ϕ tends to zero comes as well from a Taylor approximation up to third order, in this case of the term $(1-\frac{\phi}{c})^{-1}$:

$$\begin{aligned} \lim_{\phi\to 0} Z(\phi)_{\mathrm{full}} &= \left(1 + a_1\phi + a_2\phi^2 + a_3\phi^3\right)\left(1 + \tfrac{\phi}{\phi_{\mathrm{G}}} + \left(\tfrac{\phi}{\phi_{\mathrm{G}}}\right)^2 + \left(\tfrac{\phi}{\phi_{\mathrm{G}}}\right)^3 + \ldots\right) \\ &= 1 + \phi\left(a_1 + \tfrac{1}{\phi_{\mathrm{G}}}\right) + \phi^2\left(\tfrac{a_1}{\phi_{\mathrm{G}}} + a_2 + \tfrac{1}{\phi_{\mathrm{G}}^2}\right) + \phi^3\left(\tfrac{a_1}{\phi_{\mathrm{G}}^2} + \tfrac{a_2}{\phi_{\mathrm{G}}} + a_3 + \tfrac{1}{\phi_{\mathrm{G}}^3}\right) + \ldots \end{aligned} \tag{C.5}$$

By comparing the powers of ϕ of both low packing fraction expansions, the coefficients a_1,a_2 and a_3 can be obtained.

$$\begin{aligned} a_1 &= \frac{-1+3\alpha\phi_G+\phi_G}{\phi_G} \\ a_2 &= \frac{-1-3\alpha+3\alpha^2\phi_G+6\alpha\phi_G+\phi_G}{\phi_G} \\ a_3 &= \frac{-1-3\alpha^2-6\alpha+8\alpha^2\phi_G+9\alpha\phi_G+\phi_G}{\phi_G} \end{aligned} \tag{C.6}$$

Adding more power coefficients in the low packing fraction expansion would only provide functions that are closer to the one of the CS equation. It is not really worth to go beyond a third power for a small packing fraction equation. Furthermore, a forth term added to the polynomial series that approximates the geometrical equation of state would be related with the coefficient θ that determinate the concrete asymptotic approach. That is, the third order approximation is overestimating the influence of the low packing fraction contribution. Here the case of a fourth order approximation is also explained. If we want a fourth order polynomial the complete full geometric equation of state will be given as:

$$Z(\phi)_{\text{full},4} = \frac{1 + a_1\phi + a_2\phi + a_3\phi^3 + a_4\phi^4}{1 - \phi/\phi_{\text{Glass}}} \tag{C.7}$$

The new coefficient a_4 will depend on the ones previously calculated, as far as the low Z expansion was made up to third order in ϕ. Thus, the limiting equality will provide the value of a_4, but the coefficients a_1,,a_2 and a_3 will remain the same.

$$\begin{aligned} \lim_{\phi\to\phi_G} Z(\phi)_{\text{full},4} &= \frac{1+a_1\phi_G+a_2\phi_G+a_3\phi_G^3+a_4\phi_G^4}{1-\phi/\phi_G} = \frac{\theta/\phi_G}{1-\phi/\phi_G} \\ a_4 &= \frac{-\left(8\alpha^2+9\alpha+1\right)}{\phi_G} - \frac{\theta}{\phi_G} \end{aligned} \tag{C.8}$$

Notice how big the influence of the term $\frac{\theta}{\phi_G}$ is in the fourth order approximation, specially for long rods (where ϕ_G is very low). Having not knowledge about the concrete value of this term, a third order approximation is more than a good approach. By lower order approximations, we are overestimating the influence of the low packing fraction function, yet the asymptotic behavior is present and quantitative physical behavior is retained. Furthermore, taking into account that the behavior showed by the first, second and third order approximations should be retained, a very crude first value of θ could be provided by matching the shape of the provided functions with the ones of the third order approximation (a kind of data collapse). The next page presents the scaled geometrical equations of state for the glass transition for rods of variable aspect ratio, from 1 to 100 approximated by different polynomial order. The line follow a rainbow color series: purple stands for $\lambda = 1$ and red for $\lambda = 100$.

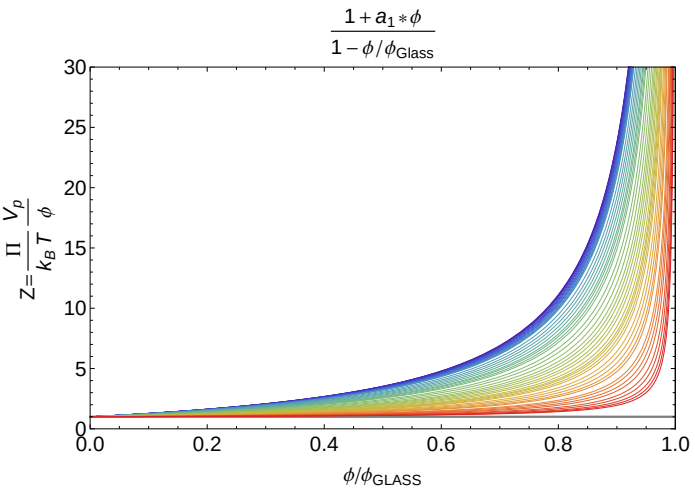
$\frac{1+a_1*\phi}{1-\phi/\phi_{Glass}}$
$Z=\frac{\Pi}{k_B T}\frac{V_p}{\phi}$
0
5
10
15
20
25
30
0.0
0.2
0.4
0.6
0.8
1.0
ϕ/ϕ_{GLASS}

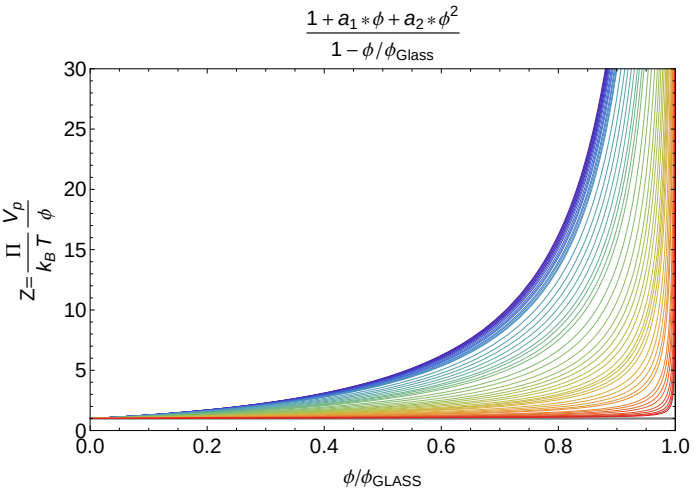
$\frac{1+a_1*\phi+a_2*\phi^2}{1-\phi/\phi_{Glass}}$
$Z=\frac{\Pi}{k_B T}\frac{V_p}{\phi}$
0
5
10
15
20
25
30
0.0
0.2
0.4
0.6
0.8
1.0
ϕ/ϕ_{GLASS}

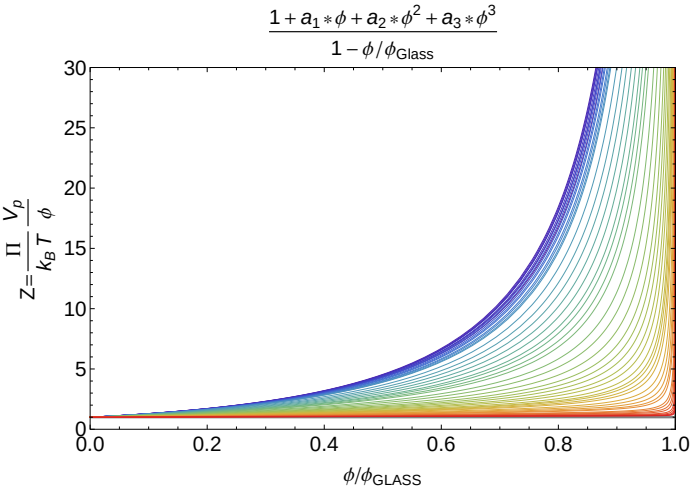
$\frac{1+a_1*\phi+a_2*\phi^2+a_3*\phi^3}{1-\phi/\phi_{Glass}}$
$Z=\frac{\Pi}{k_B T}\frac{V_p}{\phi}$
0
5
10
15
20
25
30
0.0
0.2
0.4
0.6
0.8
1.0
ϕ/ϕ_{GLASS}

D

VIRTUAL ROD IN A PLANE

Here we derive a simple formula for the calculation of the centroid of a spherocylinder parallel to a plane, maximizing the overlap of another spherocylinder intersecting this plane. This position will be the one of the virtual rod used for defining the hard boundary of the wedge in Chapter 3, but the method is general. The frame of reference with respect the equations are presented here is the one with respect the wedge is scaled during the squash: the prism centroid is at $(\frac{1}{3}w_b, \frac{1}{3}w_h, \frac{1}{2}w_d)$ with respect to a system with origin in one of the corners of the wedge (see D.1).

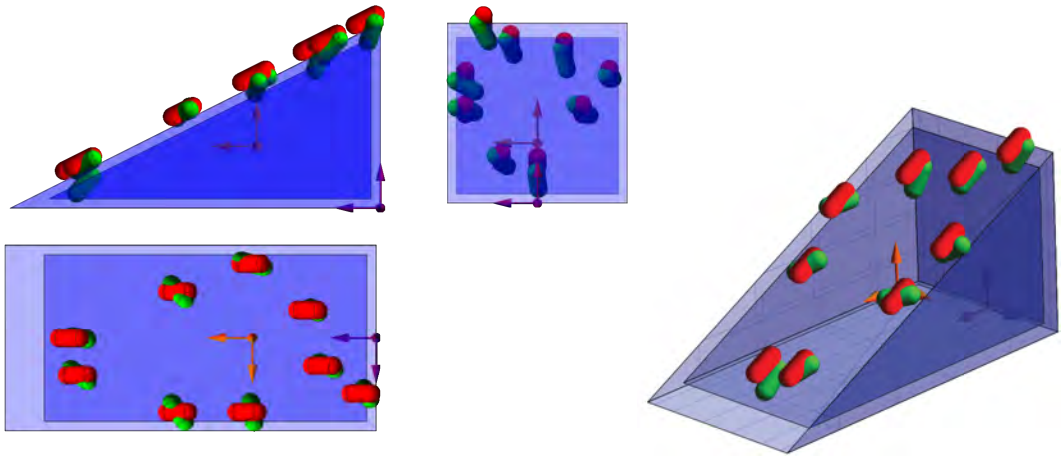

Figure D.1: The considered problem with a collection of rods touching the slope (green) and their corresponsding virtual rods (red).

Start by consider a right triangular prism with dimensions $w_b \times w_h \times w_d$, corresponding to the x, y and z axes. The 'sloped' surface of the prism S is determined by the angle θ given by $\tan\theta = \frac{w_h}{w_b}$. Lets also consider a spherocylinder A a with radius R, length L and orientation $\hat{r}$, such that its endpoints are given as in Chapter 2:

$$\boldsymbol{p}_\pm \quad = \quad \boldsymbol{x} \pm \tfrac{1}{2}L\hat{R} \tag{D.1}$$

When A is placed randomly inside the prism, it may intersect S. If so, we calculate the point of intersection $\mathbf{q}$ and place an identical spherocylinder B such that

it is parallel to, and in contact with S and has maximal overlap with A (see Figure D.1). The centroid of B is given by $\mathbf{c} = \mathbf{q} + R\hat{\mathbf{n}}$, where $\hat{\mathbf{n}}$ is the unit vector normal to S.

In order to determine q, we first need to determine which endpoint causes A to intersect S. Intersection occurs when the following holds

$$p(y)_{1,2} > \left(p(x)_{1,2} + \frac{1}{3}w_\mathrm{b}\right)\tan\theta - R\left[1/\tan\left(\frac{\pi}{4} - \frac{\theta}{2}\right) - \tan\theta\right]$$

There is no intersection when this condition is not satisfied for $\mathbf{p}_1$ and $\mathbf{p}_2$. Call the intersecting point $\mathbf{p}$.

Point $\mathbf{q}$ can be determined by calculating the intersection of S with a line normal to S and passing trough $\mathbf{p}$. We use the method as described by Paul Bourke [102].

For a general plane $Ax + By + Cz + D = 0$ and an intersecting line going through points $\mathbf{P}_1 = (x_1, y_1, z_1)$ and $\mathbf{P}_2 = (x_2, y_2, z_2)$, the intersecting point $\mathbf{P}$ is given by

$$\mathbf{P} = \mathbf{P}_1 + u(\mathbf{P}_2 - \mathbf{P}_1)$$

and the value of u is given by

$$u = \frac{Ax_1 + By_1 + Cz_1 + D}{A(x_1 - x_2) + B(y_1 - y_2) + C(z_1 - z_2)}$$

For our system we take the following values for the parameters

$$\begin{array}{lcll} A & = & \frac{w_\mathrm{h}}{w_\mathrm{b}} & \Rightarrow \quad w_\mathrm{h} \\ B & = & -1 & \Rightarrow \quad -w_\mathrm{b} \\ C & = & 0 & \Rightarrow \quad 0 \\ D & = & \frac{1}{3}w_\mathrm{h} & \Rightarrow \quad \frac{1}{3}w_\mathrm{h}w_\mathrm{b} \\ (x_1, y_1, z_1) & = & \mathbf{p} & \\ (x_2, y_2, z_2) & = & \mathbf{p} + (-\sin\theta, \cos\theta, 0) & \end{array}$$

Filling in for u gives

$$u = \frac{w_\mathrm{h}p_x - w_\mathrm{b}p_y + \frac{1}{3}w_\mathrm{h}w_\mathrm{b}}{w_\mathrm{h}\sin\theta + w_\mathrm{b}\cos\theta}$$

This gives $\mathbf{q}$ after some rewriting

$$
\begin{aligned}
\mathbf{q} &= \mathbf{p} + u(-\sin\theta, \cos\theta, 0) \\
&= (p_x, p_y, p_z) + \left(-\tfrac{w_\mathrm{h} p_x - w_\mathrm{b} p_y + \frac{1}{3} w_\mathrm{h} w_\mathrm{b}}{w_\mathrm{h} \sin\theta + w_\mathrm{b} \cos\theta} \sin\theta, \tfrac{w_\mathrm{h} p_x - w_\mathrm{b} p_y + \frac{1}{3} w_\mathrm{h} w_\mathrm{b}}{w_\mathrm{h} \sin\theta + w_\mathrm{b} \cos\theta} \cos\theta, 0 \right) \\
&= \left(w_\mathrm{b} \tfrac{p_x \cos\theta + p_y \sin\theta - \frac{1}{3} w_\mathrm{h} \sin\theta}{w_\mathrm{b} \cos\theta + w_\mathrm{h} \sin\theta}, w_\mathrm{h} \tfrac{p_x \cos\theta + p_y \sin\theta + \frac{1}{3} w_\mathrm{b} \cos\theta}{w_\mathrm{b} \cos\theta + w_\mathrm{h} \sin\theta}, p_z \right)
\end{aligned}
$$

This can be further simplified by using the fact that $w_\mathrm{h} = w_\mathrm{b} \tan\theta$ and $1/(\cos\theta + \tan\theta \sin\theta) = \cos\theta$. This gives

$$
\mathbf{q} = \left(\cos\theta \left[p_x \cos\theta + p_y \sin\theta - \frac{w_\mathrm{h}}{3} \sin\theta \right], \sin\theta \left[p_x \cos\theta + p_y \sin\theta + \frac{w_\mathrm{b}}{3} \cos\theta \right], p_z \right)
$$

To find the centroid of the contacting spherocylinder B we need to translate $\mathbf{q}$ a distance r normal to S. The normal direction is given by $(-\sin\theta, \cos\theta, 0)$, or equivalently by $(-\cos\theta \tan\theta, \sin\theta / \tan\theta, 0)$ so that

$$
\begin{aligned}
\mathbf{c} &= \mathbf{q} + R\hat{\mathbf{n}} \\
&= \mathbf{q} + (\cos\theta \left[-R \tan\theta \right], \sin\theta \left[R / \tan\theta \right], 0) \\
&= \begin{pmatrix} \cos\theta \left(p_x \cos\theta + p_y \sin\theta - \frac{w_\mathrm{h}}{3} \sin\theta - R \tan\theta \right]) \\ \sin\theta \left(p_x \cos\theta + p_y \sin\theta + \frac{w_\mathrm{b}}{3} \cos\theta + R / \tan\theta \right) \\ p_z \end{pmatrix}
\end{aligned}
$$

This finally gives all the information required.

E

THE ENVELOPING SPHERE RADIUS FOR SUPERQUADRICS

Here the analytical method to obtain the furthest point from the center of a superquadric is derived. The analytical solution is shown in the cases in which it can be obtained: for superballs and for supercuboids. This is done, as commented in Chapter 4, by means of a Langrange multiplier. The most general formulation is presented, and then its corresponding simplifications. Here the analytical method to obtain the furthest point from the center of a superquadric is derived. The analytical solution is shown in the cases in which it can be obtained: for superballs and for supercuboids. This is done, as commented in Chapter 4, by means of a Langrange multiplier. The most general formulation is presented, and then its corresponding simplifications.

E.1 GENERAL PROBLEM SET UP

The square of the distance (d^2) to the center is used as function to minimize, as far as it do not requires the square root present in the absolute distance. Thus, the optimization problem consists of minimizing

$$d^2 = x^2 + y^2 + z^2 \tag{E.1}$$

constraint to

$$\left(\frac{x}{a_x}\right)^{\varepsilon_x} + \left(\frac{y}{a_y}\right)^{\varepsilon_y} + \left(\frac{z}{a_z}\right)^{\varepsilon_z} = 1 \tag{E.2}$$

The Lagrangian Λ that defines our problem, with its corresponding lagrange multiplier λ and its derivatives are defined as:

$$\begin{aligned}
\Lambda &= x^2 + y^2 + z^2 - \lambda\left(\left(\tfrac{x}{a_x}\right)^{\varepsilon_x} + \left(\tfrac{y}{a_y}\right)^{\varepsilon_y} + \left(\tfrac{z}{a_z}\right)^{\varepsilon_z} - 1\right) \\
\frac{\partial\Lambda}{\partial x} &= 2x - \tfrac{\varepsilon_x\lambda}{a_x}\left(\tfrac{x}{a_x}\right)^{\varepsilon_x - 1} = 0 \\
\frac{\partial\Lambda}{\partial y} &= 2y - \tfrac{\varepsilon_y\lambda}{a_y}\left(\tfrac{y}{a_y}\right)^{\varepsilon_y - 1} = 0 \\
\frac{\partial\Lambda}{\partial z} &= 2z - \tfrac{\varepsilon_z\lambda}{a_z}\left(\tfrac{z}{a_z}\right)^{\varepsilon_z - 1} = 0
\end{aligned} \tag{E.3}$$

By rearranging these terms, some of the useful properties later used for obtaining the solution are achieved. Furthermore, the solution describes an ellipsoid with

the axes corresponding to the deformation parameters. In the most general case, this can only be solved numerically.

$$\begin{gathered}\frac{2x^2}{\lambda\varepsilon_x} = \left(\frac{x}{a_x}\right)^{\varepsilon_x} \qquad \frac{2y^2}{\lambda\varepsilon_y} = \left(\frac{y}{a_y}\right)^{\varepsilon_y} \qquad \frac{2z^2}{\lambda\varepsilon_z} = \left(\frac{z}{a_z}\right)^{\varepsilon_z} \\ \frac{2x^2}{\varepsilon_x\lambda} + \frac{2y^2}{\varepsilon_y\lambda} + \frac{2z^2}{\varepsilon_z\lambda} = 1;\end{gathered} \tag{E.4}$$

The point (x, y, z) that verifies E.3 for a certain λ is denoted as $\boldsymbol{x}_\lambda = (x_\lambda, y_\lambda, z_\lambda)$.

E.2 SUPERBALLS

Here the result for the furthest point from a superball center is retrieved from the general case. A calculation of this distance can be found [103], and it ca be easily check that here the same result is retrieved with less assumptions. This simplified case consists of minimizing

$$d^2 = x^2 + y^2 + z^2 \tag{E.5}$$

constraint to

$$(x)^m + (y)^m + (z)^m = a^m \tag{E.6}$$

where by setting $m = 2\gamma$ reduces the formula for the implicit surface of a superball as used in the present project. The solution to the Lagrangian and the final distance from the center of the superball are given as:

$$\begin{aligned}\lambda &= \frac{2a^2 3^{1-\frac{2}{m}}}{m} \\ \boldsymbol{x}_\lambda &= \left(a3^{-1/m}, a3^{-1/m}, a3^{-1/m}\right) \\ d &= \sqrt{3}a\left(\tfrac{1}{3}\right)^{1/m}\end{aligned} \tag{E.7}$$

E.3 SUPERCUBOIDS

Now we take a superball and allow a three different axis deformations. We use the exponent m again due to its closer connection with the general case. Thus, in this case the problem consists of minimizing

$$d^2 = x^2 + y^2 + z^2 \tag{E.8}$$

constraint to

$$\left(\frac{x}{a_x}\right)^m + \left(\frac{y}{a_y}\right)^m + \left(\frac{z}{a_z}\right)^m = 1 \tag{E.9}$$

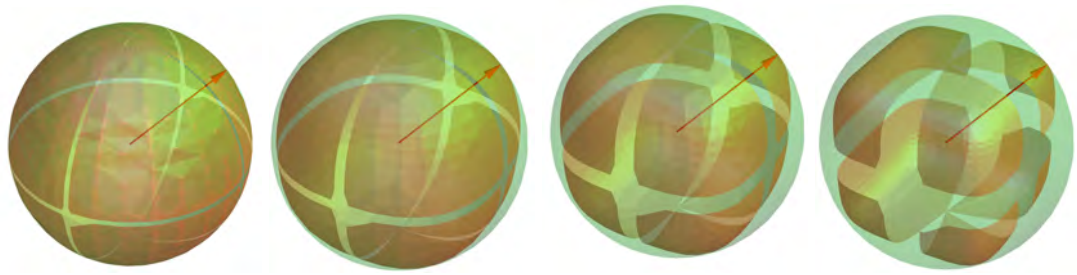

Figure E.1: Final solution for the furthest distance from a superball with the corresponding enveloping sphere. Discontinuities in the surface are due plotting limitations in Mathematica.

which provides the solution

$$\begin{aligned} \lambda &= \frac{2}{m}\left(a_x^{-\frac{2m}{2-m}} + a_y^{-\frac{2m}{2-m}} + a_z^{-\frac{2m}{2-m}}\right)^{\frac{m-2}{m}} \\ \boldsymbol{x}_\lambda &= \left(a_x^{\frac{2m}{m-2}} + a_y^{\frac{2m}{m-2}} + a_z^{\frac{2m}{m-2}}\right)^{-1/m}\left(a_x^{\frac{m}{m-2}}, a_y^{\frac{m}{m-2}}, a_z^{\frac{m}{m-2}}\right) \\ d^2 &= \left(a_x^{\frac{2m}{m-2}} + a_y^{\frac{2m}{m-2}} + a_z^{\frac{2m}{m-2}}\right)^{\frac{m-2}{m}} \end{aligned} \tag{E.10}$$

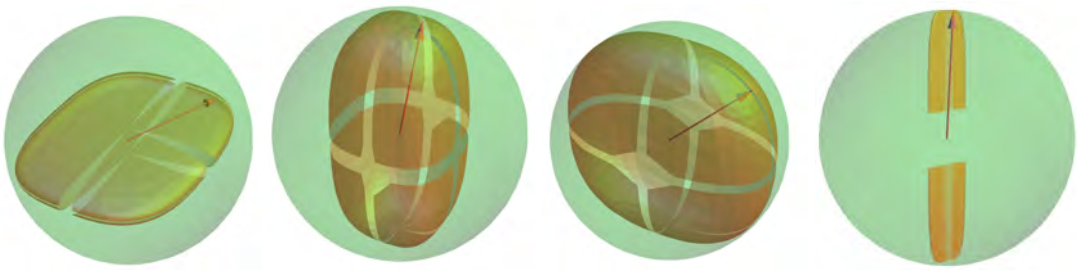

Figure E.2: Final solution for the furthest distance from generic supercuboids with the corresponding enveloping sphere. Discontinuities of the surface are due plotting limitations in Mathematica.

Finally the most general equation is presented for a general superquadric. Equations can be reduced analytically up to:

$$\begin{aligned}
x_\lambda &= 2^{-\frac{1}{2-\varepsilon_x}} a_x^{-\frac{\varepsilon_x}{2-\varepsilon_x}} (\varepsilon_x \lambda)^{\frac{1}{2-\varepsilon_x}} \\
y_\lambda &= 2^{-\frac{1}{2-\varepsilon_y}} a_y^{-\frac{\varepsilon_y}{2-\varepsilon_y}} (\varepsilon_y \lambda)^{\frac{1}{2-\varepsilon_y}} \\
z\lambda &= 2^{-\frac{1}{2-\varepsilon_z}} a_z^{-\frac{\varepsilon_z}{2-\varepsilon_z}} (\varepsilon_z \lambda)^{\frac{1}{2-\varepsilon_z}} \\
\frac{\lambda}{2} &= 2^{-\frac{2}{2-\varepsilon_x}} \varepsilon_x^{\frac{\varepsilon_x}{2-\varepsilon_x}} a_x^{-\frac{2\varepsilon_x}{2-\varepsilon_x}} \lambda^{\frac{2}{2-\varepsilon_x}} + 2^{-\frac{2}{2-\varepsilon_y}} \varepsilon_y^{\frac{\varepsilon_y}{2-\varepsilon_y}} a_y^{-\frac{2\varepsilon_y}{2-\varepsilon_y}} \lambda^{\frac{2}{2-\varepsilon_y}} + 2^{-\frac{2}{2-\varepsilon_z}} \varepsilon_z^{\frac{\varepsilon_z}{2-\varepsilon_z}} a_z^{-\frac{2\varepsilon_z}{2-\varepsilon_z}} \lambda^{\frac{2}{2-\varepsilon_z}}
\end{aligned} \tag{E.11}$$

This equations can simply not be solved analytically.

BIBLIOGRAPHY

[1] B. J. Alder and T. E. Wainwright, "Phase Transition for a Hard Sphere System," *The Journal of Chemical Physics*, vol. 27, no. 5, p. 1208, 1957.

[2] Z. Cheng, P. M. Chaikin, W. B. Russel, W. V. Meyer, J. Zhu, R. B. Rogers, and R. H. Ottewill, "Phase diagram of hard spheres," *Materials and Design*, vol. 22, pp. 529–534, 2001.

[3] F. H. Ree and W. G. Hoover, "Fifth and Sixth Virial Coefficients for Hard Spheres and Hard Disks," *Journal of Chemical Physics*, vol. 40, no. 4, pp. 939–950, 1964.

[4] B. D. Lubachevsky, "How to Simulate Billiards and Similar Systems," *arXiv*, pp. 1–29, 2006.

[5] H. Jean-Pierre and M. Ian R, *Theory of Simple Liquids (fourth edition) With applications to soft matter*, vol. 21. Sept. 2012.

[6] R. L. Davidchack, "Hard spheres revisited: accurate calculation of the solid-liquid interfacial free energy.," *The Journal of chemical physics*, vol. 133, p. 234701, Dec. 2010.

[7] M. N. Rosenbluth and A. W. Rosenbluth, "Further Results on Monte Carlo Equations of State," *The Journal of Chemical Physics*, vol. 22, no. 5, p. 881, 1954.

[8] L. Onsager, "The effects of shape on the interaction of colloidal particles," *Annals of the New York Academy of Sciences*, vol. 51, no. 4, pp. 627–659, 1949.

[9] Y. Jiao, F. Stillinger, and S. Torquato, "Optimal packings of superballs," *Physical Review E*, vol. 79, p. 041309, Apr. 2009.

[10] R. D. Batten, F. H. Stillinger, and S. Torquato, "Phase behavior of colloidal superballs: Shape interpolation from spheres to cubes," *Physical Review E*, vol. 81, p. 061105, June 2010.

[11] R. Ni, A. P. Gantapara, J. de Graaf, R. van Roij, and M. Dijkstra, "Phase diagram of colloidal hard superballs: from cubes via spheres to octahedra," *Soft Matter*, vol. 8, no. 34, p. 8826, 2012.

[12] S. C. McGrother, D. C. Williamson, and G. Jackson, "A re-examination of the phase diagram of hard spherocylinders," *The Journal of Chemical Physics*, vol. 104, no. 17, p. 6755, 1996.

[13] P. J. Camp, C. P. Mason, M. P. Allen, A. a. Khare, and D. a. Kofke, "The isotropic nematic phase transition in uniaxial hard ellipsoid fluids: Coexistence data and the approach to the Onsager limit," *The Journal of Chemical Physics*, vol. 105, no. 7, p. 2837, 1996.

[14] P. Bolhuis and D. Frenkel, "Tracing the phase boundaries of hard spherocylinders," *Journal of Chemical Physics*, vol. 106, no. June 1996, pp. 666–687, 1997.

[15] H. Graf and H. Löwen, "Density functional theory for hard spherocylinders: phase transitions in the bulk and in the presence of external fields," *Journal of Physics: Condensed Matter*, vol. 11, pp. 1435–1452, Feb. 1999.

[16] A. Kuijk, D. V. Byelov, A. V. Petukhov, A. van Blaaderen, and A. Imhof, "Phase behavior of colloidal silica rods," *Faraday Discussions*, vol. 159, p. 181, 2012.

[17] G. Bautista-carbajal, A. Moncho-jord, and G. Odriozola, "Further details on the phase diagram of hard ellipsoids of revolution," 2013.

[18] Alan Wouterse, *Random packing of colloids and granular matter*. PhD thesis, 2008.

[19] L. Rossi, *Colloidal Superballs*. PhD thesis, Utrecht University, 2012.

[20] Joost de Graaf, *Anisotropic Nanocolloids: Self-Assembly, Interfacial Adsorption, and Electrostatic Screening*. PhD thesis, 2012.

[21] P. M. Chaikin, A. Donev, W. Man, F. H. Stillinger, and S. Torquato, "Some Observations on the Random Packing of Hard Ellipsoids," *Industrial & Engineering Chemistry Research*, vol. 45, pp. 6960–6965, Oct. 2006.

[22] B. Bideau and A. hasten, *Disroder and granular media*. Random materials and processes.Elsevier, Amsterdam, 1993.

[23] T. Aste and D. Weaire, *The pursuit of perfect packing*. Institute of Physics Publishing, 2000.

[24] A. P. Philipse, "Caging effects in amorphous hard-sphere solids," *Colloids and Surfaces A: Physicochemical and Engineering Aspects*, vol. 213, pp. 167–173, Feb. 2003.

[25] S. Torquato, T. M. Truskett, and P. G. Debenedetti, "Is Random Close Packing of Spheres Well Defined?," *arXiv*, no. 1, pp. 1–6.

[26] E. R. Nowak, J. B. Knight, E. Ben-naim, H. M. Jaeger, and S. R. Nagel, "Density fluctuations in vibrated granular materials," vol. 57, no. 2, pp. 1971–1982, 1998.

[27] J. B. Knight, C. G. Fandrich, C. Ning Lau, H. M. Jaeger, and S. R. Nagel, "Density relaxation in a vibration.pdf," *Physical Review E*, vol. 51, no. 5, 1995.

[28] C. Song, P. Wang, and H. a. Makse, "A phase diagram for jammed matter.," *Nature*, vol. 453, pp. 629–32, May 2008.

[29] G. D. Scott and D. M. Kilgour, "The density of random close packing of spheres," *Journal of Physics D: Applied Physics*, vol. 2, pp. 863–866, June 1969.

[30] H. Jaeger, S. Nagel, and R. Behringer, "Granular solids, liquids, and gases," *Reviews of Modern Physics*, vol. 68, pp. 1259–1273, Oct. 1996.

[31] A. P. Philipse, "The Random Contact Equation and Its Implications for (Colloidal) Rods in Packings, Suspensions, and Anisotropic Powders," *Langmuir*, vol. 12, pp. 5971–5971, Jan. 1996.

[32] S. Sacanna, L. Rossi, a. Wouterse, and a. P. Philipse, "Observation of a shape-dependent density maximum in random packings and glasses of colloidal silica ellipsoids," *Journal of Physics: Condensed Matter*, vol. 19, p. 376108, Sept. 2007.

[33] "Classifying rice for import and export." https://www.gov.uk/classifying-rice#classifying-the-size-of-the-grain-of-rice. Accessed: 2014-09-23.

[34] A. Baule and H. a. Makse, "Fundamental challenges in packing problems: from spherical to non-spherical particles.," *Soft matter*, vol. 10, pp. 4423–9, July 2014.

[35] J. Baker and A. Kudrolli, "Maximum and Minimum Stable Random Packings of Platonic Solids," *arXiv*, vol. 01610, 2010.

[36] A. Baule, R. Mari, L. Bo, L. Portal, and H. a. Makse, "Mean-field theory of random close packings of axisymmetric particles.," *Nature communications*, vol. 4, p. 2194, Jan. 2013.

[37] "Statistical Ensembles for Jammed Granular States Notes," Tech. Rep. 2007, 2009.

[38] H. Brouwers, "Particle-size distribution and packing fraction of geometric random packings," *Physical Review E*, vol. 74, p. 031309, Sept. 2006.

[39] H. J. H. Brouwers, "Packing fraction of geometric random packings of discretely sized particles," *Physical Review E*, vol. 84, p. 042301, Oct. 2011.

[40] H. Brouwers, "Random packing fraction of bimodal spheres: An analytical expression," *Physical Review E*, vol. 87, p. 032202, Mar. 2013.

[41] D. Asenjo, F. Paillusson, and D. Frenkel, "Numerical calculation of granular entropy," *arXiv*, pp. 1–5, 2014.

[42] A. J. Liu and S. R. Nagel, "Jamming is not just cool any more," *Nature*, vol. 396, no. November, 1998.

[43] S. F. Edwards and R. Oakeshott, "Theory of powders," *Physica A*, vol. 157, pp. 1080–1090, 1989.

[44] B. P. Tighe, A. R. T. van Eerd, and T. J. H. Vlugt, "Entropy maximization in the force network ensemble for granular solids," *Physical Review Letters*, p. 4, Mar. 2008.

[45] P. Duncan, M. Dennison, A. Masters, and M. Wilson, "Theory and computer simulation for the cubatic phase of cut spheres," *Physical Review E*, vol. 79, p. 031702, Mar. 2009.

[46] a. Wouterse, M. Plapp, and a. P. Philipse, "On the caging number of two- and three-dimensional hard spheres.," *The Journal of chemical physics*, vol. 123, p. 054507, Aug. 2005.

[47] O. Stenzel, M. Salzer, V. Schmidt, P. W. Cleary, and G. W. Delaney, "Quantitative structural analysis of simulated granular packings of non-spherical particles," *Granular Matter*, vol. 16, pp. 457–468, Mar. 2014.

[48] B. Widom, "Random Sequential Addition of Hard Spheres to a Volume," *The Journal of Chemical Physics*, vol. 44, no. 10, p. 3888, 1966.

[49] J. D. Sherwood, "Packing of spheroids in three-dimensional space by random sequential addition," vol. 30, pp. 839–843, 1997.

[50] S. Torquato, O. Uche, and F. Stillinger, "Random sequential addition of hard spheres in high Euclidean dimensions," *Physical Review E*, vol. 74, p. 061308, Dec. 2006.

[51] G. Zhang and S. Torquato, "Precise algorithm to generate random sequential addition of hard hyperspheres at saturation," *Physical Review E*, vol. 88, p. 053312, Nov. 2013.

[52] F. H. Stillinger and B. D. Lubachevsky, "Crystalline-Amorphous Interface Packings for Disks and Spheres," *Journal of Statistical Physics*, vol. 73, pp. 497–514, 1993.

[53] B. D. Lubaehevsky and F. H. Stillinger, "Geometric Properties of Random Disk Packings," vol. 60, no. 12, 2000.

[54] A. Donev, S. Torquato, and F. H. Stillinger, "Neighbor List Collision-Driven Molecular Dynamics Simulation for Nonspherical Hard Particles . I . Algorithmic Details," *arXiv*, 2004.

[55] A. Donev, S. Torquato, and F. H. Stillinger, "Neighbor list collision-driven molecular dynamics simulation for nonspherical hard particles. I. Algorithm details," *Journal of Computational Physics*, vol. 202, pp. 737–764, Jan. 2005.

[56] A. Donev, *Jammed Packings of Hard Particles*. PhD thesis, Princeton University, 2006.

[57] Y. Jiao, F. H. Stillinger, and S. Torquato, "Novel Features Arising in Maximally Random Jammed Packings of Superballs," *arXiv*, pp. 1–20, 2010.

[58] S. Williams and a. Philipse, "Random packings of spheres and spherocylinders simulated by mechanical contraction," *Physical Review E*, vol. 67, p. 051301, May 2003.

[59] C. Ferreiro-Córdova and J. S. V. Duijneveldt, "Random Packing of Hard Spherocylinders," *Journal of Chemical engineering*, 2014.

[60] M. Rintoul and S. Torquato, "Metastability and Crystallization in Hard-Sphere Systems.," *Physical review letters*, vol. 77, pp. 4198–4201, Nov. 1996.

[61] A. V. Kyrylyuk, A. Wouterse, A. P. Philipse, M. Nakagawa, and S. Luding, "Random Packings Of Rod-Sphere Mixtures Simulated By Mechanical Contraction," *AIP Conference Proceedings*, pp. 211–214, 2009.

[62] A. V. Kyrylyuk, M. Anne van de Haar, L. Rossi, A. Wouterse, and A. P. Philipse, "Isochoric ideality in jammed random packings of non-spherical granular matter," *Soft Matter*, vol. 7, no. 5, p. 1671, 2011.

[63] A. Wouterse, S. R. Williams, and A. P. Philipse, "Effect of particle shape on the density and microstructure of random packings.," *Journal of physics. Condensed matter : an Institute of Physics journal*, vol. 19, p. 406215, Oct. 2007.

[64] W. Peter, "Candy Science: MMs Pack More Tightly than Spheres.." Science, April 2004.

[65] A. Fortini and M. Dijkstra, "Phase behaviour of hard spheres confined between parallel hard plates: manipulation of colloidal crystal structures by confinement.," *Journal of physics. Condensed matter : an Institute of Physics journal*, vol. 18, pp. L371–8, July 2006.

[66] L. Jiang, J. W. J. de Folter, J. Huang, A. P. Philipse, W. K. Kegel, and A. V. Petukhov, "Helical colloidal sphere structures through thermo-reversible coassembly with molecular microtubes.," *Angewandte Chemie (International ed. in English)*, vol. 52, pp. 3364–8, Mar. 2013.

[67] L. Miao, O. Vanderlinde, J. Liu, R. P. Grant, A. Wouterse, K. Shimabukuro, A. Philipse, M. Stewart, and T. M. Roberts, "The role of filament-packing dynamics in powering amoeboid cell motility.," *Proceedings of the National Academy of Sciences of the United States of America*, vol. 105, pp. 5390–5, Apr. 2008.

[68] L. L. LeClaire, M. Stewart, and T. M. Roberts, "A 48 kDa integral membrane phosphoprotein orchestrates the cytoskeletal dynamics that generate amoeboid cell motility in Ascaris sperm.," *Journal of cell science*, vol. 116, pp. 2655–63, July 2003.

[69] L. Meng, H. Wei, A. Nagel, B. J. Wiley, L. E. Scriven, and D. J. Norris, "The role of thickness transitions in convective assembly.," *Nano letters*, vol. 6, pp. 2249–53, Oct. 2006.

[70] S. Miltenyi, W. Müller, W. Weichel, and a. Radbruch, "High gradient magnetic cell separation with MACS.," *Cytometry*, vol. 11, pp. 231–8, Jan. 1990.

[71] W. R. Inc, "Mathematica Edition: Version 10.0.1," *Wolfram Research, Inc*, 2014.

[72] F. Panneton, P. L. Ecuyer, and M. Matsumoto, "Improved Long-Period Generators Based on Linear Recurrences Modulo 2," *ACM Transactions on Mathematical Software*, vol. V, pp. 1–16, 2006.

[73] T. Gibaud, E. Barry, M. J. Zakhary, M. Henglin, A. Ward, Y. Yang, C. Berciu, R. Oldenbourg, M. F. Hagan, D. Nicastro, R. B. Meyer, and Z. Dogic, "Reconfigurable self-assembly through chiral control of interfacial tension.," *Nature*, vol. 481, pp. 348–51, Jan. 2012.

[74] C. Vega and S. Lago, "A fast algorithm to evaluate the shortest distance between rods," *Computers Chem*, vol. 18, no. 1, pp. 55–59, 1994.

[75] M. Alonso and E. J. Finn, *Physics*. Addison-Wsley Publishing Company, revised ed., 1992.

[76] "The feynman lectures on physics." http://feynmanlectures.caltech.edu/. Accessed: 2014-09-23.

[77] S. S. L. Peppin, J. a. W. Elliott, and M. G. Worster, "Solidification of colloidal suspensions," *Journal of Fluid Mechanics*, vol. 554, p. 147, Apr. 2006.

[78] M. Robins and A. Fillery-Travis, "Colloidal dispersions. edited by w. b. russel, d. a. saville and w. r. schowalter, cambridge university press, cambridge, uk, 1989, xvii + 506 pp., price: Â£60.00. isbn 0 521 34188 4," *Journal of Chemical Technology and Biotechnology*, vol. 54, no. 2, pp. 201–202, 1992.

[79] N. F. Carnahan and K. E. Starling, "Equation of state for nonattracting rigid spheres," *The Journal of Chemical Physics*, vol. 51, no. 2, pp. 635–636, 1969.

[80] T. Boublik, "Statistical thermodynamics of nonspherical molecule fluids," *Berichte der Bunsengesellschaft fÃŒr physikalische Chemie*, vol. 85, no. 11, pp. 1038–1041, 1981.

[81] Y. S. Wei and R. J. Sadus, "Equations of State for the Calculation of Fluid-Phase Equilibria," *Ai ChE Journal*, vol. 46, no. 1, pp. 169–196, 2000.

[82] T. M. Truskett, P. G. Debenedetti, and S. Torquato, "Thermodynamic implications of confinement for a waterlike fluid," *The Journal of Chemical Physics*, vol. 114, no. 5, p. 2401, 2001.

[83] A. Jaoshvili, A. Esakia, M. Porrati, and P. M. Chaikin, "Experiments on the Random Packing of Tetrahedral Dice," *Physical Review Letters*, vol. 104, p. 185501, May 2010.

[84] G. Singh, H. Chan, A. Baskin, E. Gelman, N. Repnin, P. Král, and R. Klajn, "Self-assembly of magnetite nanocubes into helical superstructures.," *Science (New York, N.Y.)*, vol. 1149, July 2014.

[85] V. Meester, *Self-assembly of micron-sized hollow silica cubes using convective assembly methods*. PhD thesis, 2014.

[86] V. R. Dugyala, S. V. Daware, and M. G. Basavaraj, "Shape anisotropic colloids: synthesis, packing behavior, evaporation driven assembly, and their

application in emulsion stabilization," *Soft Matter*, vol. 9, no. 29, p. 6711, 2013.

[87] A. Barr, "Superquadrics and angle-preserving transformations," *Computer Graphics and Applications, IEEE*, vol. 1, pp. 11–23, Jan 1981.

[88] L. Rossi, S. Sacanna, W. T. M. Irvine, P. M. Chaikin, D. J. Pine, and A. P. Philipse, "Cubic crystals from cubic colloids," *Soft Matter*, vol. 7, no. 9, p. 4139, 2011.

[89] J.-M. Meijer, F. Hagemans, L. Rossi, D. V. Byelov, S. I. R. Castillo, A. Snigirev, I. Snigireva, A. P. Philipse, and A. V. Petukhov, "Self-assembly of colloidal cubes via vertical deposition.," *Langmuir : the ACS journal of surfaces and colloids*, vol. 28, pp. 7631–8, May 2012.

[90] J.-M. Meijer, D. V. Byelov, L. Rossi, A. Snigirev, I. Snigireva, A. P. Philipse, and A. V. Petukhov, "Self-assembly of colloidal hematite cubes: a microradian X-ray diffraction exploration of sedimentary crystals," *Soft Matter*, vol. 9, no. 45, p. 10729, 2013.

[91] S. I. R. Castillo, C. E. Pompe, J. van Mourik, D. M. a. Verbart, D. M. E. Thies-Weesie, P. E. de Jongh, and A. P. Philipse, "Colloidal cubes for the enhanced degradation of organic dyes," *Journal of Materials Chemistry A*, vol. 2, no. 26, p. 10193, 2014.

[92] R. Featherstone, *Rigid Body Dynamics Algorithms*. Boston: Springer, 2007.

[93] R. Portal, J. a. Dias, and L. de Sousa, "Contact Detection Between Convex Superquadric Surfaces," *Archive of Mechanical Engineering*, vol. LVII, Jan. 2010.

[94] D. S. Lopes, M. T. Silva, J. a. Ambrósio, and P. Flores, "A mathematical framework for rigid contact detection between quadric and superquadric surfaces," *Multibody System Dynamics*, vol. 24, pp. 255–280, Sept. 2010.

[95] P. D. Duncan, M. Dennison, A. J. Masters, and M. R. Wilson, "Theory and computer simulation for the cubatic phase of cut spheres," *Phys. Rev. E*, vol. 79, p. 031702, Mar 2009.

[96] a. Isihara, "Determination of Molecular Shape by Osmotic Measurement," *The Journal of Chemical Physics*, vol. 18, no. 11, p. 1446, 1950.

[97] A. Jaklič, A. Leonardis, and F. Solina, *Segmentation and Recovery of Superquadrics*, vol. 20 of *Computational imaging and vision*. Dordrecth: Kluwer, 2000. ISBN 0-7923-6601-8.

[98] A. González García, "Monte Carlo Simulations for Superellipsoids in NPT and NVT ensemble," *Report for Modelling and Simulation, UU*, 2014.

[99] "Animation physics, course in computer science, university of british columbia (ubc). http://www.cs.ubc.ca/ rbridson/courses/533d-winter-2005/cs533d-slides-feb23.pdf." http://www.cs.ubc.ca/ rbridson/courses/533d-winter-2005/cs533d-slides-feb23.pdf, note = Accessed: 2014-09-23.

[100] L. Pournin, M. Weber, M. Tsukahara, J.-a. Ferrez, M. Ramaioli, and T. M. Liebling, "Three-dimensional distinct element simulation of spherocylinder crystallization," *Granular Matter*, vol. 7, pp. 119–126, Feb. 2005.

[101] R. Meland, I. R. Gran, J. A. Melheim, S. T. Munkejord, and N. E. Haugen, "CLUSTER INTEGRATION METHOD FOR NON-SPHERICAL GRANULAR PARTICLES," *Fifth International Conference on CFd in the Process Industries*, no. December, pp. 1–4, 2006.

[102] "Minimum distance between a point and a line written by paul bourke." http://paulbourke.net/geometry/pointlineplane/. Accessed: 2014-09-28.

[103] A. G. Brinkman, "Preparations and properties of colloidal cubes," *Literature Study*, 2011.

We have seen that computer programming is an art,
because it applies accumulated knowledge to the world,
because it requires skill and ingenuity, and especially
because it produces objects of beauty.

— Donald E. Knuth, *Computer Programming as an Art*

ACKNOWLEDGMENTS

The best grant that a researcher can find is the complete, unconditional support of his beloved ones. Thanks to my family in the first place. No words could ever express my gratitude. La mejor ayuda que siempre he podido encontrar ha venido de mi familia. ¡Muchísimas gracias!

From now on, acknowledgments will be given in order of distance from home (growing circles from Los Silos, Tenerife, Canary Islands).

Thanks to Prof. Maria Elena Alvira Lechuz for all the wise advice beyond the merely academical. I hope we will keep in touch as we have done so far. Yet, my time at ULL (Universidad de La Laguna) is long time ago ended, I really appreciate the background I received there. And I wish all my colleagues simply the best in all aspects of their lives. ¡Nos vemos en los bares! Special thanks also to Prof. Daniel Alonso Ramírez for introducing me to the fascinating world of statistical physics.

During the last year of my bachelor, I got the opportunity to do research under the supervision of prof. Dr. Angel Delgado at Universidad de Granada. Even more, the reason that I ended in the Netherlands has a name: Julián López-Viota. By taking your advice, I ended at FCC and I found again my passion for physics. ¡Espero verte pronto! Thanks to both of them in particular, and in general to the whole department of Applied Physics at UGR for the great time there.

Thanks to Rebeca V. Herrero Hahn for the detailed correction in one (of the multiple) version of this manuscript. Thanks also to Victor Díez Borge for not a so accurate correction, but still a great interest in this project. I hope to host you both soon again in the Netherlands! ¡Venganse pa'arriba muchachos!

The last circle brings me to Utrecht. Thanks to the group of students with whom I got the luck of sharing this year. I appreciate how we manage to go beyond the academical and got such great fun! Not only to the students, but I would also like to thank the whole FCC group for the great year. Dank u!

I would like to thank Rocío Costo-Cámara. We got in touch far before I came to the Nederlands, and yet we did not share as much time as expected, she always supported me. Muchas gracias Rocío, te deseo lo mejor.

Thanks also to my supervisor, prof. Dr. Albert Philipse for bringing me in touch with the granular state of matter via the random packing structure. Thanks as well to prof. Dr. Willem Kegel for the reading of the present document and the supervision in the literature study (which brought me to the statistics beyond stem cell differentiation).

Last, but not least. Thanks to my daily supervisor, Roel Baars. For the patience, the discussions, the critics, the fun, and an endless list of more things. I feel my skills have improved a lot thanks to you. And I make you responsible for the increase in my self-confidence as a scientist during the last year. Actually, this is for me the best result of this research project. I wish you the best with all your projects.